Multifunction Phased Arrays: In-Band Full-Duplex Antennas, Front-Ends and Systems

by

Kenneth E. Kolodziej

B.E., Stevens Institute of Technology, 2007

M.E., Stevens Institute of Technology, 2007

A thesis submitted to the

Faculty of the Graduate School of the

University of Colorado in partial fulfillment

of the requirements for the degree of

Doctor of Philosophy

Department of Electrical, Computer & Energy Engineering

2026

Committee Members:

Prof. Zoya Popović, Chair

Prof. Dejan Filipovic

Prof. Laila Marzall

Dr. Jeffrey Herd

Dr. Patrick Bell

Prof. Jonathan Chisum

Kolodziej, Kenneth E. (Ph.D., Electrical Engineering)

Multifunction Phased Arrays: In-Band Full-Duplex Antennas, Front-Ends and Systems

Thesis directed by Prof. Zoya Popović

Multifunction operation is becoming the standard for wireless systems, including phased arrays that provide electronically-steerable directionality. The general concept refers to systems utilizing the same hardware and frequency spectrum to simultaneously perform multiple different applications, such as radar, communications, jamming, and/or sensing. The optimal combination of these functions is enabled by incorporating in-band full-duplex (IBFD) technology, allowing a system to transmit and receive within the same frequency band at the same time after the resulting self-interference is suppressed. This thesis presents research on the IBFD antennas, front-ends and systems that enable the simultaneous-multifunction operation of phased arrays. Different architectural options are analyzed, with a focus on aperture- and element-level approaches, where the former divides the aperture into transmit and receive subarrays and the latter empowers each element to simultaneously transmit and receive. The mechanisms that influence the mutual coupling between elements within these antenna arrays are studied to create a scalable reduced-coupling array design that is used to determine the system-level requirements, allowing for the mitigation of distinct self-interference components. The unique architecture of two active circulator front-ends with integrated tunable cancellers for on-chip self-interference suppression is demonstrated for devices fabricated as gallium nitride (GaN) monolithic microwave integrated circuits (MMICs). Finally, the measured array and front-end results are integrated into both aperture- and element-level systems, which are excited with realistic radar and communications signals to demonstrate the desired multifunction capability.

Dedication

To my wife, Maria-Christina: I am beyond grateful for your endless support and encouragement for all my adventures − none of them would be possible without you.

To my daughter, Briana: I will never forget doing homework together and answering your amazing questions during my defense − and despite this accomplishment, I'm still *most* proud to be your dad.

Vi amo tantissimo!

Acknowledgements

I would like to start by thanking my advisor, Prof. Zoya Popović, for convincing me to come back to school and working with me throughout the semesters to make the process both fun and productive. I learned more from this experience than I could ever have imagined, and I will be forever grateful!

Many thanks to Prof. Dejan Filipovic for being the second reader of my thesis, and not only providing great feedback, but also teaching me about antennas and mutual coupling over the years. I am also grateful to Prof. Laila Marzall for all of her collaborative discussions throughout this process, as well as her help with the Cadence AWR software used to simulate and tape out the multiple MMIC designs. I would like to express my appreciation to my other committee members, Dr. Jeffrey Herd, Dr. Patrick Bell and Prof. Jonathan Chisum: your insightful comments helped me consider different aspects of the research and improved the final product tremendously.

A final sincere thanks goes to Dr. Christopher Galbraith, Dr. Jonathan Doane and Dr. Songyi Yen for multiple technical discussions; Dr. Seth Johannes for help with the MMIC layout images and general guidance; Michael D'Anna for help with the Ansys HFSS simulator; Will Vu for help with Altium Designer and multiple PCB reviews; the MIT Lincoln Laboratory packaging team for bonding the chips; the LLCAD team for supporting the simulation tools; and MIT Lincoln Laboratory for its funding support.

Contents

Chapter

1 Introduction **1**

1.1 Background and Motivation 1

1.2 In-Band Full-Duplex Overview 3

1.2.1 IBFD Transceiver Diagram 4

1.2.2 Self-Interference Cancellation Techniques 7

1.3 Multifunction Phased Arrays 8

1.3.1 Wireless Functions 9

1.3.2 Array Architecture Overview 11

1.3.3 Critical Technologies 12

1.4 Thesis Outline 12

2 In-Band Full-Duplex Antenna Arrays **14**

2.1 Introduction 14

2.2 IBFD Array Types 16

2.3 Aperture-Level IBFD Arrays 19

2.3.1 Array Architecture 19

2.3.2 Digitally-enabled SIC Processes 21

2.4 Element-Level IBFD Arrays 24

2.4.1 Array Architectures 24

2.5 IBFD Array Prototypes . . . 26
2.5.1 Measurement Survey . . . 26
2.5.2 Results and Challenges . . . 29
2.6 Chapter Conclusion . . . 32

3 Mutual Coupling and System Requirements 34
3.1 Introduction . . . 34
3.2 Mutual Coupling Overview . . . 36
3.3 Coupling-Reduction Techniques . . . 39
3.4 Reduced-Coupling Array . . . 42
3.4.1 Baseline Design . . . 44
3.4.2 Reduced-Coupling Design . . . 46
3.5 System Analysis . . . 48
3.5.1 Aperture-Level IBFD Array Requirements . . . 50
3.5.2 Element-Level IBFD Array Requirements . . . 53
3.6 Chapter Conclusion . . . 56

4 IBFD Front-End One-Tap Active Circulator 57
4.1 Introduction . . . 57
4.2 Architecture Overview . . . 61
4.3 Active Circulator Design . . . 63
4.3.1 Amplifier Design . . . 64
4.3.2 Phase Shifter Design . . . 66
4.4 Measured Results . . . 68
4.5 Chapter Conclusion . . . 72

5 IBFD Front-End Two-Tap Active Circulator 73
5.1 Introduction . . . 73

5.2 Active Circulator Improvements . . . 73
5.2.1 Power Divider Design . . . 73
5.2.2 Amplifier Design . . . 74
5.2.3 Phase Shifter Design . . . 75
5.3 Measured Results . . . 78
5.3.1 S-Parameters . . . 79
5.3.2 PA and LNA Performance . . . 80
5.3.3 Modulated-Signal Characterization . . . 82
5.4 Chapter Conclusion . . . 84

6 System-Level Array Integration **87**
6.1 Introduction . . . 87
6.2 Aperture-Level IBFD Array . . . 89
6.2.1 Antenna Array . . . 89
6.2.2 Front-End . . . 92
6.2.3 Signal Processing . . . 94
6.2.4 System Evaluation . . . 98
6.3 Element-Level IBFD Array . . . 102
6.3.1 Antenna Array . . . 104
6.3.2 Front-End . . . 107
6.3.3 Signal Processing . . . 108
6.3.4 System Evaluation . . . 109
6.4 Chapter Conclusion . . . 112

7 Conclusion **114**
7.1 Thesis Summary . . . 114
7.2 Future Work . . . 116
7.2.1 Antennas . . . 116

7.2.2 Front-Ends 118

7.2.3 Systems 119

7.3 Summary of Contributions 121

Bibliography **122**

Appendix

A Appendix **135**

A.1 Introduction 135

A.2 Coupling-Reduction Techniques Results 135

A.3 Reduced-Coupling Array Design Results 141

Tables

Table

1.1 Summary of Wireless Function Characteristics 11

2.1 Summary of Measured IBFD Phased Array Systems 26

2.2 Summary of Simulated IBFD Phased Array Systems 28

3.1 Summary of Simulated Coupling-Reduction Techniques 43

3.2 Summary of Simulated Reduced-Coupling Array Design 48

5.1 Summary of Measured Active Circulators using III-V Compound Semiconductors . . 85

6.1 Summary of System-Level Array Losses 112

Figures

Figure

1.1 Multifunction Phased Array Scenarios 2

1.2 IBFD Transceiver Diagram 5

1.3 Self-Interference Cancellation Techniques 7

1.4 Graphical Thesis Summary 8

2.1 Example Array Comparisons 15

2.2 IBFD Phased Array Architectures 17

2.3 Aperture-Level IBFD Subarray Losses 18

2.4 Aperture-Level IBFD Array Architecture 20

2.5 Aperture-Level IBFD Array Signal Progression 21

2.6 Element-Level IBFD Array Architectures 25

2.7 Measured IBFD Array Systems Performance 27

2.8 Aperture-level IBFD Array Performance 29

2.9 Element-level IBFD Array Performance 31

3.1 Array System Diagram and Interference Components 35

3.2 Designators for a 25-Element Array 37

3.3 Aperture-Level IBFD Array Coupling 38

3.4 Element-Level IBFD Array Coupling 39

3.5 Unit Cell for Coupling-Reduction Techniques 40

3.6 Baseline E- and H-Plane Array Models 41
3.7 Baseline E- and H-Plane Array Fields 42
3.8 Simulated Mutual Coupling for E- and H-Planes 42
3.9 Coupling-Reduction Techniques 43
3.10 Baseline 25-Element Array 44
3.11 Reduced-Coupling 25-Element Array 46
3.12 Receiver Cascade Analysis 49
3.13 Aperture-Level Array Cancellation Requirements 52
3.14 Element-Level Array Cancellation Requirements for Low-Gain Front-Ends 54
3.15 Element-Level Array Cancellation Requirements for High-Gain Front-Ends 55

4.1 Multifunction Phased Array Radar Scenario 58
4.2 Active Circulator Front-End MMICs 60
4.3 Front-End Active Circulator Diagram 62
4.4 Active Circulator with One-Tap Canceller Layout 64
4.5 Amplifier Circuit Schematic, Layout and Photo 65
4.6 Amplifier Circuit Characterization 66
4.7 Phase Shifter Circuit Schematic, Layout and Photo 67
4.8 Phase Shifter Circuit Characterization 68
4.9 Measurement Setup Photo 69
4.10 One-Tap Active Circulator PCB 69
4.11 One-Tap Active Circulator S-Parameter Measurements 70
4.12 One-Tap Active Circulator Coupling Measurement 71

5.1 Active Circulator with Two-Tap Canceller Layout 74
5.2 Power Divider Comparison 75
5.3 Two-Tap Canceller Circuit Schematic, Layout and Photo 76
5.4 Two-Tap Canceller Circuit Characterization 77

5.5 Two-Tap Active Circulator PCB 78
5.6 Two-Tap Active Circulator S-Parameter Measurements 79
5.7 Two-Tap Active Circulator Coupling Measurement 80
5.8 Two-Tap Active Circulator PA and LNA Measurement 81
5.9 Two-Tap Active Circulator Modulated-Signal Measurement 82

6.1 Aperture-Level IBFD Array Signal Model 88
6.2 10-Element Antipodal Vivaldi Array 90
6.3 Antipodal Vivaldi Array |S11| Measurement 90
6.4 Antipodal Vivaldi Array Coupling 91
6.5 Aperture-Level IBFD Array Front-End 92
6.6 Integrated Front-End S-Parameter Measurements 94
6.7 Simulated Aperture-Level IBFD Array Power Levels 96
6.8 Simulated Coupled Power and Array Gain 97
6.9 Aperture-Level IBFD Array Evaluation with Two-Tone Signal 99
6.10 Aperture-Level IBFD Array Evaluation with LFM Signal 101
6.11 Element-Level IBFD Array Signal Model 102
6.12 Reduced-Coupling 25-Element Patch Array 104
6.13 Reduced-Coupling Array Measurement Setup 104
6.14 Reduced-Coupling Array |S11| Measurement 105
6.15 Reduced-Coupling Array Mutual Coupling Measurement 106
6.16 Discrete Canceller Diagram 107
6.17 Element-Level IBFD Array Evaluation with Two-Tone Signal 110
6.18 Element-Level IBFD Array Evaluation with LFM Signal 111

7.1 Unit Cells for Wideband Arrays 117
7.2 Active Circulator with Wilkinson Layout 118
7.3 Simulated Resistive/Wilkinson Divider Comparison 119

7.4 Neural Network Diagram 120

A.1 Mutual Coupling Reduction – Metallic Posts 137

A.2 Mutual Coupling Reduction – Metallic Walls 138

A.3 Mutual Coupling Reduction – EBG 139

A.4 Mutual Coupling Reduction – DGS 140

A.5 Reduced-Coupling 25-Element Array – Configuration 1 142

A.6 Reduced-Coupling 25-Element Array – Configuration 2 143

A.7 Reduced-Coupling 25-Element Array – Configuration 3 144

A.8 Reduced-Coupling 25-Element Array – Configuration 4 145

A.9 Reduced-Coupling 25-Element Array – Configuration 5 146

Chapter 1

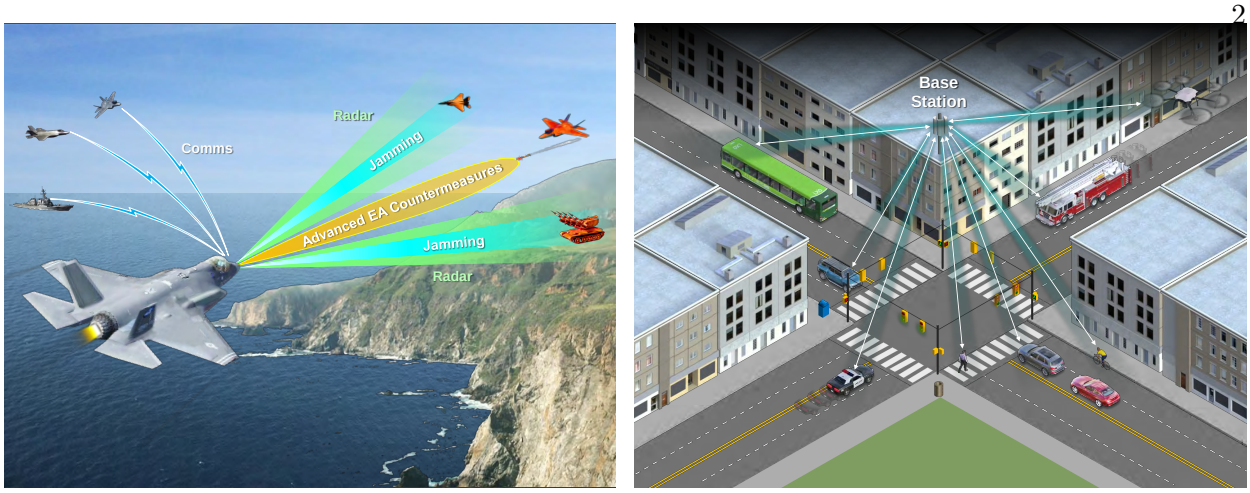
Introduction

1.1 Background and Motivation

Active phased array systems are gaining popularity in many wireless applications due to their ability to electronically create, steer and change multiple beams with high directivity as well as adaptively reduce external interference [50]. Fifth- and next-generation (5G and NextG) wireless communications are leveraging phased arrays to create smart base stations in sub-6 GHz Frequency Range 1 (FR1) [132] as well as overcoming the propagation losses in the FR2 millimeter-wave spectrum [93]. For space-based constellations like Starlink and Kuiper, ground stations utilize phased arrays to simultaneously track multiple satellites using different beams without any mechanical movement [46]. The stringent link budgets of radar applications have also benefited from the high directivity of phased arrays as well as their angle-of-arrival estimation accuracy without cumbersome and costly servo motors for object detection [142]. Finally, electronic warfare (EW) systems are beginning to leverage phased arrays to more accurately locate hostile signals in noisy environments and precisely direct their jamming attacks [61].

In addition to creating traditional "stove-piped" solutions for these applications, the flexibility of phase array systems makes them an attractive option to simultaneously support multiple functions. In this context, multifunctionality refers to the concept of common hardware (a phased array, in our case) being able to host more than one modality, which can include radar, communications, jamming, sensing, and/or other applications.

The investigation into these multifunction RF systems began as the number of antennas



(a) (b)

Figure 1.1: Multifunction phased array scenarios, highlighting (a) a defense application where a fighter aircraft can simultaneously communicate, employ radar and engage jamming, or advanced electronic attack (EA) countermeasures, and (b) a commercial application with a smart base station providing communications enhanced by object tracking. Reprinted from [78].

on navy ships exploded between the 1980s and 1990s [144]. In hopes of combating this trend, researchers focused on creating wideband phased arrays that allowed multiple functions to share common hardware with frequency- and/or time-division duplexing schemes [48,112,128]. Following those efforts, a summary of the key requirements and design tradeoffs for various defense-focused radar, EW and communications modes was presented in [102]. In order to help visualize this concept, Fig. 1.1a illustrates a defense scenario where a multifunction system enables a fighter aircraft to communicate with friendly aircraft and ships while simultaneously employing radar and jamming functions on enemy targets.

Applications that employ radio-based sensing have exploded in not only the traditional defense space but also the civilian/commercial sector. As a result, researchers have recently started investigating ways to integrate sensing into existing communications systems that contend for the same spectral resources. This concept is referred to as integrated sensing and communication (ISAC), and represents the simultaneous hosting of both radar and wireless communications applications within the same device [88]. This is shown in Fig. 1.1b for a smart base station that can

communicate with users as well as sense their locations to improve their links. Cognitive radios also benefit from hosting multiple functions, namely communications and spectrum sensing, to accomplish the goals of creating highly-reliable communications and efficiently utilizing the radio spectrum [45, 127], often employing wideband receiver architectures for the sensing [60, 101].

All these multifunction examples represent a new paradigm that embraces the convergence of different applications, which is in contrast to their historical coexistence, where systems would treat each other as interference sources and designers worked to improve the tolerance to the others. A significant restriction of the aforementioned research is that these multifunction systems were forced to share their common hardware in a frequency- and/or time-duplexed manner, meaning that two functions could not access the same frequency band at the same time. This limitation forces users to prioritize one application over another, which could drastically impact the performance of combing several functions as compared to their individual metrics, and generates questions surrounding the usefulness of combining the functions in the first place.

1.2 In-Band Full-Duplex Overview

This is where in-band full-duplex (IBFD) technology enters the picture: allowing systems to simultaneous transmit and receive on the same frequency as well as adjacent channels without the need for guard bands or times [20, 124]. IBFD helps overcome the obstacles that result from multiple functions attempting to access the same spectral and hardware resources by allowing for the reception of signals (i.e., radar returns) while simultaneously transmitting (e.g., for communications). This technology, however, introduces its own challenges, namely figuring out how to suppress the self-interference (SI) that results from transmitting and receiving within the same frequency band at the same time [75]. Unfortunately, there is not a universal solution to overcome the SI in IBFD systems, and instead requires a combination of cancellation techniques that depend on the specific application and environment [63].

Despite this hurdle, IBFD has been shown to enhance the multifunction capabilities for each of the previously mentioned use-cases. For defense applications, IBFD radios have combined tac-

tical communications with different same-frequency EW scenarios [118], and a counter improvised explosive device (IED) system with IBFD benefited from the ability to simultaneously detect and jam trigger signals [119]. IBFD operation has been shown to increase the throughput and reduce collisions in cognitive radio networks by providing a continual sensing ability [3], and has been demonstrated to be a key enabler to decoupling the timing requirements for ISAC systems at 2.4 and 28 GHz frequencies [9]. Building on these successes, IBFD phased arrays are now beginning to be investigated to enhance the flexibility of simultaneous multifunction systems for the applications previously discussed [65].

It should be noted that the term IBFD grew out of the communications community, and that there are other names applied to the same concept. The analogous term – simultaneous transmit and receive (STAR) – seems to have been adopted by defense organizations, possibly to encompass the asymmetric data traffic of military systems that support applications other than communications. Additionally, while same-frequency full-duplex (SFFD) can also be used to describe the technology, many publications simply refer to it as full-duplex (FD). Similar to STAR, the FD term traditionally includes systems that transmit and receive at the same time on different frequencies, known as frequency-division duplex (FDD) or out-of-band full-duplex, and should thus be avoided when specifically discussing IBFD systems. With that said, these terms will be used interchangeably throughout the thesis to all refer to the concept of concurrent transmission and reception within the same frequency band.

1.2.1 IBFD Transceiver Diagram

Many wireless systems concern themselves with interference suppression and protection against external signals to ensure desired operation. IBFD systems, however, have the additional challenge of mitigating strong interference signals generated within the node/device itself. While this difference means that many possible coupling paths exist, it also offers designers the benefit of being able to influence the coupling mechanisms and sometimes even the SI signal itself. IBFD technology only becomes viable when these benefits are exploited to provide SI cancellation (SIC) that results

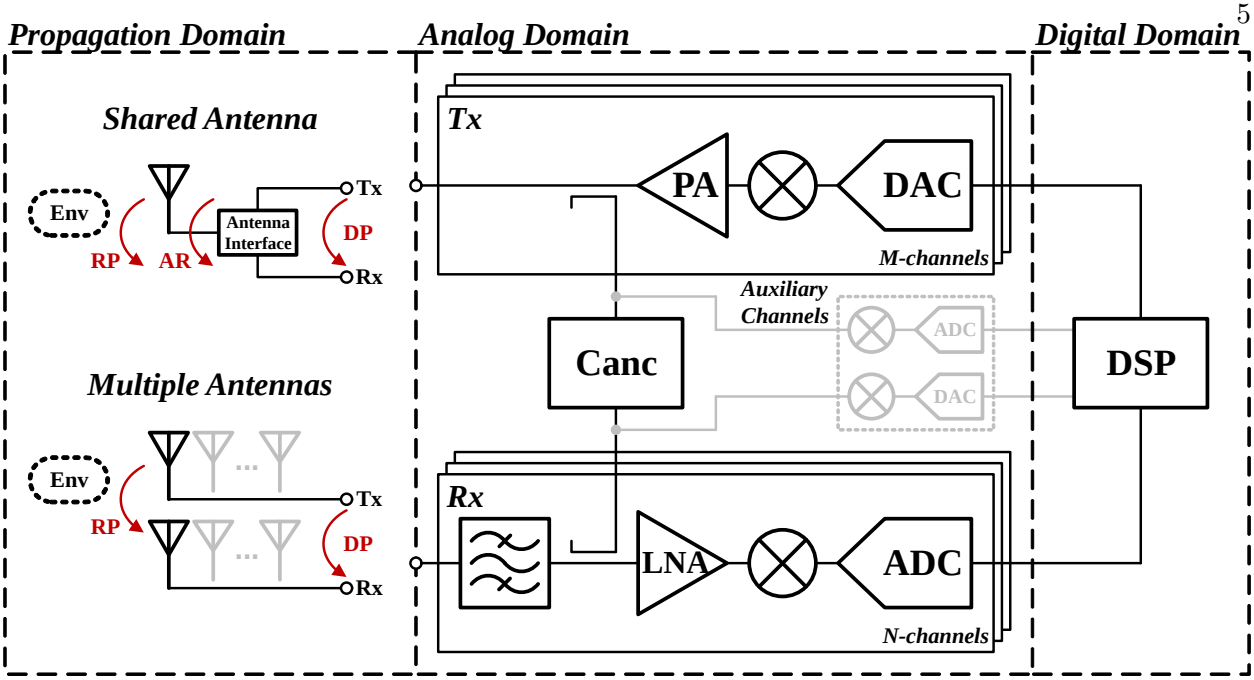


Figure 1.2: Block diagram of a typical IBFD transceiver, highlighting the propagation, analog and digital domains where self-interference cancellation techniques can be applied. Reprinted from [63].

in effectively isolating the receiver from the transmitter.

Potential locations for SIC can be considered by studying the generic IBFD transceiver diagram of Fig. 1.2. This diagram illustrates a transceiver broken down into three different domains: propagation, analog and digital [75]. The propagation domain applies to systems that share a single antenna through the use of an antenna interface device as well as designs that utilize multiple antennas for transmit and receive capabilities. Additionally, multiples of either antenna approach can be used to create arrays that introduce other SIC options. Both configurations include direct path (DP) coupling between the transmitter and receiver, which often represents the first SI component to arrive at the receiver. For multiple antennas, this is typically the line-of-sight path, and for the shared case, the DP captures the finite amount of leakage provided by the antenna interface. While these DPs are fairly static, IBFD systems must also contend with dynamic SI reflection paths (RPs) that are influenced by the environment surrounding the node. Local multipath scattering can reflect the transmit signal back towards the receiving antenna and effectively produce delayed echoes of the SI signal that become increasingly problematic as the transmit power increases. Finally, for

the shared antenna setup, an antenna reflection (AR) is created since the antenna impedance is not perfectly matched to that of the connected antenna interface. Similar to the RPs, this AR is also influenced by the immediate surroundings that can alter the perceived impedance of the antenna and effectively change the reflection signal. Due to this AR, and the tightly coupled relationship of the antenna and its interfacing device, SIC techniques related to the antenna interface are included in the propagation domain instead of the analog domain discussed next.

Within the analog domain of the transceiver resides the radio hardware responsible for conditioning and converting the propagation, or radio frequency (RF), signal to and from the digital domain. The diagram depicts M transmit (Tx) channels, each with a digital-to-analog converter (DAC) and power amplifier (PA). Additionally, a single frequency conversion mixer is also represented, but only depicts a common configuration. Realistic designs may contain more or less frequency conversion stages as well as associated out-of-band filtering and additional gain to appropriately adjust the signal before transmission. Similarly, N receive (Rx) channels are illustrated with a unique same-frequency in-band filter at the input to provide SIC that discriminates the SI by a signal parameter other than frequency. This filter is followed by a low-noise amplifier (LNA), a single frequency conversion mixer and an analog-to-digital converter (ADC). Both the linearity and saturation level of these active receiver components must be carefully considered to determine how much propagation and analog domain suppression is required before the digital domain. Analogous to the transmit side, realistic receivers will include different amounts of gain and frequency conversion as well as out-of-band filtering to suppress the external interference encountered by traditional wireless systems.

The figure also illustrates a cancellation (Canc) element between the transmit and receive channels. This specific depiction shows the canceller operating at RF (the propagation frequency), and coupling off the transmit signal path after the PA. While this represents a common configuration, both the operating frequency and location within the transceiver can vary, along with the canceller feeding mechanism. Alternative designs employ auxiliary channels to aid in SIC in either the analog and/or digital domains. A representative subset of the required components in these

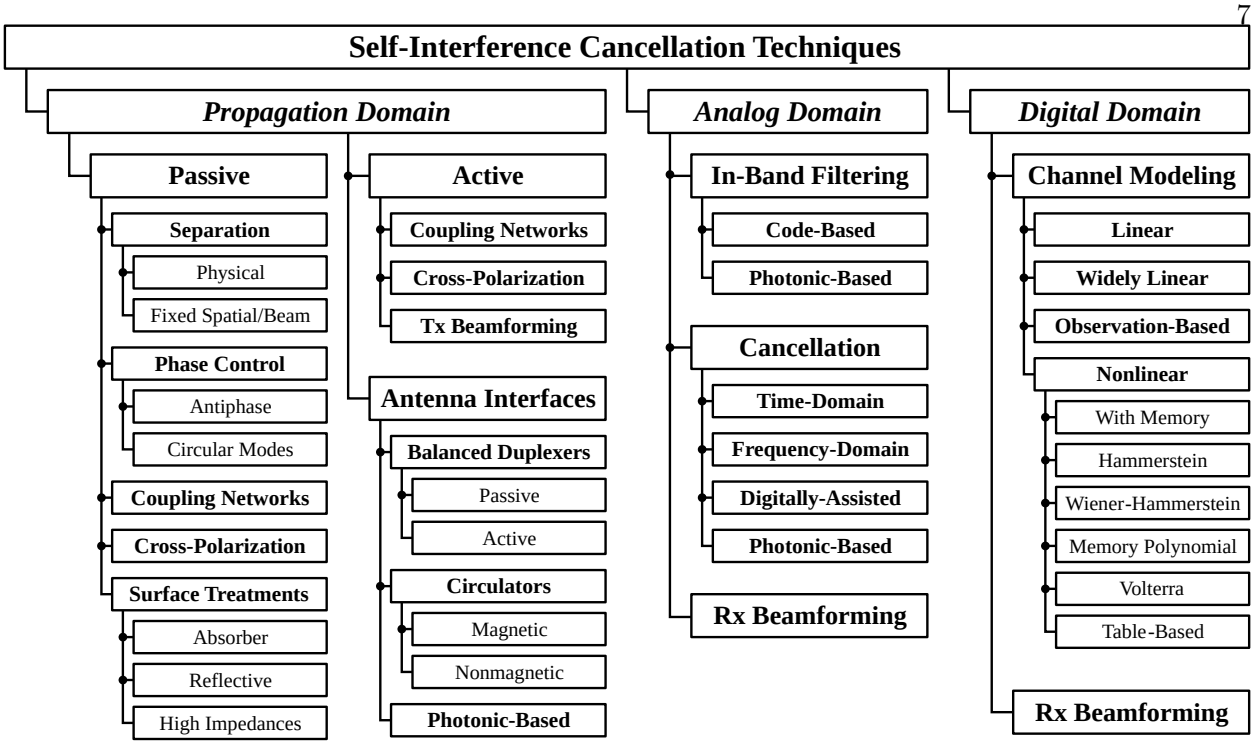


Figure 1.3: Self-interference techniques tree, highlighting a collection of options that have been demonstrated in the propagation, analog and digital domains. Reprinted from [63].

auxiliary channels and their connection paths are also captured within this generic transceiver.

Finally, the digital domain contains all SIC techniques that are controlled through digital signal processing (DSP). The diagram intentionally maintains an abstract representation of these capabilities since they are numerous and ever-growing. This generic transceiver diagram can be referenced throughout the thesis to help orient the reader to which part of the transceiver and associated SIC domain is being highlighted within each individual chapter.

1.2.2 Self-Interference Cancellation Techniques

The remaining chapters in this thesis leverage SIC techniques and their application within different locations of the generic transceiver shown in Fig. 1.2. The previously discussed breakdown among the propagation, analog and digital domains can be utilized to group these methods as depicted in Fig. 1.3. This tree diagram is organized based on the location where cancellation occurs, and provides a convenient list of SIC techniques that have previously been published and

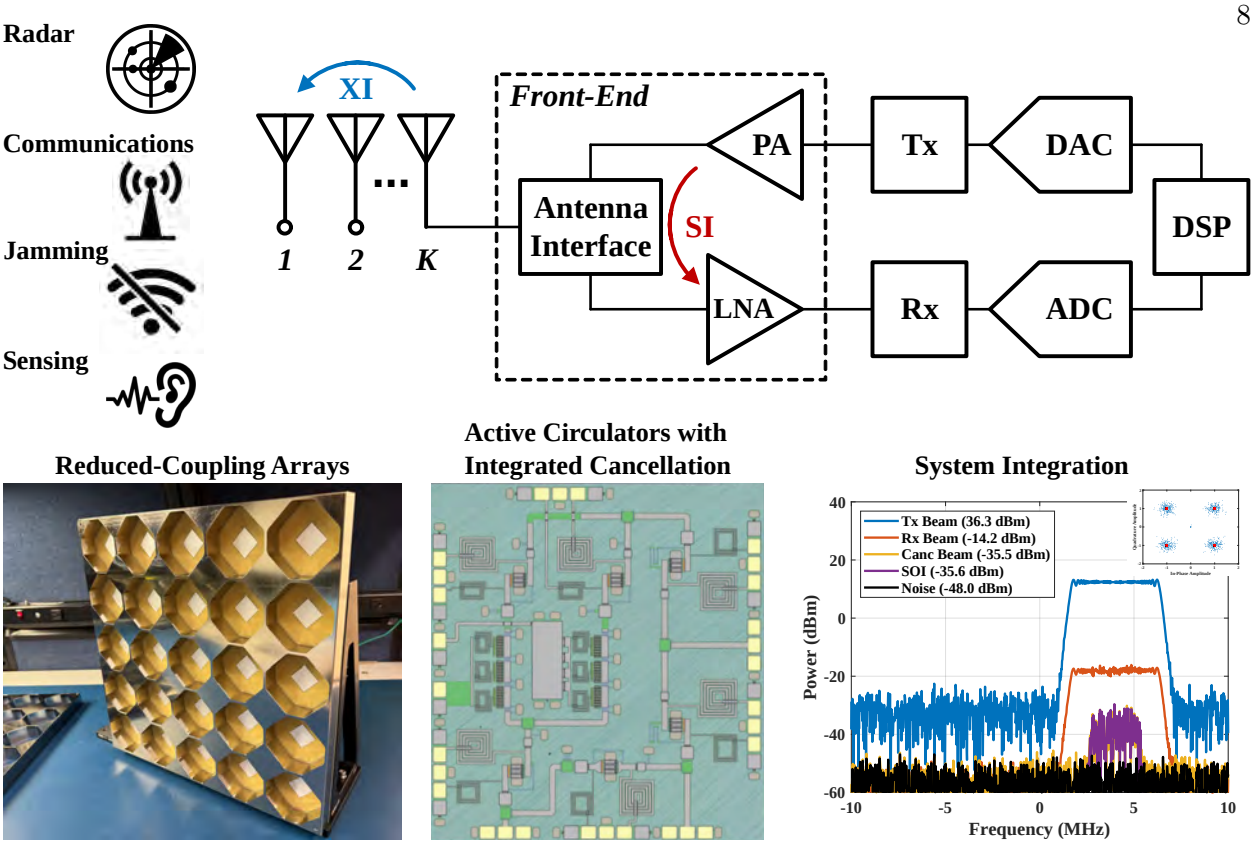


Figure 1.4: Graphical thesis summary, highlighting the multiple wireless functions, high-level array architecture with self-interference (SI) and crosstalk interference (XI), and the critical technologies that enable multifunction arrays.

initially summarized in [75]. The propagation domain includes various passive and active antenna techniques as well as the several different antenna interfaces. The analog domain contains in-band filtering, assorted cancellation methods and analog receive beamforming, while the digital domain encompasses numerous channel-modeling and digital receive beamforming approaches.

1.3 Multifunction Phased Arrays

The previous sections provided an overview of IBFD technology and highlighted the need for it within multifunction systems. The unique aspects of the different wireless functions and the key components that enable their combination within phased arrays, however, have yet to be discussed. Fig. 1.4 illustrates a graphical summary of three key topics that will be presented throughout this thesis: 1. the wireless modalities supported, 2. the array system architecture, and 3. the underlying

technologies that enable the array, all of which are summarized in the following subsections.

1.3.1 Wireless Functions

The top left of Fig. 1.4 lists the four different wireless functions capable of being supported by the multifunction phased arrays discussed throughout this thesis. As previously mentioned, these consist of radar, communications, jamming, and sensing, where these four modalities were selected based on their unique characteristics.

Radar systems are focused on detecting the presence and location of surrounding objects. They often utilize transmit pulses consisting of linear-frequency modulated (LFM) signals, and typically have duty cycles around 10% (i.e., transmit for 10% and receive for 90% of the time), but could extend up to 100% for both transmission and reception in some architectures. These waveforms are instantaneously narrowband and consist of swept continuous wave (CW) signals, which do not introduce intermodulation distortion and allows the PA to operate with enhanced efficiency in saturation. Signals-of-interest (SOIs) for this application are radar returns, or echoes, which are inherently at the same frequency but delayed in time from the transmit signal reflecting off objects in the environment.

Communications systems, on the other hand, are interested in exchanging information between two or mode nodes within a network. These signals employ different modulation schemes to encode information in the form of data packets onto a carrier signal. The modulation originated with analog methods − analog modulation (AM), frequency modulation (FM) and phase modulation (PM) − and has since incorporated digital versions, including phase shift keying (PSK), frequency shift keying (FSK), and quadrature amplitude modulation (QAM). Well-known communications systems, such as Wi-Fi, fourth generation Long-Term Evolution (4G LTE) and 5G new radio (NR), utilize variants of QAM, which allow more data to be transmitted in a single packet by modulating both the amplitude and phase of the signal. These amplitude modulations at multiple frequencies, however, can generate intermodulation distortion, which needs to be considered when selecting the PA operating point. SOIs for communications systems are often similar signals that originate from

other users/devices within the network, and are uncorrelated with the node transmissions. Data traffic for communications systems can vary for each specific application, and as referenced to the user equipment (UE), include symmetric (50% transmit, 50% receive), downlink-focused (near 0% transmit, near 100% receive), and uplink-focused (near 100% transmit, near 0% receive).

Jamming systems attempt to deliberately disrupt the operation of other wireless systems by introducing strong interfering signals within the same frequency band. These can target both radar and communications devices, and often leverage wideband waveforms, such as barrage noise. While these signals can simultaneously block multiple frequencies, which is especially useful when the operating band of the victim is not known or is changing with time, the output power is limited by the PA and a power-bandwidth tradeoff must be considered. With that in mind, these systems typically operate with nearly 100% transmit duty cycles, and can generate intermodulation distortion, but often are not concerned with limiting their spurious signal transmissions. Depending on the target and assuming there is some receive time allocated, SOIs can include radar, communications and other signals that can be used to enhance the effectiveness of the jammer.

Finally, sensing systems refer to passive receive-only operation that allows for the detection of wireless signals in the environment. These can include radar, communications, jamming, and other signals, which can be utilized to improve the performance and/or intelligence of the aforementioned modalities, or simply survey the electromagnetic spectrum. Without transmitting, there are no intermodulation signals to be concerned with. While fully-passive sensing is advantageous in certain circumstances, this function is often combined with one of the transmitting applications and is intrinsically provided by IBFD operation.

The various aspects of these different functions are summarized in Table 1.1, where varying transmit and receive duty cycle allocations are seen to be a significant differentiator between them. Additionally, the presence of transmit intermodulation distortion as well as the SOI types and related transmit signal correlation are captured. Based on this summary, it is evident that there are some inherent opportunities to integrate these functions by utilizing different array resources, including time, frequency, beam space, and power-aperture utilization. Simultaneous-multifunction

Table 1.1: Summary of Wireless Function Characteristics

Function	**Duty Cycle (%)**		**Tx Intermod-ulation**	**SOI**	
	Tx	**Rx**		**Type**	**Tx Corre-laton**
Radar	10	90	No	Radar	Yes
Communications	50	50	Yes	Communications	No
Jamming	100	0	Yes	All	Yes
Sensing	0	100	No	All	No

operation, however, can only be enabled by studying the underlying array architecture and devising an appropriate SI mitigation strategy.

1.3.2 Array Architecture Overview

Building upon aspects of the transceiver discussed in Fig. 1.2, a high-level architecture of an array that can enable multifunction IBFD operation is depicted in the top right of Fig. 1.4. This diagram illustrates K antenna elements, each connected to individual front-ends that are comprised of an antenna interface, PA and LNA. Following the front-end are transmit and receive components that connect to data converters and subsequent DSP. As will be discussed in detail in the following chapters, there are two main sources of interference in IBFD arrays: self-interference (SI) within each element and crosstalk interference (XI) that arises between the elements, as indicated in the figure. The former is highly dependent on the design of the antenna interface, for which several options exist according to Fig. 1.3, namely balanced duplexers, circulators and photonic-based approaches. The latter is governed by the mutual coupling between the elements of the array, and can be influenced by incorporating different passive and/or active techniques listed under the propagation-domain section of Fig. 1.3. These areas represent two of the key aspects that enable multifunction IBFD arrays, as discussed next.

1.3.3 Critical Technologies

The lower half of Fig. 1.4 represents the three critical IBFD array technologies that are explored within this thesis to mitigate both SI and XI as well as enable the desired multifunction capability. Reduced-coupling arrays decrease the amount of transmit signal leaking into the neighboring elements that are simultaneously receiving. In order to understand the system-level ramifications of this coupling, Chapter 2 provides a background on IBFD arrays, while Chapter 3 dives into a reduced-coupling array design. Ideally, a front-end should be selected so that it not only sufficiently suppresses the SI, but also allows the array size to be scaled in two dimensions, which implies that it is compact enough to fit within the array lattice spacing defined by the operational wavelength. For this purpose, nonmagnetic active circulators can be utilized, where two different monolithic microwave integrated circuits (MMICs) with different cancellers are discussed in Chapters 4 and 5. Finally, it is the combination of antenna arrays with front-end circuits behind each element that creates the complete phased array. This system integration relies on SIC techniques listed under the digital-domain section of Fig. 1.3, and are necessary in order to fully remove the SI and XI signals and extract the desired information from the SOIs for the different functions, as discussed in Chapter 6.

1.4 Thesis Outline

This thesis presents work towards creating state-of-the-art IBFD phased arrays that can enable simultaneous-multifunction operation. The various aspects highlighted in Fig. 1.4 will be expanded upon with additional background information, experimental prototype results and detailed simulations of integrated multifunction arrays.

Chapter 2 overviews array fundamentals and introduces the architectures that enable IBFD at the aperture and element levels as well as summarizes the current research in the field, highlighting both state-of-the-art prototype results and simulation efforts. Material for this chapter is based on content reported in [77] and [78].

Chapter 3 discusses mutual coupling within arrays and analyzes different approaches to reduce the element-to-element leakage, which is expanded from work previously published in [68]. The design of a reduced-coupling array is also presented and utilized to derive the system-level cancellation requirements for aperture- and element-level IBFD arrays.

Chapter 4 highlights a multifunction radar application that can benefit from IBFD arrays and presents the design of an active circulator front-end MMIC with a one-tap integrated canceller, including subcircuit performance and full-chip measurement results.

Chapter 5 expands upon this front-end architecture and describes an advanced design that incorporates a two-tap integrated canceller as well as additional subcircuit improvements. The MMIC is characterized with small-, large- and modulated-signal inputs, where both this and the previous chapter are based on the material reported in [71] and [72].

Chapter 6 presents the array-level system integration that leverages the measured results of antenna prototypes and front-end MMICs for both aperture- and element-level IBFD arrays. This chapter illustrates the capability of digital-domain techniques to remove the residual SI and XI to enable multifunction operation. The aperture-level IBFD part of this chapter is based on work reported in [58] and currently in publication review in [70].

Chapter 7 draws conclusions from the totality of the work presented in this thesis and discusses plans for future research that would further the maturity of advanced multifunction phased arrays with IBFD technology.

Appendix A contains the model details and simulated results for the mutual coupling reduction techniques considered as well as the design evolution of the reduced-coupling array presented in Chapter 3.

Chapter 2

In-Band Full-Duplex Antenna Arrays

2.1 Introduction

An antenna array is a group of antenna elements that are coherently operated to increase the effective area, and therefore gain, of the antenna. Such arrays usually have identical elements located on a uniform grid, where designers can select an element type with either an omnidirectional or directional pattern as well as the spacing between the elements, both of which influence the overall radiation characteristics. This results from the combination of the element pattern and the array factor, and effectively enhances the directivity of the individual elements regardless of their native directionality. For example, the azimuthal radiation pattern of a four-element dipole array is shown in Fig. 2.1a, and compares different element spacings, d. Starting with the $\lambda/2$ case, the maximum antenna gain can be found at 0-degrees azimuth while sidelobes are seen at ± 45 degrees. One of the effects of starting with an omnidirectional element is visible when we look at ± 180 degrees, where the array directivity level matches that of the main beam at 0 degrees. This "back lobe" is more obvious when the directivity is plotted in polar coordinates, as shown in Fig. 2.1b, where the patterns are clearly symmetrical in the forward (up) and backward (down) directions.

Figs. 2.1a and 2.1b also illustrate the introduction of "grating lobes" at ± 45 and ± 135 degrees when the element spacing is $3\lambda/2$. These undesired lobes are predicted by the pattern multiplication theorem of the array factor, and are related to the element spacing and array scan conditions. While their appearance may be mitigated by nulls in the element pattern, they generally appear when the spacing is greater than $\lambda/2$ and become more noticeable when the array is scanned. The fact

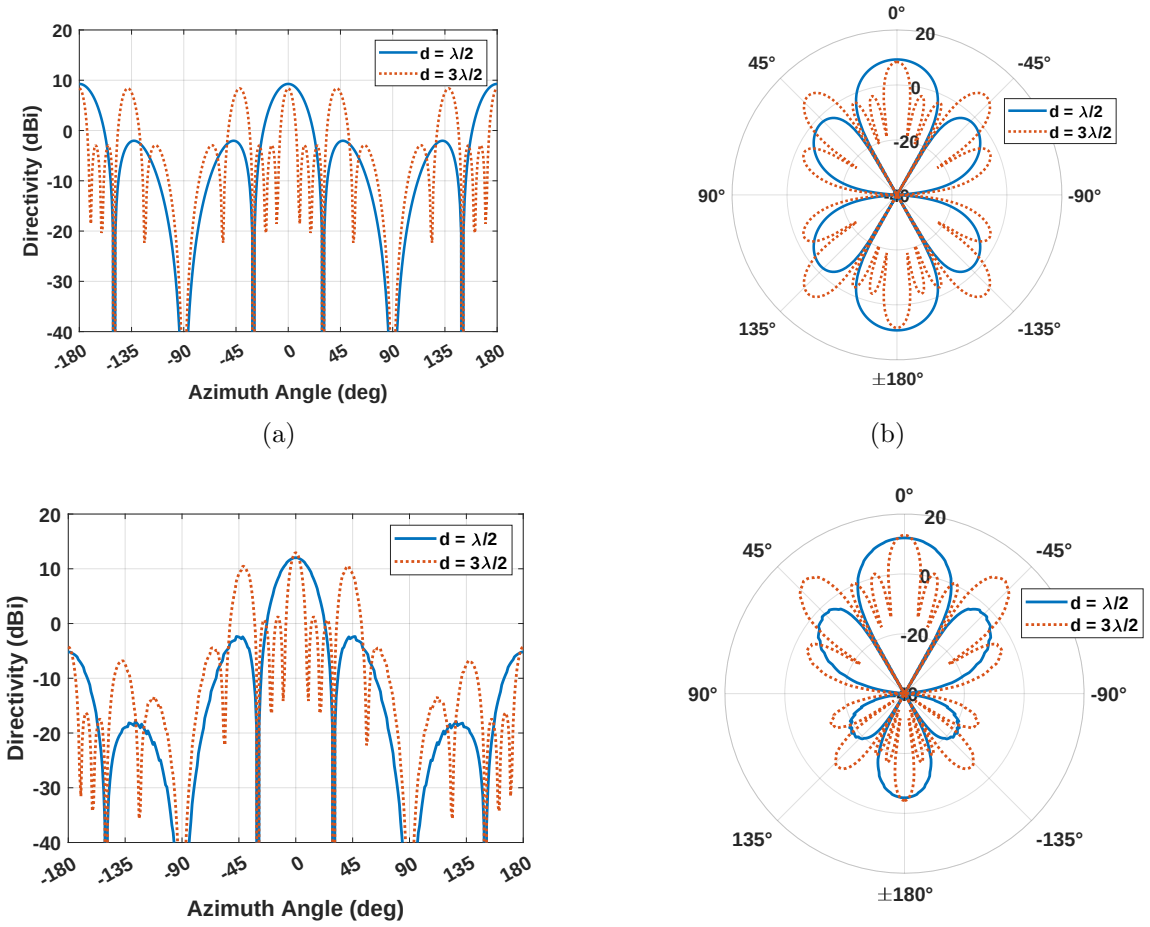


Figure 2.1: Example array comparisons with elements spaced by a distance, d, for a 4-element dipole linear array radiation pattern versus azimuth angle in (a) rectangular and (b) polar coordinates, and a 4-element linear patch array radiation pattern versus azimuth angle in (c) rectangular and (d) polar coordinates. Reprinted from [78].

that multiple azimuth angles exhibit the same directivity (i.e. the main-lobe level is the same as the back lobe and possibly the grating lobes) introduces an angle ambiguity. When receiving, this ambiguity effectively means that the incoming signal's angle-of-arrival can be one of several angles (i.e. angles with the same directivity), which is often not very helpful for many applications and thus leads us to arrays with directional elements.

Similar to the dipole array, Figs. 2.1c and 2.1d plot the directivity of a four-element linear patch array with different element spacings, d. For the $3\lambda/2$ configuration, grating lobes can be

seen near ±45 and ±135 degrees, which are similar to the dipole scenario (it should be noted that the grating lobes around ±135 degrees are suppressed by the native patch pattern as compared to the dipole). Both directivity figures also illustrate a back lobe at ±180 degrees, which results from the imperfect nature of the directive element. The significant difference between these plots and those of the dipole array, however, is the level of the back-lobe radiation. For the patch array, the back lobe is seen to be more than 15 dB lower than the main beam, which allows the array to successfully discern the angle-of-arrival of a received signal and eliminate the angle ambiguity associated with omnidirectional-element arrays. This leaves us with the patch array setup with $\lambda/2$ element spacing that exhibits minimal back lobe and side-lobe levels as well as eliminates the grating lobes, and will be the configuration considered in the remaining sections of this chapter.

2.2 IBFD Array Types

When thinking how to possibly incorporate the ability to simultaneously transmit and receive into a directional array (for multifunction or normal operation), several different options can be considered. The arrays within each architecture are constructed and configured differently, which presents unique challenges and opportunities for self-interference cancellation (SIC). As shown in Fig. 2.2, the options consist of multi-array, aperture-level and element-level designs (where each square represents a directional element, i.e. patch).

Multi-array designs utilize two distinct antenna arrays for transmit and receive, which are physically separated from one another by some distance, as shown in Fig. 2.2a. Similar to non-array systems with separate antennas, this configuration reduces the direct-path (DP) coupling through the physical separation of the arrays, which provides isolation in a very straightforward manner [34]. Unlike non-array systems, however, these arrays offer the added flexibility of incorporating adaptive beamforming with degrees-of-freedom that do not exist in systems with only single-element antennas [40, 120, 129, 130]. Unfortunately, the necessity of two unique arrays that are spatially separated requires a large physical volume to implement. This effectively limits this particular array architecture to larger platforms, and may not be suitable for many space-constrained applications.

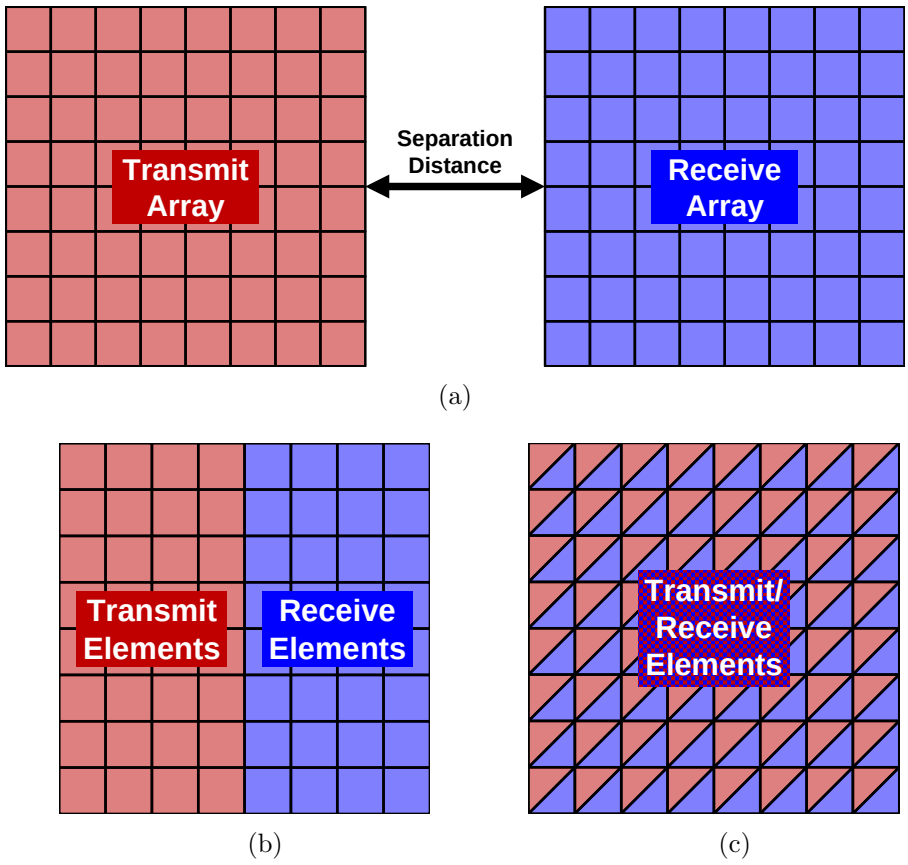


Figure 2.2: IBFD phased array architectures, highlighting the different transmit and receive elements for: (a) multi-aperture, (b) aperture-level and (c) element-level designs. Reprinted from [78].

This size disadvantage is eliminated for both the aperture- and element-level cases that utilize the same array for transmit and receive. Aperture-level arrays operate by electronically dividing the array into distinct zones, or subarrays, where some elements are assigned for transmit and the others for receive. This concept is depicted in Fig. 2.2b for an example 8×8 configuration that nominally splits the array down the middle, forming two 8×4 subarrays. This architecture enables IBFD operation between the subarrays by creating high amounts of SIC using a combination of adaptive digital beamforming and cancellation techniques, as discussed in the next section. The most significant benefit of this approach is that the subarrays can be dynamically reconfigured between transmit and receive based on the data received and/or the demands of the application, such as scheduling different applications in a multifunction scenario. Additionally, this architecture

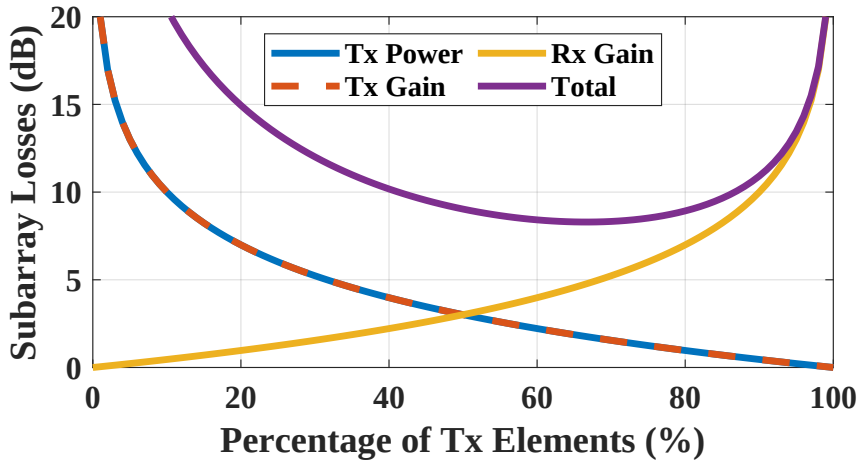


Figure 2.3: System losses associated with the subarray divisions created in aperture-level IBFD arrays, plotted versus the percentage of elements dedicated to transmit.

does not require any RF/analog cancellation stages [73], which not only helps eliminate a potential bandwidth and/or linearity bottleneck, but also removes any associated insertion loss penalties on both transmit and receive. While these benefits are significant, the downside of splitting the aperture into different subarrays is that the antenna-array gain is reduced for both transmit and receive as well as the total transmit power. These theoretical losses are individually plotted in Fig. 2.3 along with the combined total loss associated with the subarray divisions. This analysis assumes that elements are assigned to either transmit or receive, where an even (50%) split yields 3 dB losses for the transmit power and transmit gain (overlapping traces) and the receive gain for a total loss of 9 dB. The minimum total loss is 8.3 dB, and occurs when 68% of the elements are assigned to transmit.

This array-gain reduction is avoided for element-level designs that enable every element in the array to simultaneously transmit and receive, as shown in Fig. 2.2c. This is accomplished by including an antenna interface behind each individual element as well as introducing additional techniques to improve the transmit-receive isolation within each element [16]. These designs also often incorporate analog cancellation stages that not only mitigate the self-interference (SI) at each element, but also reduce the mutual coupling, or crosstalk interference (XI), that is generated from neighboring elements in the array. While this architecture enables maximum usage and flexibility

of the aperture, the required RF/analog cancellation is not straightforward for arrays with an appreciable number of elements, and additionally introduces nontrivial insertion loss that impacts the transmit output power and receive noise figure, as discussed in a subsequent section dedicated to element-level designs [28].

2.3 Aperture-Level IBFD Arrays

2.3.1 Array Architecture

Behind each of the elements shown in Fig. 2.2b reside transmit and receive channels with electronics that enable the arbitrary transmit-receive subarray divisions. There are several different methods of constructing these hardware channels, where selections are often dictated by the operational frequency of the array. For lower frequency applications (i.e. sub-6 GHz), arrays can be designed to directly generate and sample the RF signals with high-speed digital-to-analog converters (DACs) and analog-to-digital converters (ADCs). While this might complicate the digital design, the main benefit of this approach is that the RF/analog frequency-conversion mixer stages are eliminated, which improves the dynamic range of the system by minimizing the creation of local oscillator and nonlinear spurious signals [133].

With this direct-sampling concept in mind, Fig. 2.4 represents the block diagram of an example array with two transmit (left) and two receive (right) channels. Starting with the single transmit channel on the far-left, a DAC is shown to generate a transmit signal that is subsequently filtered to remove the unwanted images and clock frequencies before being amplified by a power amplifier (PA) that is connected to a transmit-receive (T/R) switch and an antenna element within the array. On the other side of that T/R switch are the receiver electronics, which contain a slight modification to the front-end as compared to a traditional array without IBFD. This change is the incorporation of an additional switch that is shown between the T/R switch and the low-noise amplifier (LNA). This switch allows the otherwise inactive receive channels that are connected to the active transmit channels to sample the transmit output through the use of a coupler, or similar

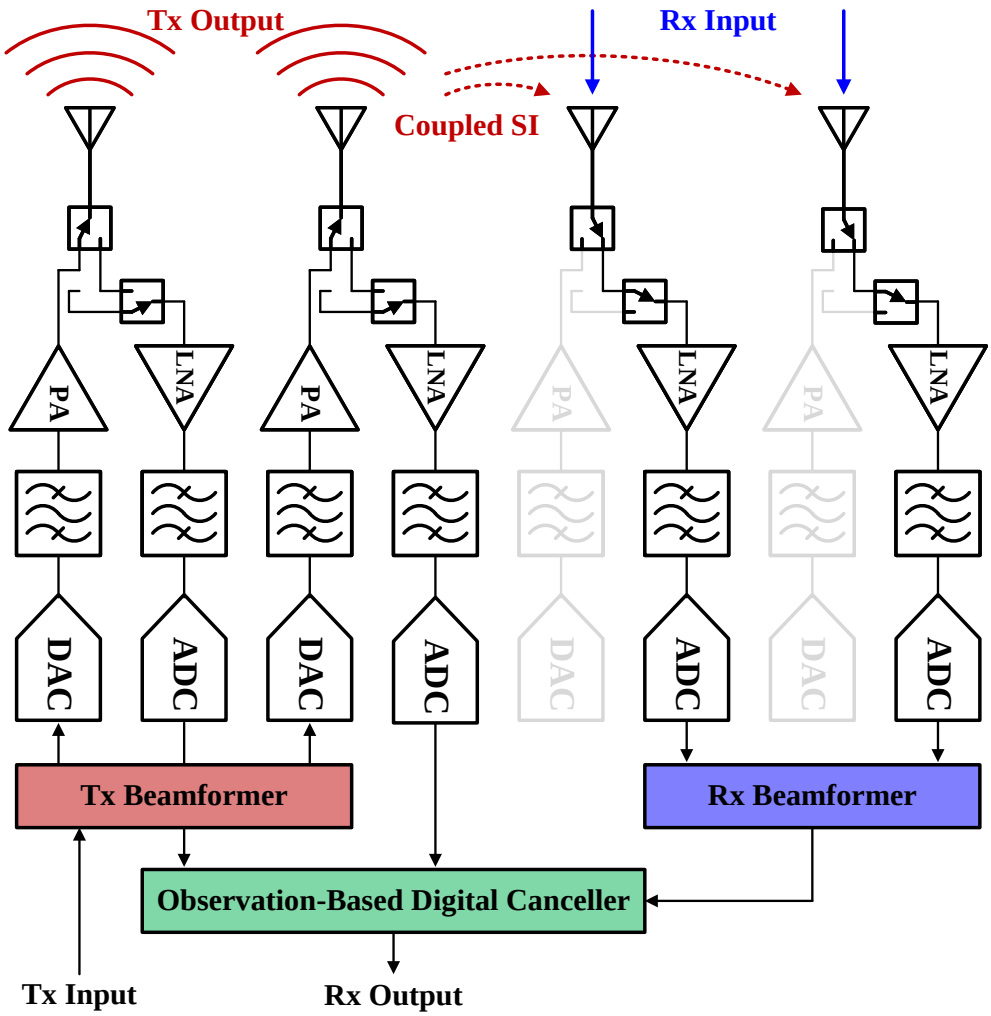


Figure 2.4: Block diagram of an IBFD aperture-level phased array architecture, highlighting adaptive transmit and receive digital beamforming as well as observation-based digital cancellation using observation feedback signals for SIC processing.

device, as shown. The reason for this will be expanded upon in the following subsection.

The top of the image shows the desired transmitted output as well as the unwanted self-interference that couples between the transmit and receive elements of the array. As previously discussed, the elements are spaced at $\lambda/2$ so the coupling levels are often quite significant. When the PAs are outputting an appreciable amount of power, the coupled SI stresses the dynamic range of the receive channels that are attempting to process the SI along with the much-weaker intended receiver input. Together, these signals are filtered after the LNAs and converted using ADCs in

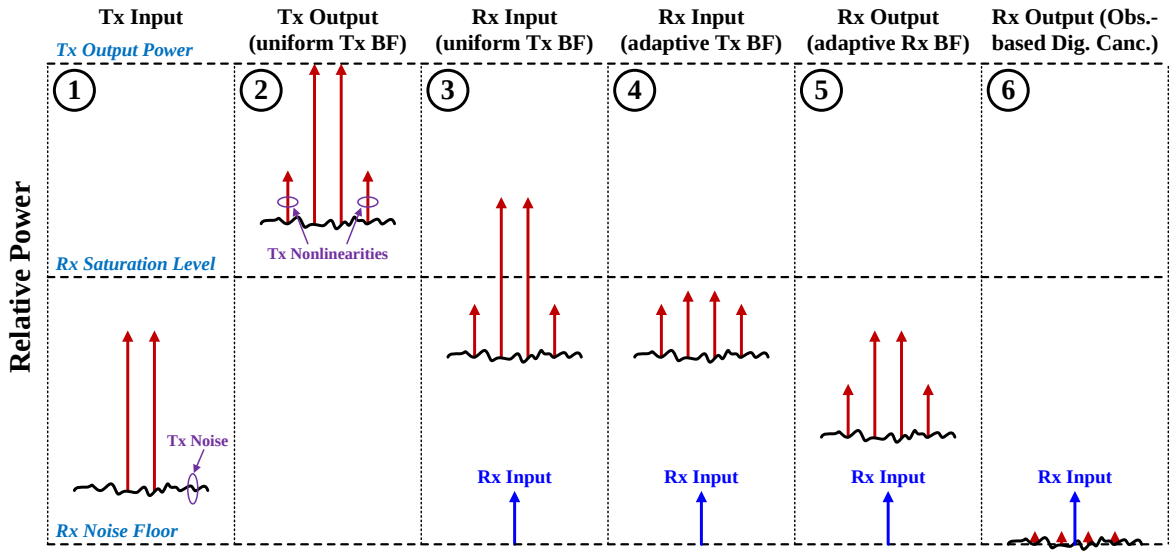


Figure 2.5: Representative power plot showing how the transmit signal, noise and nonlinearities change for each of the processing stages within an IBFD aperture-level phased array.

this direct-sampling architecture. The bottom of Fig. 2.4 depicts digital beamformers connected to the transmit and receive channels, which are traditionally used to weight and electronically alter the far-field pattern of the array. As the next subsection will discuss, these beamformers, along with observation-based digital cancellation, can be used to additionally provide SIC and enable the IBFD operation.

2.3.2 Digitally-enabled SIC Processes

The aperture-level array concept depicted in Fig. 2.2b generates SIC between subarrays within the aperture using a collection of adaptive digital beamforming and cancellation techniques, as previously mentioned [24, 31]. While the connection of these methods was highlighted in the block diagram of Fig. 2.4, their operation and effect on the signals within the array will be discussed here. Fig. 2.5 plots the relative power levels at various points in the transmit and receive channels of the array to illustrate how the signals change during each processing state. Three important power levels are denoted as the receiver noise floor, the receiver saturation level, and the transmit

output power.

Starting on the left, the first part represents a notional transmit signal that is output from a DAC. For illustrative purposes, the signal is simply two tones without any distortions imparted by the DAC, other than a noise level that is imposed by its limited dynamic range, as shown. Assuming a uniform transmit beamformer that weights all the channels equally (i.e. effectively not providing any beamforming), the second part represents the transmit output signals that in addition to the two tones and noise level, now also contain intermodulation distortion that results from the nonlinearities of the transmit channel, which are dominated by those of the PA. It should be noted that more complex waveforms (other than tones) produce nonlinearities that are at the same frequencies as the desired transmit signals, and cannot be removed via conventional filtering, as the image might suggest.

The following parts of Fig. 2.5 illustrate the power levels through the receive channels. The third part depicts the coupled SI that is suppressed by the inherent path loss and directivity of the array at the input of the receivers (still with a uniform transmit beamformer). The main SI components are seen to be above the receiver saturation level, and could also be above the maximum input, or damage level, for cases when the transmit output power is significantly high. The receive input is also shown to be above the receive noise floor and substantially below the coupled SI.

The first SIC stage is represented in the fourth step, which is the application of digital beamforming on the transmit side, where the signal common to each transmit channel (i.e. the two tones) is suppressed in the direction of the receiver elements. This near-field nulling effect can be accomplished with minimal impact to the far-field gain pattern when constraints are applied to the adaptive weight calculation, and has been demonstrated for both omnidirectional [51, 74, 137] and directional arrays [35]. Due to the fact that the transmit nonlinearities and noise are unique to each transmit channel (and power amplifier), they do not coherently subtract at the receiver elements, with the nonlinearities and noise level not changing for this processing stage, as indicated in Fig. 2.5. Overall, the goal of this transmit beamforming task is to reduce the high-power transmit signal below the saturation level of the receiver channels so that it can be processed linearly and

digitized.

The fifth part of the cascade illustrates the effect of the second SIC method that utilizes the digitized receive samples to provide adaptive beamforming on receive. In a similar way to the transmit beamforming, the receive channels are digitally weighted to create a near-field nulling effect that suppresses the coupling of both the transmit signal and uncorrelated noise, as was shown for omnidirectional [13] and directional IBFD systems [28,32]. Since this technique treats both of these components as coming from the same spatial direction in the near-field, both of their receive power levels are reduced. It should be noted that receive beamforming algorithms can simultaneously attempt to mitigate SI in the near-field and suppress traditional external interference in the far-field, where the computations are limited by the degrees-of-freedom of the array, which is one less than the number of elements [17, 94].

The final step, captured in part six of Fig. 2.5, is the application of observation-based digital cancellation using the otherwise-inactive receivers paired with each transmit channel to provide an observation of the actual signals that are transmitted [81, 90]. These signals differ from the ideal transmitted waveforms in that they additionally include the nonlinear components and non-deterministic noise generated, as visualized in the difference between parts one and two of the figure. The linear combination of the feedback from these observation receivers is used to feed a multichannel-digital canceller that allows not only the transmit signal to be subtracted from the received data, but also the transmitter nonlinearities and noise since they were measured. This combination of techniques allows the aperture-level IBFD array system the ability to suppress the transmit signal, nonlinearities and noise below the receiver noise floor, and recover the signal of interest, as shown in the last step, and demonstrated for a representative system in Chapter 6.

2.4 Element-Level IBFD Arrays

2.4.1 Array Architectures

As shown in Fig. 2.2c, element-level IBFD arrays differ from aperture-level designs by allowing every element within the array to simultaneously transmit and receive. While researchers pursuing the aperture-level concept have predominately utilized architectures similar to Fig. 2.4, element-level approaches have varied. This is due to the fact that multiple SIC techniques are available within the RF/analog domain to generate the necessary isolation between the transmit and receive channels for a given element.

Fig. 2.6a illustrates the block diagram of an element-level IBFD array architecture that was demonstrated in [11]. Beginning at the top, each of the N antenna elements are shown to produce SI that is appropriately indexed. In addition to this SI, XI is generated between pairs of elements, such that a XI coupling path exists from each element to every other element in the array for a total of $N^2 - 1$ interference paths (the diagram only indicates the XI originating from the first element for clarity). Similar interference coupling paths exist in the aperture-level approach, but are significantly reduced by the directionality and path loss between the subarrays.

Another requirement of element-level arrays is the inclusion of an antenna-sharing interference, which is fulfilled by the circulator, and connects the transmit and receive channels with the antenna for each element. Below these devices are RF/analog cancellation stages, consisting of tapped delay line structures that can independently adjust their complex weights in an attempt to mitigate the various types of interference [73]. The cancellers on top (in red) sample the transmit output for their corresponding element and focus on reducing the associated SI, while the cancellers below them (in blue) sample the other transmit channels in order to tackle the XI signals. The complexity of the canceller designs varies with signal power and delay spread, where 12 taps were utilized for the SI cancellers, 4 taps for the shorter XI paths (i.e. XI_{2-1}), and 2 taps for the longer XI paths (i.e. XI_{N-1}), for a total of 56 taps for the 3-element array in [11]. These RF/analog cancellation stages reduce both the SI and XI so that they can be linearly processed and digitized

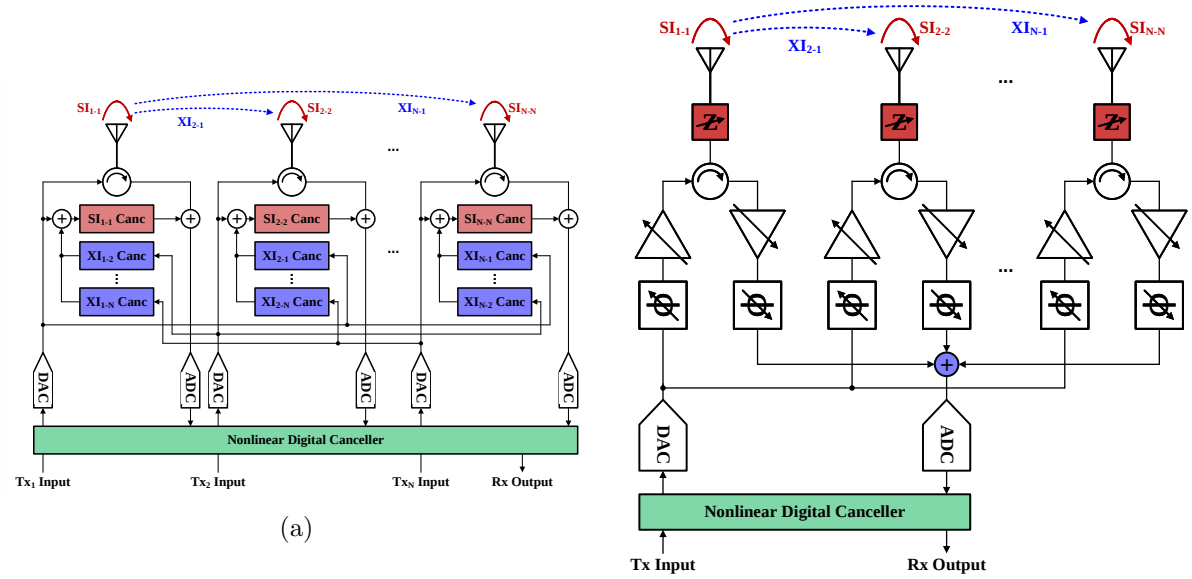


Figure 2.6: Block diagrams of IBFD element-level phased array architectures, highlighting (a) an approach that utilizes RF/analog cancellers, and (b) an approach that employs impedance tuning and RF/analog beamforming before a final nonlinear digital cancellation step.

by the receivers before the application of nonlinear digital cancellation (where the amplification, filtering and frequency conversion components were omitted from the diagram to focus on the IBFD aspects).

An alternative element-level IBFD array architecture that avoids the use of RF/analog cancellers is shown in Fig. 2.6b [28]. The same SI and XI coupling paths are indicated at the top of the diagram for an array with N elements. While this approach also utilizes circulators, it employs an impedance tuner (in red) between them and the antenna elements. This device helps to dynamically match the impedances of the circulators and antennas, such that reflections from the antennas are minimized and the transmit-receive isolation is enhanced. Following the SIC provided by the tuners/circulators, this architecture leverages adaptive beamforming in the RF/analog domain to provide additional interference suppression. Jointly optimizing transmit and receive beamformers using analog components (such as the tunable gain stages and phase shifters shown) allows this design to maximize far-field gain and minimize near-field interference, similar to the aperture-level

Table 2.1: Summary of Measured IBFD Phased Array Systems

Ref	IBFD Type	Arrangement	Tx, Rx #	Total #	F_c (GHz)	BW (MHz)	P_{Tx} (dBm)	Total Isolation (dB)
[32]	Aperture	Linear	4, 4	8	2.45	100	33.3	140.5
[4]	Aperture	Linear	4, 4	8	2.40	20	–	41.4
	Aperture	Linear	8, 8	16	2.40	20	–	45.0
[67]	Aperture	Linear	4, 4	8	2.45	100	33.3	140.5
	Aperture	Linear	4, 4	8	2.45	1	33.3	160.8
[7]	Aperture	Linear	5, 5	10	4.20	1	–	80.0
[35]	Aperture	Rectangle	36, 36	72	2.40	20	0.0	87.0
[158]	Aperture	Square	25, 25	50	10.00	100	–	20.0
[157]	Aperture	Rectangle	30, 10	40	10.00	200	30.0	13.8
[11]	Element	Linear	3, 3	3	2.45	20	20.0	103.0
[28]	Element	Rectangle	8, 8	8	0.73	16	16.5	100.0

approach. It should be noted that the SI and XI signals are suppressed by summing the receive channels with a combiner (in blue), which reduces the interference before the ADC, as shown (where the ancillary RF/analog components were again omitted). After digitization, a nonlinear digital cancellation stage reduces the residual interference.

2.5 IBFD Array Prototypes

2.5.1 Measurement Survey

Due to the number of channels required and their associated hardware costs, phased array systems are expensive to create. With that said, several universities and research organizations have constructed IBFD array prototypes as well as simulated various aspects of their design and performance.

Table 2.1 categorizes measured prototypes based on their IBFD architectural type, and compares the number of antenna elements, their arrangement, operational frequency, bandwidth, and transmit output power per element as well as the reported total isolation achieved. It is evident that many researchers have chosen to focus on designs revolving around the aperture-level archi-

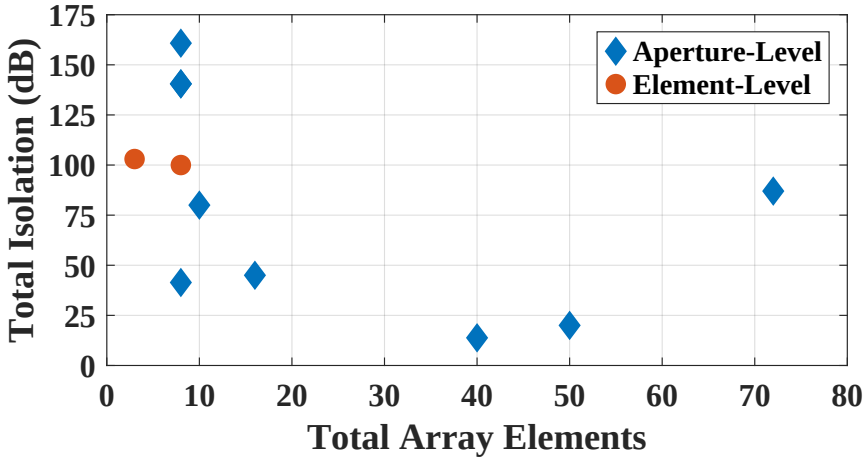


Figure 2.7: Survey of total isolation versus the total number of array elements for measured IBFD phased array systems with aperture- and element-level architectures.

tecture as opposed to element-level approaches. The array sizes are seen to vary from 3 up to 72 elements, and have arrangement types that include both one (linear) and two dimensions (square and rectangular). The design frequencies range from 0.73 to 10 GHz with instantaneous bandwidths spanning 1 to 200 MHz. While not every publication reported the element transmit output power, the maximum was found to be +33 dBm, or 2 Watts.

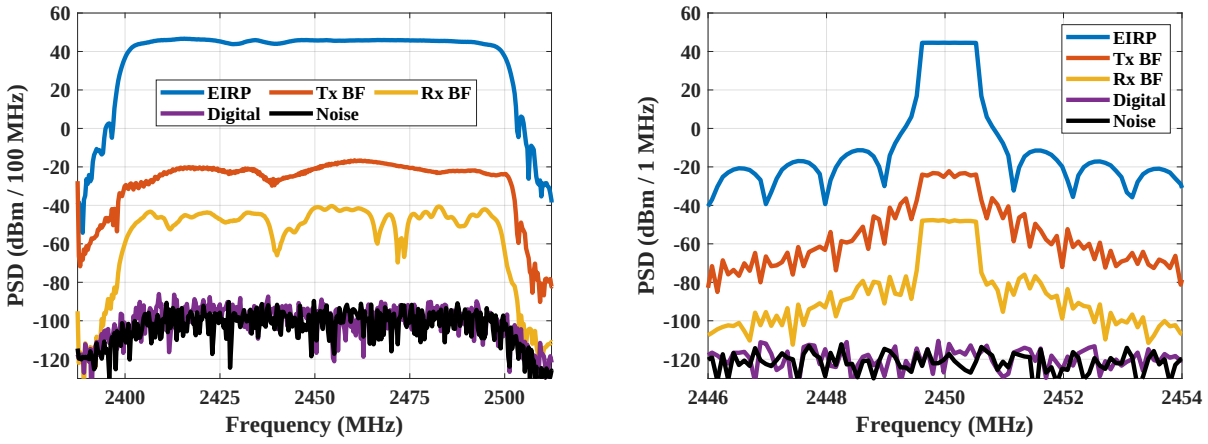
The total isolation achieved by these systems is seen to vary over a wide range, and is influenced by the output power level and bandwidth, where the highest isolation was reported as 160.8 dB for a narrowband measurement of a high-power prototype. For a more visual representation of this data, Fig. 2.7 plots the total isolation reported versus the total number of array elements, and distinguishes between the aperture- and element-level architectures. Ideally, this comparison table would also include numbers on power consumption per element and system losses due to implementing IBFD operation; however, these metrics were not reported in the research publications.

Regarding the simulation contributions, Table 2.2 summarizes IBFD-array publications that have modeled various aspects of the different architectures and element arrangements. It shows that element counts up to 100 have been considered for arrays with operating frequencies up to 28 GHz. This table also lists the main focus and simulation contributions of each paper to provide readers

Table 2.2: Summary of Simulated IBFD Phased Array Systems

Ref	**IBFD Type**	**Arrangement**	**Tx, Rx #**	**Total #**	**F_c (GHz)**	**Simulation Focus**
[31]	Aperture	Rectangle	25, 25	50	2.45	Coupling, SIC and beamfomer losses
[24]	Aperture	Rectangle	25, 25	50	2.42	SIC, noise and beamformer losses over scan angle
[125]	Aperture	Square	50, 50	100	28.00	SIC for sparse arrays with circular polarization
[138]	Aperture	Square	50, 50	100	22.50	Coupling for different boundary conditions
[33]	Aperture	Rectangle	25, 25	50	2.45	SIC of multi-channel analog cancellation networks
[47]	Aperture	Linear	16, 16	32	28.00	Coupling and scan performance for linear arrays
[154]	Aperture	Rectangle	4, 4	8	10.00	Beamformer optimization with unique algorithm
[52]	Aperture	Rectangle	16, 16	32	4.3	Joint design of sparse arrays and beamforming
[87]	Aperture	Rectangle	36, 36	72	28.00	Tx/Rx beamformer design on per-antenna basis
[53]	Aperture	Rectangle	16, 16	32	4.3	Beamforming and digital cancellation comparison
[86]	Aperture	Rectangle	36, 36	72	28.00	Tx analog beamformer with quantization per-antenna
[15]	Aperture	Rectangle	36, 36	72	2.40	Rate gains and beamformer losses using measured data
	Element	Rectangle	8, 8	8	1.65	
[149]	Element	Rectangle	32, 32	32	–	Beamformer losses for different algorithms

with a quick summary to pique their interest for further investigation. While many have focused on different facets of SIC, other topics have included the analysis of beamformer losses, optimization algorithms, and data rate gains for these systems. While both of these tables highlight the fact that aperture-level architectures have dominated the focus of research to date, overall knowledge of IBFD arrays is limited and continuing to progress.



(a) (b)

Figure 2.8: Aperture-level IBFD array performance, showing power spectral density (PSD) with various SIC techniques including adaptive Tx and Rx beamforming (Tx/Rx BF) and digital cancellation over (a) 100-MHz and (b) 1-MHz bandwidthds from [67].

2.5.2 Results and Challenges

In order to provide more insight into the designs highlighted in Table 2.1, the results and challenges of the highest-performing systems will be discussed here for both aperture- and element-level architectures. Specifically, the SIC and XI cancellation (XIC), or total isolation, performance will be analyzed for the different mitigation strategies, and their associated system losses will be examined.

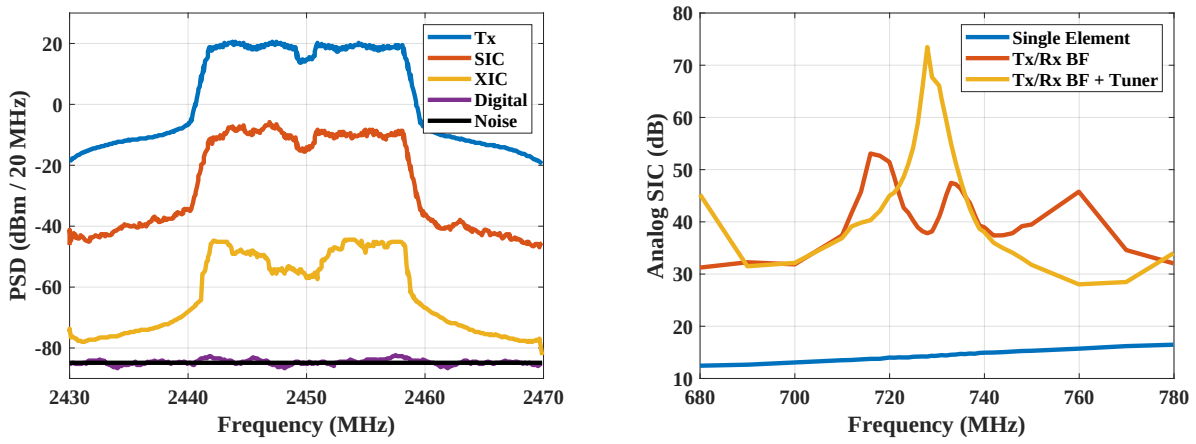
Beginning with the aperture-level IBFD array presented in [32, 67] with the architecture depicted in Fig. 2.4, an example of the SIC performance over a 100-MHz bandwidth centered at 2.45 GHz can be seen in the power spectral density (PSD) plot of Fig. 2.8a. This measurement was conducted using an 8-element linear array in an anechoic chamber and allowed the beamforming and cancellation techniques to be evaluated without any multipath effects. The effective isotropic radiated power (EIRP) for the array was 44.8 dBm, which was the result of combining the array gain of 11.5 dBi and 33.3 dBm total output power with uniform transmit beamforming. Adapting the transmit weights with the objective of reducing the coupling power as well as not sacrificing the main transmit beam performance resulted in reducing the SI at the receive elements to less than

−22 dBm. Adaptive receive beamforming further lowered the interference to −46.3 dBm, while also removing some of the transmit noise, as visualized in the smoothness of the residual signal. The observation-based digital cancellation process then decreased the residual to −96.1 dBm, which was 2.5 dB above the noise floor, and yielded a total of 140.5 dB of transmit-receive isolation.

These same processes were repeated for a signal with a 1-MHz bandwidth, as represented in the measured results of Fig. 2.8b. This plot demonstrates a similar EIRP (44.5 dBm) and SI decrease near the noise floor (2.2 dB above) for a total isolation of 160.8 dB, which signifies that this approach scales with signal bandwidth and corresponding noise floor changes.

While this aperture-level architecture was demonstrated to offer a fairly straightforward path to high output power and near-optimal SI reduction, there are two distinct challenges to overcome before widespread adoption. The first relates to the front-end hardware modification of traditional arrays that allows for the transmit output signals to be sampled and fed into the observation-based digital canceller. This unique set of switches and couplers should have a high dynamic range, provide the ability to operate over different output powers and exhibit low loss, such that the losses after the PAs and system noise figure are comparable to arrays with standard T/R switches. Initial research targeting this problem using GaN-based MMICs at both S- and X-bands shows promising results [57]. The second challenge relates to the beamforming algorithms, and the need to simultaneously satisfy the goals of minimally impacting the far-field gain while also providing near-field SIC. While the prototype presented in [32, 67] successfully demonstrated SIC with far-field main-beam transmit/receive gain reductions of less than 0.5 dB as a result of the beamforming operations, the algorithm did not run in real-time. This can potentially be improved by incorporating neural networks that can be implemented on field-programmable gate arrays (FPGAs), but still needs to be proven as the array size increases [25].

The first element-level architecture, demonstrated in [11] and illustrated in Fig. 2.6a, reported SI and XI reductions over a 20 MHz bandwidth centered at 2.45 GHz, as shown in Fig. 2.9a. The circulator isolation and SI cancellation provides 30 dB of suppression, which reduces the +20 dBm transmit output power to −10 dBm. The XI signal levels are then decreased by 40 dB using their



(a) (b)

Figure 2.9: Element-level IBFD array performance, showing (a) power spectral density (PSD) with various SIC and XIC techniques and digital cancellation over a 20-MHz bandwidth from [11], and (b) analog SIC performance for adaptive analog Tx and Rx beamforming (Tx/Rx BF) and antenna-impedance tuning, compared to the native isolation of a single element from [28].

corresponding cancellers, which lowers the total interference power to −50 dBm. The remaining signal is then sampled and further suppressed by an additional 33 dB using digital cancellation, bringing the residual to −83 dBm, which was 1.6 dB above the receiver noise floor. With 70 dB of RF/analog cancellation, this 3-element prototype produced 103 dB of total isolation.

The second element-level design, presented in [28] and shown in Fig. 2.6b, reported RF/analog-domain SIC over a 16.25-MHz bandwidth centered at 730 MHz, as shown in Fig. 2.9b. The nominal transmit-receive isolation for a single element was measured to be roughly 15 dB, where the addition of the adaptive transmit and receive analog beamforming increased the SIC to 40.7 dB. For the beamforming algorithm, the far-field array gains for both transmit and receive were permitted to degrade by 3 dB. Simultaneously optimizing the beamforming weights and the antenna-impedance tuners provided a total RF/analog SIC of 50 dB. This was later combined with another 50 dB of SIC using digital cancellation, and yielded a total isolation of 100 dB for the 2×4-element array.

While not strictly phased arrays in the sense that we have discussed (since they do not maintain a traditional $\lambda/2$-lattice spacing), multiple-input multiple-output (MIMO) systems can

be created with directional elements and be outfitted for IBFD operation. In order to provide a sense of their performance, the work of [28] was extended to a 2-channel MIMO architecture that used RF and baseband SIC along with integrated circulators to produce 45 dB of SIC over a 20 MHz band centered at 2.2 GHz along with 53 dB XIC over the same band [8]. Additionally, a 4-channel IBFD MIMO front-end was demonstrated to provide 44 dB of combined SIC and XIC using a quadrature balanced power amplifier (QBPA) topology and wideband digital interference cancellation [39], and another front-end employed a common-mode-suppression balun to provide a passive SIC of 64.5 dB [37]. While the performance of the individual MIMO channels can influence the design of those in $\lambda/2$-spaced arrays, the isolation gained through spatial antenna separation must be considered.

Similar to these MIMO systems, both of the element-level designs face hardware-related challenges − the former approach needing to tackle how to efficiently incorporate and tune all of the RF/analog canceller taps within each element, and the latter being limited to a single receive beam due to the analog combination scheme feeding a single ADC. Additionally, each architecture must contend with high-speed RF signal routing between the elements to accomplish its intended SIC: the first needs to route the necessary canceller inputs, while the second must route the receive signals into the combiner. This physical-routing obstacle can more broadly be categorized as a scaling challenge, which is also common to aperture-level designs, and additionally pushes into the digital computing realm as all of these IBFD arrays utilize digital SIC processing as the final mitigation step. The following section outlines some future research directions that can be pursued to help overcome these scalability challenges.

2.6 Chapter Conclusion

This chapter provides an overview of the state-of-the-art IBFD phased array implementations that could be used to create simultaneous-multifunction systems. Various IBFD array architectures are presented with a focus on aperture- and element-level approaches. The former divides the aperture into transmit and receive subarrays, and utilizes digitally-enabled SIC processes to create

isolation between the subarrays. The latter allows the same antenna in each element to simultaneously transmit and receive, and requires an RF/analog-based cancellation scheme to reduce interference before digitization and further suppression. A survey of measured IBFD array prototypes as well as their results and limitations are discussed, which highlighted the need for additional research on the physical and computational scalability of IBFD arrays before being able to support future multifunction systems.

Future work on the scalability of IBFD arrays can be broken down into two major categories: the physical array panels themselves and the digital signal processing hosted on them. Many of the prototypes discussed within this chapter were designed with a modest number of antenna elements and could not easily cascade additional elements and hardware channels to change the array size beyond their initial proof of concept. This can be improved by focusing on the unit panel design of an array that could ideally be tiled in both horizontal and vertical directions to create arrays of arbitrary sizes [43, 64]. The cost of including IBFD capability within these panels could be minimized by incorporating the IBFD-enabling circuits directly into integrated front-end designs, as discussed in Chapters 4 and 5.

For the digital signal processing aspect, integrating a compact digital computing solution on the array itself, not only allows the local management of resources for simultaneous-multifunction operation, but also provides an option to output actionable data products instead of raw data samples [29, 152]. This seamless digital-data sharing is critical for scalable-SIC approaches to reduce the computational complexity and overall power consumption as the array size grows to support multiple functions and deployment scenarios [69]. Parts of the material presented in this chapter are reported in [77] and [78].

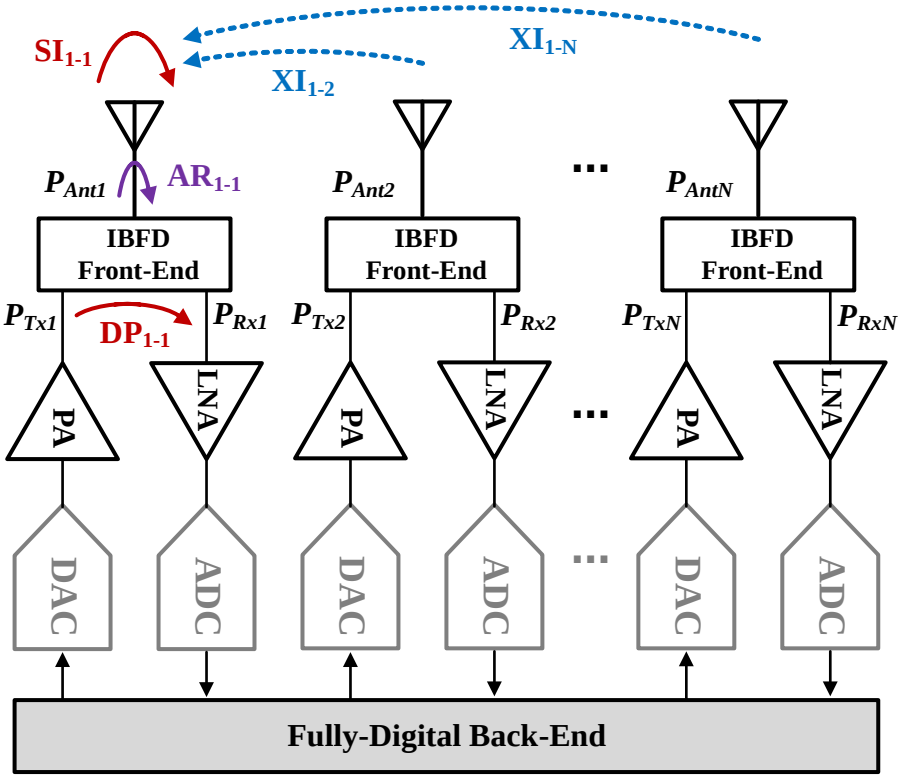
Chapter 3

Mutual Coupling and System Requirements

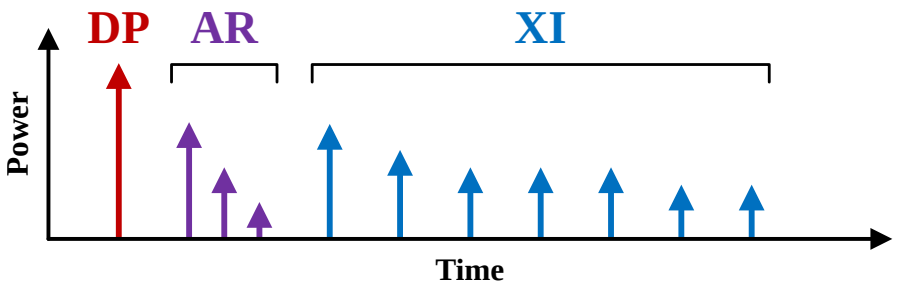
3.1 Introduction

While the previous chapter provides an overview of IBFD arrays as well as preexisting aperture- and element-level approaches, this chapter discusses the cancellation requirements for these systems, focusing on the IBFD front-ends that see the highest self-interference (SI) power levels. Fig. 3.1 illustrates the block diagram of a generic array that can provide IBFD operation at either the aperture- or element-level, depending on the configuration. This architecture leverages a fully-digital back-end that consists of digital-to-analog converters (DACs) and analog-to-digital converters (ADCs) for every element. While not a necessary condition for IBFD arrays, the flexibility provided by this digital-at-every-element approach is useful when employing digital beamforming and parallel signal processing. In addition to the data converters, the location of power amplifiers (PAs) and low-noise amplifiers (LNAs) is depicted to provide a sense of the where the high-power signals (P_{Tx}) are generated and where the coupled SI is received (P_{Rx}), respectively. It should be noted that supplementary components, such as filters, mixers and gain blocks, are also often incorporated into these systems, but are not necessary for the discussion of the front-end requirements.

When architecting IBFD systems, it is helpful to understand the different types of signals that comprise the SI. This allows designers to gain an appreciation of how these signals are generated and how best to tailor mitigation techniques to address them. The upper part of Fig. 3.1 highlights the various interference types that must be considered for a generic IBFD array, and only shows those related to the first element for clarity. The direct path (DP) interference has the shortest



(a)



(b)

Figure 3.1: (a) Diagram of generic IBFD array system, highlighting the self-interference (SI) and crosstalk inteference (XI) for the first element as well as the critical power levels for the IBFD front-end, and (b) time-domain example response for the direct path (DP), antenna reflection (AR) and XI signals.

delay between the transmitter and receiver within an element, representing the SI component that arrives first at the receiver, as depicted in the example time-domain response shown in Fig. 3.1b. Antenna reflections (ARs) arise from the fact that the antenna is not perfectly impedance-matched to the front-end, and thus generates a reflection-based copy of the transmit signal that has a slightly

longer delay compared to the DP and could consist of multiple reflections that decay over time. Together, the DP and AR interferences comprise the SI within each element, and can be thought of differently for aperture- and element-level approaches. While both architectures utilize the transmit elements to simultaneously receive, the difference arises in their signals-of-interest and associated receiver sensitivities.

For aperture-level designs, the receivers connected to active-transmit elements are interested in digitizing the individual transmit signals to provide an observation path that can have a significant amount of attenuation. As seen in the previous chapter, this can be accomplished using front-ends that consist of transmit/receive switches and attenuators to sufficiently suppress the DP and AR signals so they do not saturate the receivers and can be digitized for subsequent cancellation. For element-level designs, however, each receiver is attempting to capture signals-of-interest with low signal-to-noise ratios (SNRs) from distant sources, and thus must maintain their nominal low-sensitivity levels. Associated element-level IBFD front-ends must then be designed to handle, and ideally suppress, both DP and AR interferences to avoid receiver saturation.

The additional consideration of cross-talk interference (XI) is important for both design types, and represents interference that arrives at the receiver later than the DP and AR signals. This XI depends on mutual coupling between the elements with an array, and will be discussed in the following sections.

3.2 Mutual Coupling Overview

Mutual coupling is defined as the electromagnetic interaction between nearby antenna elements in an array, which causes them to affect the overall performance by changing the input impedance of the individual antenna elements as well as the radiation pattern of the array itself [2, 134]. This phenomenon influences the amount of transmit energy that leaks into any elements attempting to simultaneously receive, and is also a concern for arrays where every element is transmitting since they unintentionally receive energy from their neighbors, which changes their characteristics. These changes are dependent on the transmitted and coupled power, which are

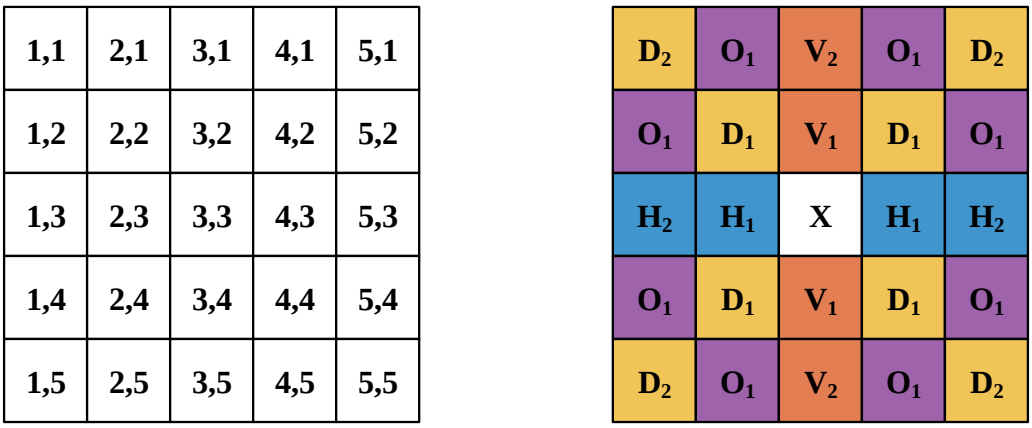
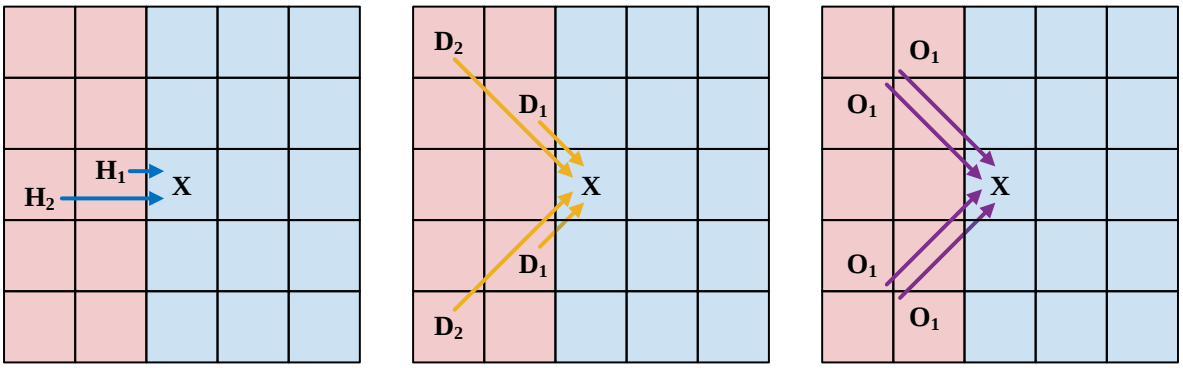


Figure 3.2: Designators for a 25-element 5×5 array based on (a) physical location and (b) mutual coupling groups: horizontal (H); vertical (V); diagonal (D); and off-diagonal (O) relative to the center element (X).

inversely proportional to the element spacing within the array [12]. While reducing the effects of mutual coupling has been studied to improve the scanning performance for traditional half-duplex arrays, research has not focused on the reduction of mutual coupling, or XI, for IBFD applications [83, 84].

An intuition can be gained into the mutual coupling effects on IBFD front-ends by analyzing a notional two-dimensional (2D) 5×5 array with 25 total elements, as depicted in Fig. 3.2a. Each box within this diagram represents an antenna element with the numbering of the individual elements based on their location. Due to the physical symmetry of most arrays, the mutual coupling paths between elements are often similar and can be grouped into different categories, as illustrated in Fig. 3.2b. If the mutual coupling to the center element of the array (location 3,3) is considered and denoted with an X, four different groups can be drawn based on the coupling planes of the 2D geometry: horizontal (H); vertical (V); diagonal (D); and off-diagonal (O); where the subscripts represent the number of elements from the center. With this framework in place, the differences in the mutual coupling considerations between aperture- and element-level IBFD arrays can now be discussed.

As mentioned in the previous chapter, aperture-level architectures partition the elements



(a) (b) (c)

Figure 3.3: Aperture-level IBFD array coupling for a 5×5 array with two transmit columns and three receive columns, highlighting the (a) horizontal (H), (b) diagonal (D), and (c) off-diagonal (O) paths to the center element (X).

into transmit and receive subarrays, where the coupling at the boundary between these zones is the highest. Fig. 3.3a depicts an aperture-level configuration for the 5×5 array where the array is divided such that the two left columns represent transmit elements and the three right columns represent receive elements. This figure also highlights the horizontal coupling paths between the two transmit elements to the left of the center element being considered. It should be noted that no vertical coupling paths exist for this scenario − since the elements above and below the center are not transmitting − but that alternate aperture-level subarray divisions could introduce those paths. Figs. 3.3b and 3.3c similarly depict the diagonal and off-diagonal coupling paths for this array configuration, respectively. For this example, there are a total of 10 transmitting elements, and thus, a total of 10 different XI signals with associated coupling paths that exist to the center receive element.

For an element-level IBFD array where every element is simultaneously transmitting and receiving, Fig. 3.4a illustrates the corresponding horizontal and vertical coupling paths to the center element. Similarly, Figs. 3.4b and 3.4c highlight the diagonal and off-diagonal coupling. In this case, all 25 elements are transmitting, which creates 24 unique XI signals into the center element (the transmission of the center element itself is classified as SI). For both IBFD array types, the

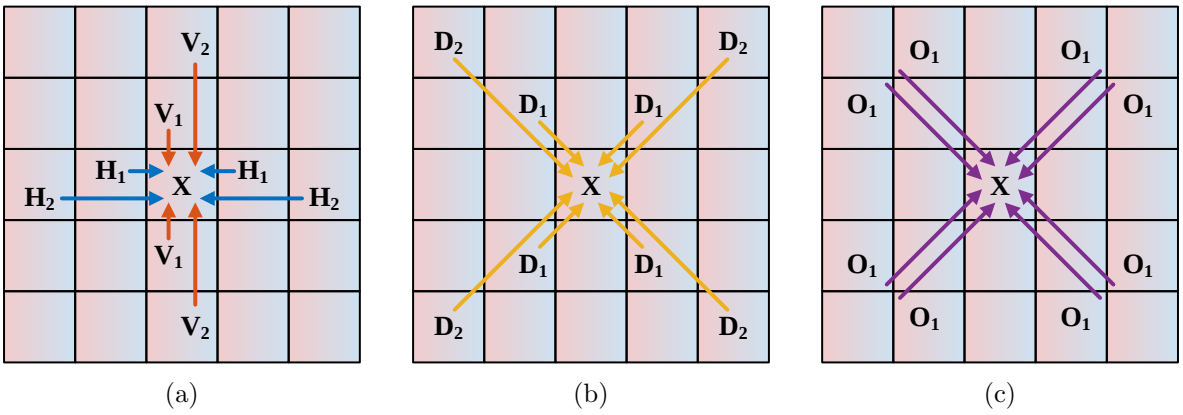


Figure 3.4: Element-level IBFD array coupling for a 5×5 array, highlighting the (a) horizontal (H) and vertical (V), (b) diagonal (D), and (c) off-diagonal (O) paths to the center element (X).

strength of these XI signals is dependent on the mutual coupling between the array elements. Each architecture greatly benefits from utilizing arrays with low-mutual coupling so they can operate at higher transmit powers and avoid receiver saturation. An investigation of mutual coupling reduction techniques is discussed next.

3.3 Coupling-Reduction Techniques

This section presents the investigation of mutual coupling within a patch-based array, and utilizes a 7-element linear structure that can be scaled in two dimensions for either aperture- or element-level IBFD arrays. The coupling differences between the E- and H-planes are discussed, and the simulated results of several different coupling-reduction techniques are summarized with the goal of better understanding the mechanisms that control the coupling in both planes.

As seen in Fig. 3.5a, the unit cell within the array is a square patch that has a length and width of 870 mils and is placed on top of a ground-backed FR4 substrate with 250 mil thickness and 1968 mil extent, which provides the array with a $\lambda/2$ spacing at 3.0 GHz. The patch is differentially fed using coaxial probes to provide symmetric coupling to neighboring elements, where the E-plane is between the probes and the H-plane is perpendicular to it, as depicted in the top view of Fig. 3.5b. The unit cell exhibits an S11 magnitude less than -25 dB and a gain of 5 dBi for broadside radiation

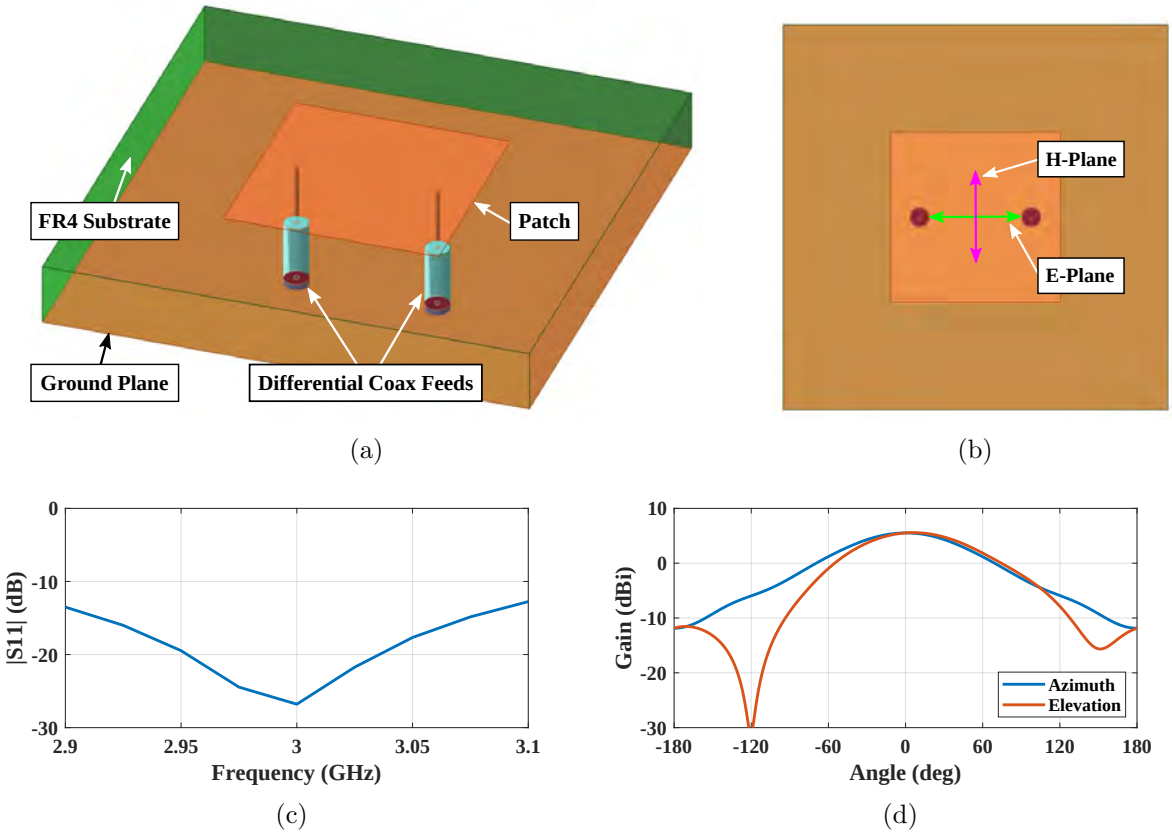
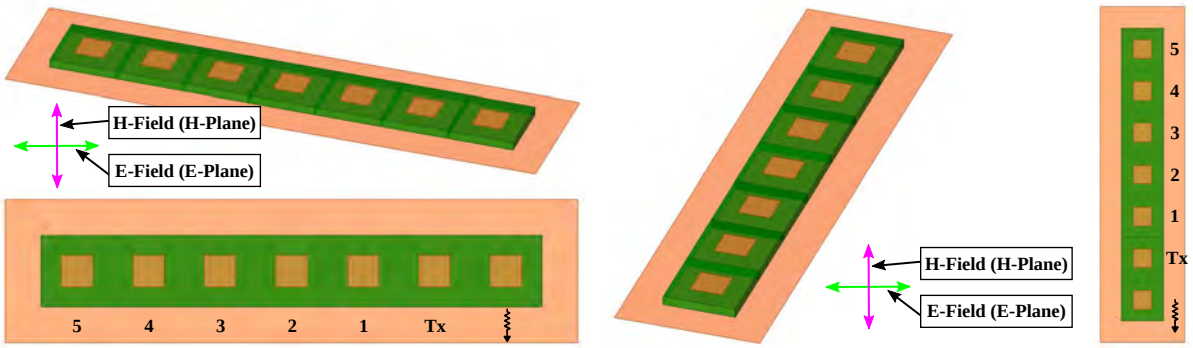


Figure 3.5: Unit cell used for the mutual coupling reduction investigation, highlighting the (a) isometric and (b) top model views, (c) simulated S11 magnitude, and (d) simulated gain.

at 3.0 GHz, as plotted in Figs. 3.5c and 3.5d, respectively.

From this unit cell, an array over an extended ground plane is created by orienting the differential probes along the horizontal axis of the linear array such that coupling occurs in the E-plane, as seen in Fig. 3.6a. Similarly, another 7-element array was created by combining the unit cells in the opposite direction so that the differential probes are perpendicular to the array orientation, which produced coupling between elements in the H-plane, as illustrated in the vertical arrangement of Fig. 3.6b. Both of these images also depict the transmit element that was active and generated coupling to elements numbered 1 through 5 and was adjacent to a terminated element to minimize the array edge effects.

The nominal E-field magnitude with the Tx element active is plotted on the E-plane array

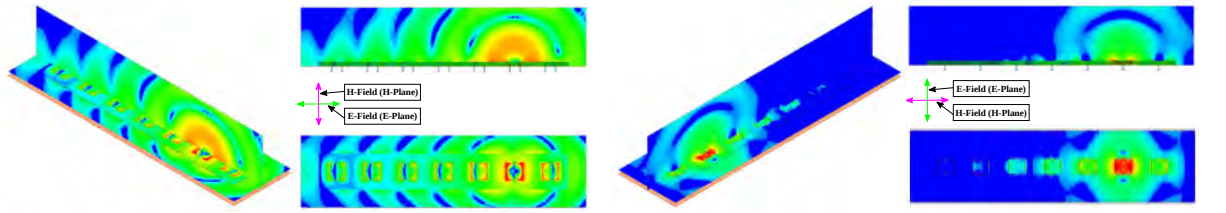


(a) (b)

Figure 3.6: Baseline 7-element linear array models used for investigation of mutual coupling in the (a) E- and (b) H-planes, highlighting the simulated Tx next to a terminated element and coupling into elements 1 through 5.

surface and in the direction of radiation for the isometric, side and top views shown in Fig. 3.7a. As expected, the E-field intensity is seen to be highest for elements close to the Tx and decays with distance. Similarly, the nominal H-field magnitude is depicted on the H-plane array surface and radiation direction when the Tx source is active, as seen in Fig. 3.7b for isometric, side and top views. It should be noted that the array is rotated and subsequently the E- and H-field vectors swapped for the figure. Comparable to the E-field, this image also illustrates that the H-field is strongest near the Tx element, but that it decays more rapidly with distance as compared to the E-field. The quantitative mutual coupling for these two cases is represented in Fig. 3.8 for the different element numbers indicated in Figs. 3.6a and 3.6b. The plot illustrates that the H-plane coupling is stronger than that of the E-plane for the first neighboring element, but it then decreases faster than the E-plane coupling for the elements further from the Tx source, which agrees with previous findings [55, 116].

With a mutual coupling baseline established, different techniques to reduce the coupling between array elements can be considered. While there are many options available, this investigation focused on four unique approaches, namely the introduction of: metallic posts, metallic walls, electromagnetic bandgap structures (EBGs), and defected ground structures (DGSs). These modifications were introduced between the array elements in order to minimize the coupling between



(a) (b)

Figure 3.7: Baseline E- and H-field magnitudes for the (a) E- and (b) H-planes arrays.

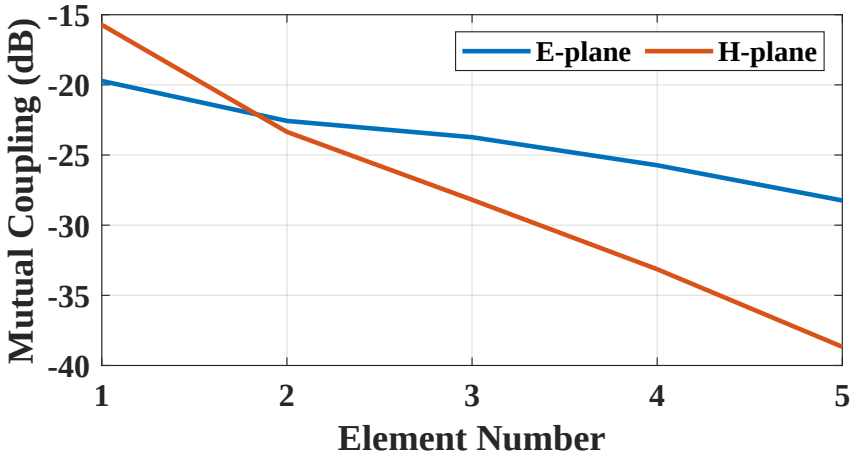
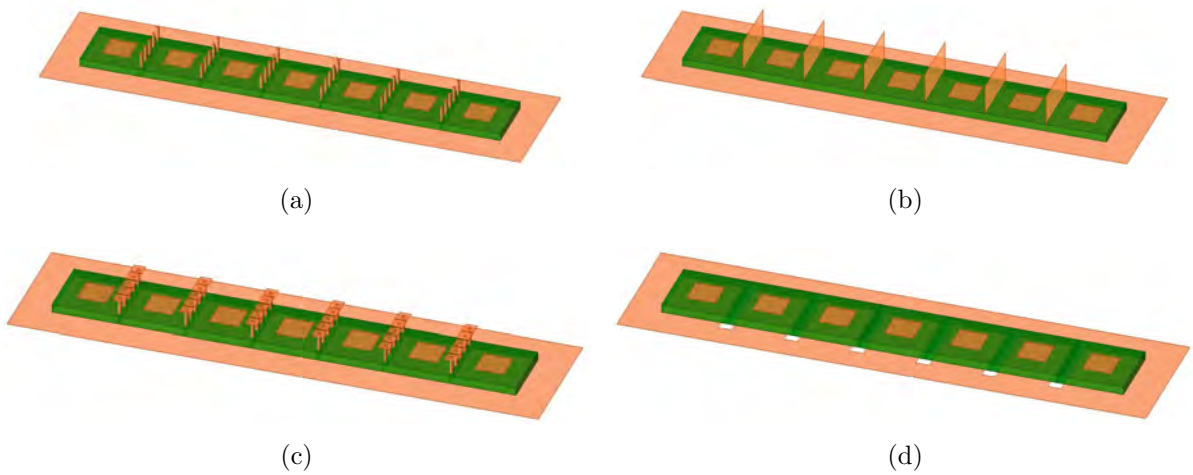


Figure 3.8: Simulated mutual coupling from the active Tx to elements 1 through 5 for the baseline 7-element E- and H-plane arrays. Reprinted from [68].

them, and are depicted for the E-plane array in Fig. 3.9, respectively. For each of the techniques, several aspects of the physical structures were varied to determine their impact on the mutual coupling. While detailed results for each of these are presented in Appendix A, a summary of the the mutual coupling changes is provided in Table 3.1.

3.4 Reduced-Coupling Array

Based on the mutual coupling reduction techniques analyzed in the previous section, a 25-element array was designed with a 5×5 configuration that matches the diagrams and designators referenced in Fig. 3.2. Similar to before, the array design leveraged a rectangular patch element that was modified to facilitate the fabrication of a prototype. While the unit cell was similarly



(a) (b) (c) (d)

Figure 3.9: Array models with mutual coupling reduction techniques inserted between the elements, including (a) metallic posts; (b) metallic walls; (c) electromagnetic bandgap structures (EBGs); and (d) defected ground structures (DGSs).

Table 3.1: Summary of Simulated Coupling-Reduction Techniques

Reduction Technique/ Element#	**Mutual Coupling Change (dB)**									
	E-Plane					**H-Plane**				
	1	**2**	**3**	**4**	**5**	**1**	**2**	**3**	**4**	**5**
Posts	2.0	−2.1	−1.8	−4.1	−6.5	2.7	2.4	0.1	−7.7	−9.5
Walls	2.3	−8.8	−8.7	−10.7	−14.4	−7.4	−12.9	−14.5	−15.5	−16.6
EBG	4.1	−7.6	−7.8	−10.2	−13.5	−2.9	−6.9	−5.9	−4.0	−2.5
DGS	0.7	−1.1	−2.3	−3.5	−5.3	−6.1	−7.7	−8.7	−6.8	−4.6

constructed using an FR4 substrate with a ground plane on the bottom side, the notable changes from the one presented in Fig. 3.5 include switching to a single-ended coaxial feed (eliminating the need for an external balun) and reducing the substrate thickness to a standard height of 62 mils (unintentionally narrowing the radiation bandwidth). Since various aspects of the unit cell are modified between the different array configurations, a focus has been placed on the larger array performance, as discussed in the following sections.

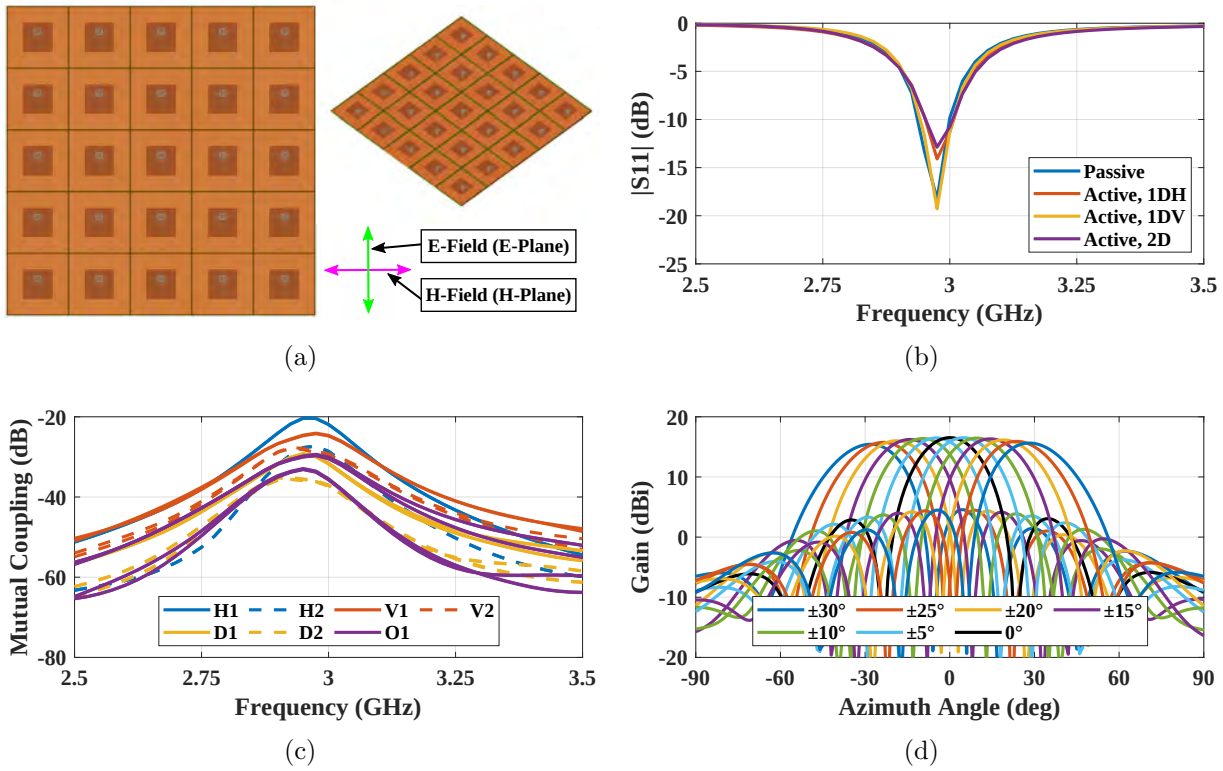


Figure 3.10: Baseline 25-element patch array: (a) top and isometric model views with field directions indicated; (b) simulated S11 magnitude for passive and active (1D horizontal, 1D vertical and 2D) configurations; (c) simulated mutual coupling to center element for the locations referenced in Fig. 3.4; and (d) simulated azimuth gain patterns for different scan angles.

3.4.1 Baseline Design

All of the array simulations were conducted using Ansys HFSS, where the unit cell was first verified in an infinite-array setup with boundary conditions defined using two lattice pairs on the sides and a perfectly matched radiation layer on top. This allowed for the patch size and feed location to be optimized for radiation at 3 GHz, and leveraged the coaxial feed dimensions for a standard surface-mount SMA connector located behind each element.

Fig. 3.10a shows the top and isometric views of the baseline 5×5 array model along with the E- and H-field directions (and associated planes), as dictated by the feed location in the upper-center part of each patch. The unit cell is sized for a 1/2-λ spacing at 3 GHz, which translates to approximately 2 inches (specifically 1968 mils) and produces an overall array size just under 10 inches

(9840 mils exactly). In between each of the patches is a set of vias that extend from the ground plane to the top of the board, which helps provide some initial isolation between the elements within the substrate. The S11 magnitudes for the center element are plotted in Fig. 3.10b for the passive case, where only the center element is transmitting and all of the others are terminated, as well as three active cases based on different array configurations. These include when the transmitters are assigned to a subset of the elements in 1×5 1D horizontal (1DH) and 5×1 1D vertical (1DV) setups (where unused elements are terminated) as well as the full 5×5 2D configuration. The plot indicates that there are slight differences between S11 for these diverse cases, but that overall, the array is well-matched near 3 GHz.

The critical mutual coupling performance is depicted in Fig. 3.10c for the different horizontal (H); vertical (V); diagonal (D); and off-diagonal (O) paths defined in Fig. 3.4. As expected, the adjacent elements produce the strongest coupling values, with −20.4 dB from the horizontal (H1) and −24.1 dB from the vertical (V1) locations. This agrees with the results presented in Fig. 3.8, indicating that the H-plane exhibits stronger coupling than the E-plane for the first neighboring element. The strongest diagonal and off-diagonal values are around −29 dB, and, unsurprisingly, elements further from the center in each direction exhibit lower coupling values.

Additionally, the array gain for the full 2D 5×5 configuration was simulated for different azimuth scanning angles between ±30 degrees, as seen in Fig. 3.10d. While the gain is plotted versus azimuth angle, the results are the same in elevation due to the symmetric nature of the square array. All of the elements are uniformly fed, which produces a maximum gain of 16.5 dBi at broadside (0 degrees) with standard sidelobes of −13 dBc relative to the main beam. Overall, the beam performance is seen to be consistent for the different scan angles. Together, these results can be used to provide a baseline set of metrics for a standard array, and can be compared to a modified design that focuses on reducing the mutual coupling.

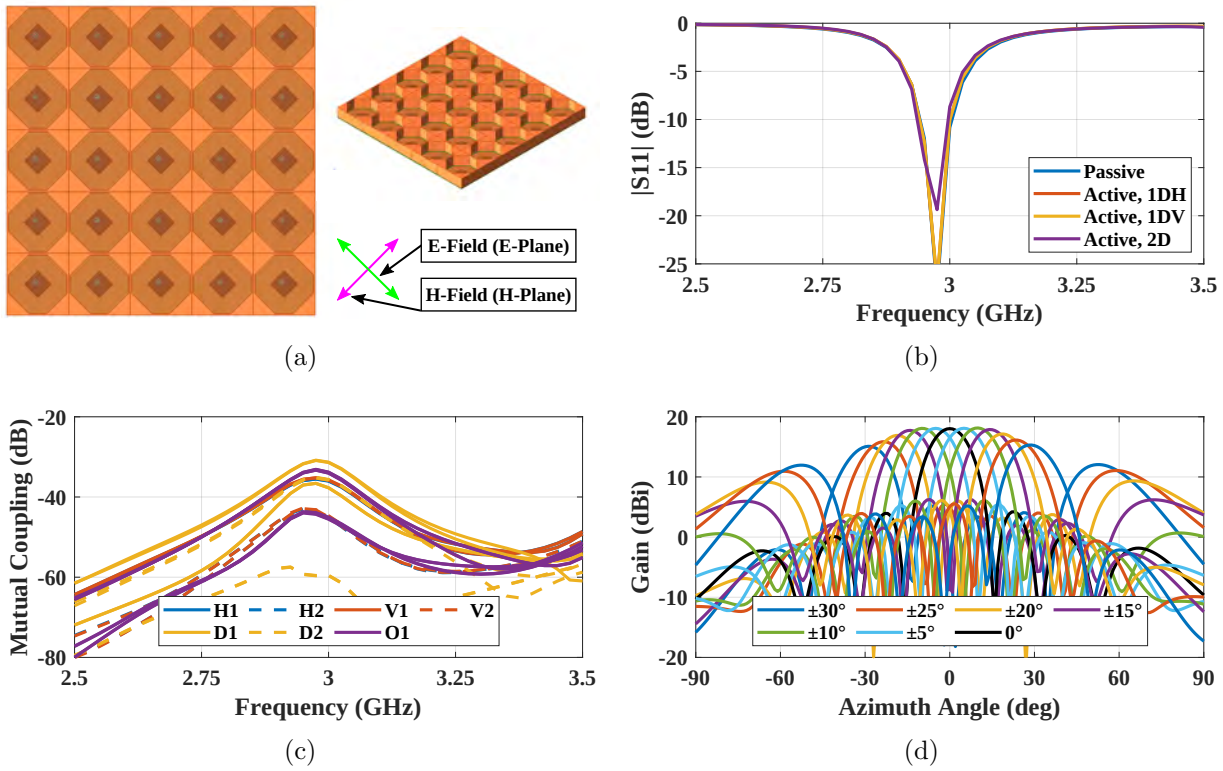


Figure 3.11: Reduced-coupling 25-element patch array: (a) top and isometric model views with field directions indicated; (b) simulated S11 magnitude for passive and active (1D horizontal, 1D vertical and 2D) configurations; (c) simulated mutual coupling to center element for the locations referenced in Fig. 3.4; and (d) simulated azimuth gain patterns for different scan angles.

3.4.2 Reduced-Coupling Design

Based on intuition, and backed by the findings presented in Fig. 3.8, it is clear that increasing the distance between array elements is an effective method of reducing their coupling. With this in mind, three mutual-coupling-reduction techniques were incorporated into the modified array design shown in Fig. 3.11a, with top and isometric model views depicted. The first change was the 45-degree rotation of the square patches, such that the E- and H-fields are shifted 45-degrees relative to the horizontal and vertical array axes, as indicated in the figure. While this has the effect of reducing the coupling horizontally and vertically, it unfortunately increases the coupling on the diagonal axes since those are now in line with the E- and H-planes, but does so with additional distance between diagonal elements. The second modification is increasing the unit cell

and element spacing to 3/4-λ at 3 GHz, which increases the overall array dimension to slightly less than 15 inches (14760 mils exactly). This technique introduces additional physical separation between the elements, but comes at the cost of degrading the array radiation pattern. The final array alteration is the inclusion of metallic walls between the elements that were added based on the results presented in the previous section.

Similar to the baseline, the simulated S11 magnitude of the center element for the passive and three active array configurations is plotted in Fig. 3.11b, and again indicates that the elements are well-matched to 50 Ω for each case. The more noticeable changes are seen in the mutual coupling and gain results presented in Figs. 3.11c and 3.11d, respectively.

For the former, several of the element locations on the array have similar coupling levels, which causes the traces to overlap on the plot. Due to the 45-degree rotation of the patches, the strongest coupling direction is now on the diagonal axis (still on the H-plane), as opposed to the horizontal axis for the baseline array. This coupling level has a maximum of -30.8 dB for the adjacent diagonal elements, which is slightly less than the same element on the baseline array that exhibited -29.2 dB of coupling. The most significant reductions are produced on the adjacent horizontal (H1 changing from -20.4 to -35.5 dB) and vertical planes (V1 changing from -24.1 to -35.2 dB), as well as elements located further away from the center.

Due to the 3/4-λ-element spacing that provides some of the mutual coupling reduction, grating lobes are introduced into the array gain pattern, as seen in Fig. 3.11d. These are similar to the ones discussed in Fig. 2.1 when the spacing is greater than 1/2-λ, and are seen to be larger as the scan angle is increased. While this plot illustrates the scanning performance out to ± 30 degrees for straightforward comparison to Fig. 3.10d, the modified array can be utilized with -13-dBc-sidelobe levels similar to the baseline when the scanning is restricted to ± 15 degrees. Additionally, the metallic walls are found to not only reduce the mutual coupling, but also enhance the array gain with 18.0 dBi simulated at broadside.

The maximum mutual coupling values for each path (relative to the center element) as well as the array gain are summarized in Table 3.2. After the baseline array in the first row, this table also

Table 3.2: Summary of Simulated Reduced-Coupling Array Design

Design Configuration	**Maximum Mutual Coupling (dB)**							**Gain**
	H1	**H2**	**V1**	**V2**	**D1**	**D2**	**O1**	**(dBi)**
Straight Patches, 1/2-λ Spacing	−20.4	−27.3	−24.1	−27.7	−29.2	−35.1	−29.4	16.5
Rotated Patches, 1/2-λ Spacing	−24.0	−32.0	−24.1	−32.0	−24.4	−29.6	−27.3	16.3
Straight Patches, 3/4-λ Spacing	−28.2	−38.0	−24.1	−28.2	−32.9	−39.9	−32.1	17.9
Rotated Patches, 3/4-λ Spacing	−28.7	−34.9	−28.8	−34.8	−28.3	−32.4	−32.2	17.9
Rotated Patches, 3/4-λ Spacing, 1-in Square Walls	−32.8	−35.2	−32.8	−35.2	−28.6	−33.2	−33.5	18.2
Rotated Patches, 3/4-λ Spacing, 0-in Chamfered Walls	−29.2	−35.5	−29.1	−35.5	−28.6	−32.7	−32.3	18.0
Rotated Patches, 3/4-λ Spacing, 1-in Chamfered Walls	−35.5	−43.0	−35.2	−42.7	−30.8	−35.1	−33.1	18.0

includes the performance of several other intermediate design configurations as listed in the first column, where detailed results along with the model images are presented in Appendix A. Overall, the mutual coupling decreased and the array gain increased as the design evolved and incorporated additional mutual coupling reduction techniques, where the last entry in the list represents the design illustrated in Fig. 3.11. A prototype of this reduced-coupling array design was fabricated and results are included in the system-level discussion presented in Chapter 6.

3.5 System Analysis

After discussing the mutual coupling performance of the 25-element array with both baseline and reduced-coupling configurations, the system-level and RF/analog front-end requirements can be analyzed. As depicted in Fig. 3.1, receivers within both aperture- and element-level IBFD arrays are tasked with linearly processing coherently-combined SI and XI signals so that digital cancellation

Receiver Cascade Analysis											
Parameter / Stage Name		**LPF1**	**HPF1**	**Amp1**	**DSA**	**Amp2**	**LPF2**	**HPF2**	**Atten**	**Balun**	**ADC**
Gain, nom (dB)		-1.2	-1.1	20.0	-2.0	20.0	-1.2	-1.1	-2.5	-0.8	0.0
NF, nom (dB)		1.2	1.1	0.7	2.0	1.3	1.2	1.1	2.5	0.8	32.0
Signal Level (dBm)	-20.0	-21.2	-22.3	-2.3	-4.3	15.7	14.4	13.3	10.8	10.0	10.0
Cum Gain, nom (dB)		-1.2	-2.3	17.7	15.7	35.7	34.4	33.3	30.8	30.0	30.0
Cum NF, nom (dB)		1.2	2.3	3.0	3.0	3.0	3.0	3.0	3.0	3.0	5.5
Cum Noise Floor (dBm/Hz)		-174.0	-174.0	-153.3	-155.3	-135.3	-136.5	-137.6	-140.1	-140.9	-138.4

Figure 3.12: Receiver cascade analysis, highlighting the cummulative gain and noise figure with an ADC saturation of 10 dBm corresponding to a receiver saturation of −20 dBm at the input.

can be performed after the ADCs. While this system diagram captures the LNA and ADC, many of the other receiver components are excluded for simplicity, as aforementioned.

Fig. 3.12 represents the cascade analysis for a typical receiver using an expanded component list for a direct-RF-sampled architecture with stages that include two low-pass filter (LPF) and high-pass filter (HPF) combinations that provide frequency-band selection; two amplifiers (Amps); a digital step attenuator (DSA); a fixed attenuator (Atten); a single-ended to differential balun; and an ADC. For this analysis, the ADC has a full-scale voltage of 2 volts peak-to-peak, which corresponds to 10 dBm in a 50-Ω system. This figure represents a spreadsheet that contains cascaded equations based on the individual component gain and noise figure parameters (blue text) listed in the upper rows, where nominal values have been utilized. The lower rows capture the cumulative gain, noise figure and noise floor performance. The final component listed is the ADC and the last column represents the complete receiver performance, as calculated by this cascade analysis.

Based on the parameters utilized, this example receiver has a total cumulative gain of 30 dB and a nominal noise figure of 5.5 dB. This amount of gain is fairly standard to reduce the impact of the ADC quantization noise, and translates to an input signal level of −20 dBm (orange cell) being amplified up to the full-scale ADC level of 10 dBm (yellow cell). While the linearity metrics of these components can also be considered, this gain-focused analysis implies that the total SI should be limited to less than −20 dBm in order to avoid ADC saturation and maintain the full sensitivity of the receivers within the array. Based on this level, the cancellation requirements for both aperture-

and element-level IBFD arrays can be determined, as discussed in the following sections.

3.5.1 Aperture-Level IBFD Array Requirements

For each transmitter within an aperture-level IBFD array, the front-end is required to attenuate the DP SI and feed it into a transmit-observation receiver within the same element so that it can be digitized to aid subsequent cancellation. Based on the analysis conducted in the previous section, the receiver saturation level can be assumed to be $-20\,\text{dBm}$ at the input. From Fig. 3.1, the minimum required attenuation in dB for the transmit observation path can be defined as

$$\text{TxObs}_{\text{Atten}} = P_{Tx} - P_{Rx_{ISAT}}, \tag{3.1}$$

where P_{Tx} is the element transmit power in dBm and $P_{Rx_{ISAT}}$ is the input receiver saturation power in dBm. Since $P_{Rx_{ISAT}}$ is defined based on the ADC full-scale level per the cascade analysis, this attenuation does not need to occur solely in the front-end, and instead, can the distributed throughout the transmit-observation receiver as long as each individual component is operated within its linear range. It should be noted that while the transmit-observation receivers located behind each transmit element are operating in a full-duplex mode, they do so with a significantly degraded sensitivity compared to those analyzed in Fig. 3.12.

The primary source of interference within aperture-level IBFD arrays comes from XI between the transmit and receive subarrays. The received XI power is a function of the transmit power and is dictated by the mutual coupling of the array, such that

$$P_{Rx_{AL\text{–}XI\text{–}1D}} = P_{Tx} \cdot G_{Tx} \cdot (h_{1,3\text{–}3,3} + h_{2,3\text{–}3,3}) \cdot G_{Rx}, \tag{3.2}$$

captures the power received (in linear units) at the input of the center element for a 1D horizontal array with the coupling depicted in Fig. 3.3a. G_{Tx} and G_{Rx} represent the gains for the transmit and receive paths within the front-end, respectively. The transmit-to-receive channel responses are represented by $h_{1,3\text{–}3,3}$ and $h_{2,3\text{–}3,3}$ for the H1 and H2 transmit elements, respectively, as defined by the designators depicted in Fig. 3.2. From this, the required minimum XI cancellation can be

defined as

$$\text{Canc}_{AL\text{–}XI\text{–}1D} = P_{Rx_{AL\text{–}XI\text{–}1D}} - P_{Rx_{ISAT}}, \tag{3.3}$$

which maintains the XI at the receiver input below the saturation level.

While Eq. 3.3 captures the receive power for a 1D array with only two transmit elements, this can be extended to 2D scenarios, including the one highlighted in Fig. 3.3, such that

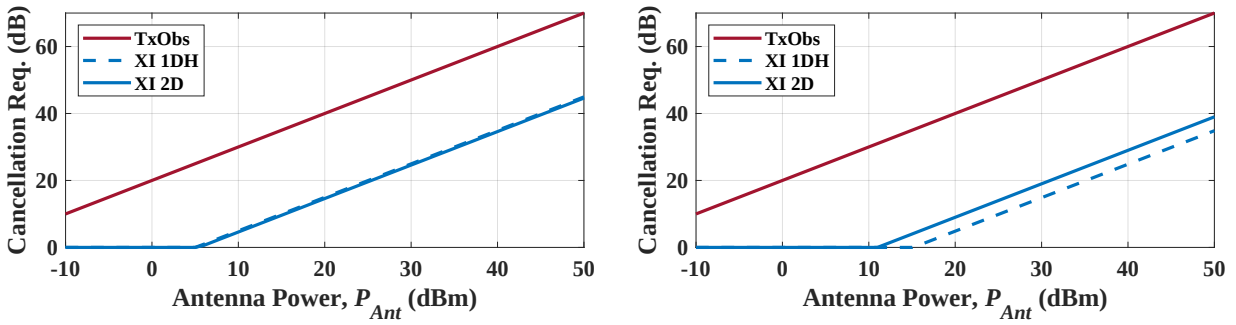
$$\begin{aligned} P_{Rx_{AL\text{–}XI\text{–}2D}} = P_{Tx} \cdot G_{Tx} \cdot (&h_{1,1\text{–}3,3} + h_{1,2\text{–}3,3} + h_{1,3\text{–}3,3} + h_{1,4\text{–}3,3} + h_{1,5\text{–}3,3} \\ &+ h_{2,1\text{–}3,3} + h_{2,2\text{–}3,3} + h_{2,3\text{–}3,3} + h_{2,4\text{–}3,3} + h_{2,5\text{–}3,3}) \cdot G_{Rx}, \end{aligned} \tag{3.4}$$

where $h_{1,1\text{–}3,3}$; $h_{1,2\text{–}3,3}$; $h_{1,3\text{–}3,3}$; $h_{1,4\text{–}3,3}$; $h_{1,5\text{–}3,3}$; $h_{2,1\text{–}3,3}$; $h_{2,2\text{–}3,3}$; $h_{2,3\text{–}3,3}$; $h_{2,4\text{–}3,3}$; and $h_{2,5\text{–}3,3}$ capture the 10 unique coupling paths between the transmit elements and the center-receive element (denoted X). Similar to Eq. 3.3, the cancellation requirement for a 2D aperture-level IBFD array can be identified as

$$\text{Canc}_{AL\text{–}XI\text{–}2D} = P_{Rx_{AL\text{–}XI\text{–}2D}} - P_{Rx_{ISAT}}, \tag{3.5}$$

where the cancellation is focused on the center-receive element since the coupling is the strongest and the requirement is relaxed further from the boundary. It should be noted that this cancellation is required before the receiver input, which precludes the use of post-digitization techniques (i.e. receive beamforming and digital cancellation), and instead necessitates the use of transmit beamforming.

Based on the arrays discussed in the previous section, the aperture-level IBFD cancellation requirements are determined for baseline- and reduced-coupling arrays in Figs. 3.13a and 3.13b, respectively. The antenna power is simply defined as $P_{Ant} = P_{Tx} + G_{Tx}$. As given by Eq. 3.1, the transmit-observation cancellation is independent of G_{Tx}, and is the same for each coupling scenario because it also does not depend on the XI. For example, the plots indicate that the minimum transmit-observation attenuation is 40 dB for a transmit power of 20 dBm. Since aperture-level IBFD array front-ends are typically passive, G_{Tx} and G_{Rx} were assumed to be -1 dB for this analysis.



(a) (b)

Figure 3.13: Aperture-level array cancellation requirements for the transmit observation (TxObs) path as well as the crosstalk interference for the 1D horizontal (XI 1DH) and 2D (XI 2D) configurations with mutual coupling from the (a) baseline and (b) reduced mutual coupling arrays.

The XI cancellation requirements, on the other hand, are strongly dependent on the number of transmit elements as well as their mutual coupling to the receive element under consideration. For the baseline-coupling case depicted in Fig. 3.13a, the 1D and 2D scenarios are seen to require similar amounts of cancellation, namely 15.0 and 14.6 dB at 20 dBm output power, respectively. This indicates that the horizontal elements are strong contributors to the composite coupling path and that some destructive interference must be occurring for the 2D configuration to require less cancellation than the 1D case.

As expected, the cancellation requirements are relaxed for the reduced-coupling array, as seen in Fig. 3.13b. The 1D and 2D requirements can be more clearly differentiated to be 4.9 and 9.0 dB at 20 dBm output power, respectively. While this difference is not large, it should be noted that these metrics are for an aperture-level array with only 10 transmit elements (as defined in Fig. 3.3), and more significant cancellation may be necessary for different array configurations. Both plots in Fig. 3.13 indicate that the requirements linearly increase with higher transmit/antenna power, but below a certain level, no cancellation is necessary.

3.5.2 Element-Level IBFD Array Requirements

The requirements for element-level IBFD arrays differ from their aperture-level counterparts since each receiver must maintain full sensitivity while transmitting with the same element. From Fig. 3.1, the DP, AR and coherent combination of XI must be considered. Similar to the aperture-level transmit-observation cancellation, the minimum DP-SI suppression for the front-end is defined as

$$\mathrm{Canc}_{\mathrm{DP}} = P_{Tx} - P_{Rx_{ISAT}}, \tag{3.6}$$

since the DP is dependent on only the front-end. Conversely, the AR-SI signal travels through both the transmit and receive paths of the front-end, and is thus affected by their gains according to

$$P_{Rx\text{–}AR} = P_{Tx} \cdot G_{Tx} \cdot h_{3,3\text{–}3,3} \cdot G_{Rx}, \tag{3.7}$$

where $h_{3,3\text{–}3,3}$ represents the antenna reflection coefficient for the center element (location 3,3) under consideration. Similar to before, the cancellation requirement is simply this power level minus the input saturation power of the receiver.

For the XI, three different array configurations can be considered, namely 1D horizontal (1DH), 1D vertical (1DV) and 2D that reference the coupling paths illustrated in Fig. 3.4. The XI power at the input to the center-element receiver for the 1DH and 1DV cases can be computed using

$$P_{Rx_{EL}\text{–}XI\text{–}1DH} = P_{Tx} \cdot G_{Tx} \cdot (h_{1,3\text{–}3,3} + h_{2,3\text{–}3,3} + h_{4,3\text{–}3,3} + h_{5,3\text{–}3,3}) \cdot G_{Rx}, \tag{3.8}$$

and

$$P_{Rx_{EL}\text{–}XI\text{–}1DV} = P_{Tx} \cdot G_{Tx} \cdot (h_{3,1\text{–}3,3} + h_{3,2\text{–}3,3} + h_{3,4\text{–}3,3} + h_{3,5\text{–}3,3}) \cdot G_{Rx}, \tag{3.9}$$

respectively. Where the horizontal configuration contains XI coupling from element locations 1,3; 2,3; 4,3; and 5,3 to element 3,3. The vertical array is similarly constructed with elements 3,1; 3,2; 3,4; and 3,5 generating XI coupling to the center, where these numbered locations are depicted in Fig. 3.2a. Lastly, when all elements are active, as in the 2D array scenario, the received power can

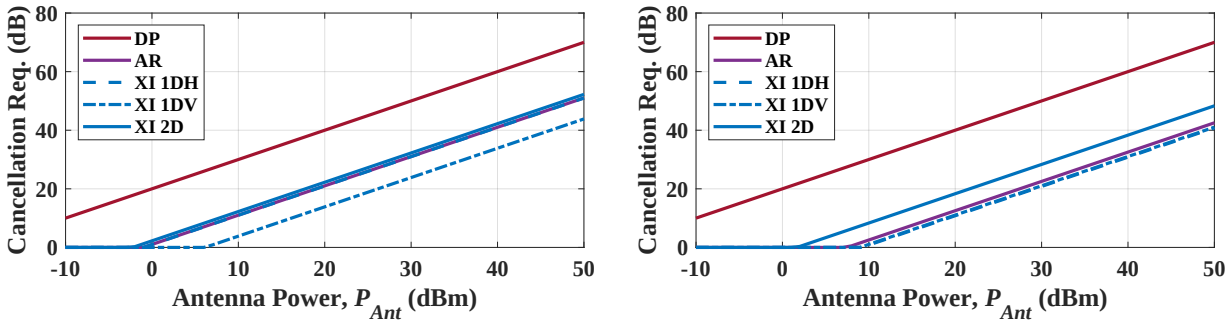


Figure 3.14: Element-level array cancellation requirements for low-gain front-ends, highlighting the direct path (DP), antenna reflection (AR), and crosstalk interference for 1D horizontal (XI 1DH), 1D vertical (XI 1DV) and 2D (XI 2D) configurations with mutual coupling from the (a) baseline and (b) reduced mutual coupling arrays.

be determined using

$$P_{Rx_{EL-XI-2D}} = P_{Tx} \cdot G_{Tx} \cdot \left(\sum_{j=1}^{5} \sum_{\substack{k=1 \\ (j,k)\neq(3,3)}}^{5} h_{j,k} \right) \cdot G_{Rx}, \tag{3.10}$$

where the coupling path between every element in the array to the center element is captured. While this clearly represents the most extreme coupling configuration for the 25-element array being considered, it provides a reasonable estimate for larger arrays since contributions from further elements are reduced. Again, the XI cancellation requirements are simply calculated as these power levels minus the receiver saturation at the input.

Based on these equations, the cancellation requirements can be examined for different transmit power levels, similar to the aperture-level ones already discussed. One significant difference between the front-ends of these array types, however, is the fact that those for element-level arrays often incorporate gain on both transmit and receive, which amplifies not only the desired signals but also the SI and XI. Figs. 3.14a and 3.14b display the cancellation requirements for low-gain front-ends (G_{Tx} and G_{Rx} set to -1 dB) for arrays with baseline and reduced coupling, respectively. When considering a transmit output power of 20 dBm for each element, the DP-SI cancellation requirement is found to be 40 dB, which is slightly different from the transmit-observation num-

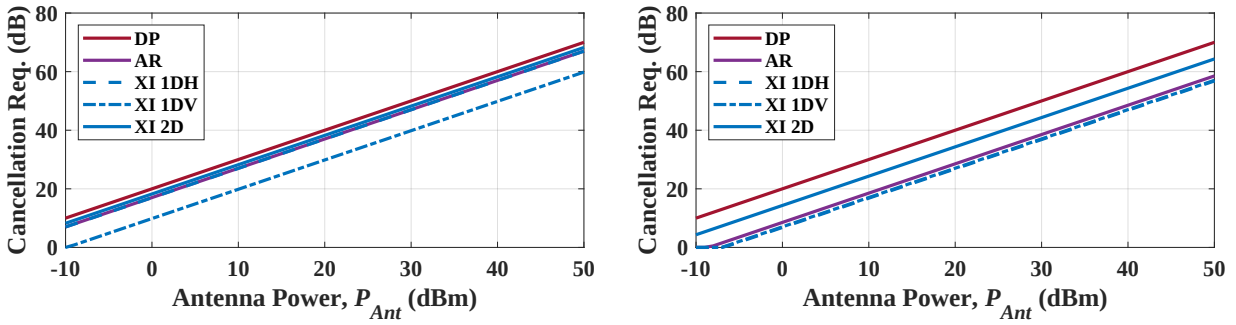


Figure 3.15: Element-level array cancellation requirements for high-gain front-ends, highlighting the direct path (DP), antenna reflection (AR), and crosstalk interference for 1D horizontal (XI 1DH), 1D vertical (XI 1DV) and 2D (XI 2D) configurations with mutual coupling from the (a) baseline and (b) reduced mutual coupling arrays.

ber in aperture-level designs since this cancellation must occur in the front-end in order to avoid saturation.

With the arrays being different between the two figures, the AR and XI values are not the same. For the baseline array, the cancellation requirements are 21.0, 21.0, 13.8, and 22.2 dB for the AR, XI 1DH, XI 1DV, and XI 2D at 20 dBm output power, respectively. These values compare to 12.5, 10.8, 11.0, and 18.3 dB for the same power level using the reduced-coupling array. While the AR requirement difference is due to the change in the impedance match, the XI cancellation requirements are lower for the reduced-coupling design, as expected. It should be noted that the cancellation requirement is relaxed for both 1D configurations versus the full 2D operation. Also, since the front-end gains were the same for the aperture- and element-level scenarios considered in Figs. 3.13 and 3.14, the cancellation requirements between the two IBFD array types can be compared, where the numbers are seen to be lower for aperture-level designs.

Figs. 3.15a and 3.15b illustrate the element-level IBFD array cancellation requirements for front-ends with 15 dB gains in the transmit and receive paths. While this does not change the DP-SI metrics, the AR and XI for all cases are seen to increase. Again looking at the 20 dBm output power level, the cancellation requirements with the baseline coupling are 37.0, 37.0, 29.8,

and 38.2 dB for the AR, XI 1DH, XI 1DV, and XI 2D, respectively. For the reduced-coupling array, these values are 28.5, 26.8, 27.0, and 34.3 dB, which are all relaxed compared to the baseline. These reduced cancellation requirements could lead to simplifications in the front-end cancellation circuitry or allow the output power to be increased for the same amount of cancellation. Overall, the values for high-gain front-ends are clearly increased over the low-gain versions, which makes the front-end design more challenging.

3.6 Chapter Conclusion

This chapter presents a generic system architecture, on which the key aspects of both aperture- and element-level IBFD arrays are considered. Both array types must address SI that arises from DP and/or AR within some or all of the elements as well as XI from neighboring elements within the array in order to avoid receiver saturation. This XI is a function of the mutual coupling between elements, where an overview of the different coupling paths was discussed for each array type, including full 2D and 1D subsets. Several different methods of reducing the mutual coupling are analyzed using a 7-element linear array, which aided the design of a 25-element 2D array with a focus on reduced-coupling between elements. This helps form the basis for mutual coupling on which an IBFD system could be analyzed, and the cancellation requirements determined for the front-ends of both aperture- and element-level IBFD arrays. These are necessary for the design of such front-ends, as will be discussed in the following chapters. Parts of the material presented in this chapter are reported in [68].

Chapter 4

IBFD Front-End One-Tap Active Circulator

4.1 Introduction

Nine different types of dish-antenna-based radar systems are currently deployed across the United States to create an air traffic control and weather monitoring network [22]. As these systems near their end of life, a common design built upon the electronic-scanning capability of phased arrays is being considered to replace them [50]. This multifunction phased array radar (MPAR) concept provides the ability to detect and track aircraft while simultaneously monitoring the weather [49, 140]. Compared to legacy systems, this new paradigm enhances air safety by detecting dangerous microbursts, bird hazards and non-cooperative drone aircraft, in addition to providing advanced weather prediction.

Despite these advantages, existing developments have focused on traditional pulsed-radar schemes that utilize a time-division duplex (TDD) approach to switch between transmit and receive modes, as illustrated in the top left of Fig. 4.1. This method disables the receivers when transmitting and consequentially creates a "blind range" within which the radar cannot detect targets [135]. This minimum detectable range is proportional to the transmit pulse width, such that longer pulses translate to longer blind ranges, which can be greater than 10 km in some cases and is particularly problematic when the radar is located at an airport [18]. A possible solution is the use of in-band full-duplex (IBFD) technology that allows both transmit and receive functions to be active simultaneously [75]. As seen in the top right of Fig. 4.1, this allows the radar to keep the receiver enabled during transmit pulses and continually detect returns from nearby objects, eliminating

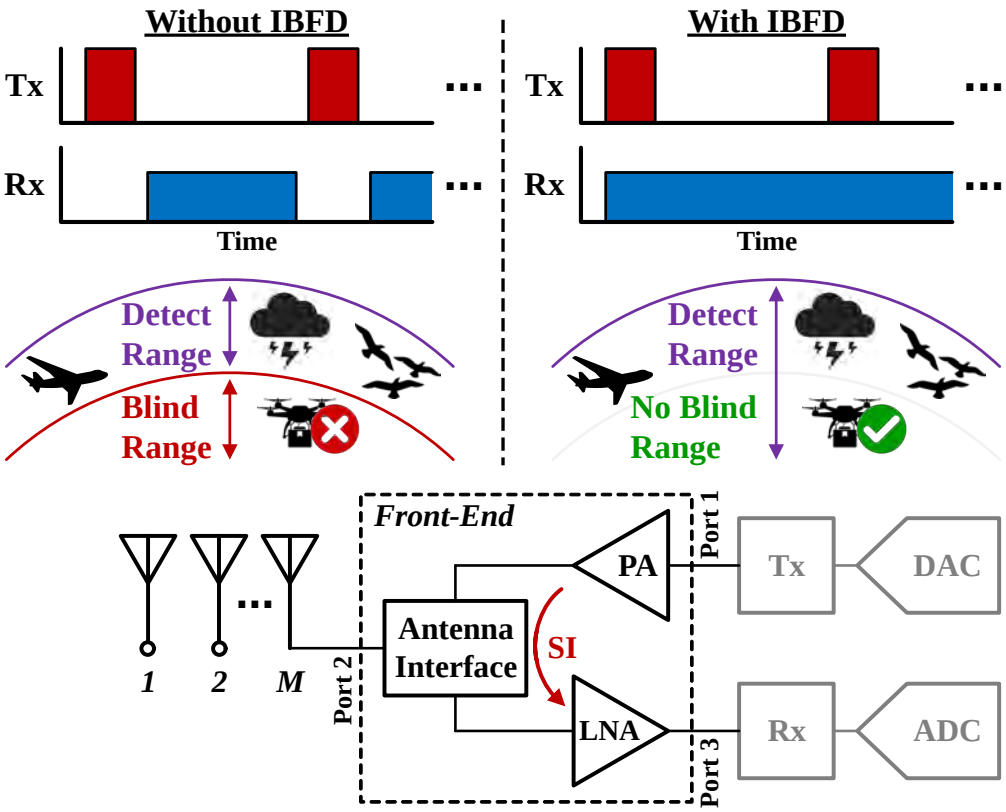


Figure 4.1: Sketch of a multifunction phased array radar that can eliminate its blind range with IBFD technology and front-end self-interference (SI) suppression.

the blind range issue [78, 96]. The multifunction radar scenario depicted in Fig. 4.1 additionally highlights a single channel within the array and illustrates how the transmitter and receiver share an antenna using an interface device within the front-end.

While this interface is simply a switch for traditional TDD-based architectures, IBFD designs require the simultaneous connection of the antenna to both transmit and receive as well as careful attention to the resulting self-interference (SI) at this connection point [63]. Predominate compact topologies include electrical balanced duplexers and integrated circulators, where a deeper comparative analysis is presented in [15]. While the former is a reciprocal-passive device that typically exhibits significant loss (5 to 6 dB) for both transmit and receive paths, the latter is a nonreciprocal-active component that can include signal gain, and is also referred to as an active circulator [109]. Active circulators utilize the unidirectional nature of transistors to create nonreciprocal devices

that avoid ferrites, which results in more compact designs that can be integrated into arrays [107]. While these devices are not passive and their port assignments are often not interchangeable (like traditional circulators), they offer unique opportunities to include isolation-enhancement techniques and gain.

The design of active circulators centers on maximizing the device's transmit-to-receive isolation, along with other key metrics, including operational bandwidth, impedance matching, transmit and receive path losses, transmit power handling, and receive noise figure. Active circulators can be grouped into two main categories based on their underlying technology materials: those created on silicon and those that use III-V compound semiconductors [44]. Generally, silicon-based circuits have lower power handling and linearity due to the lower bandgap of silicon (1.12 eV) compared to indium phosphide (InP) (1.34 eV), gallium arsenide (GaAs) (1.4 eV), and gallium nitride (GaN) (3.39 eV). Since we are interested in high power handling, this chapter will focus on active circulators that utilize III-V compound semiconductors [27].

Initial integrated active circulators combined a small number of GaAs transistors to create simple out-of-phase dividers and in-phase combiners that operated over wide bandwidths, 0.1 to 10 GHz [41] and 0.1 to 15 GHz [146], but with limited isolation. Similar methods were leveraged for a design that operated from 37 to 43 GHz using coplanar waveguide (CPW) ports [82], as well as translated into an InP process with transmission-line-based phase shifters for 35 to 40 GHz coverage [10]. While all of these designs exhibited nontrivial transmit and receive losses, the same divider/combiner principle was shown to provide gain for both transmit and receive over the 3.8 to 4.2 GHz band, along with an isolation of 22 dB [38].

An alternative architecture using three Lange couplers has been used to create GaAs designs at X-band, including a passive core of quadrature hybrids [19] and a closed-loop connection with gain-matched amplifiers [98]. Additionally, the high-power density of GaN has been investigated to combine common-gate and common-source transistors to create a lossy design from 27 to 29 GHz [150]. Commercial off-the-shelf (COTS) transistors have also been utilized to create active circulators with varying amounts of isolation, and while their size cannot compete with their

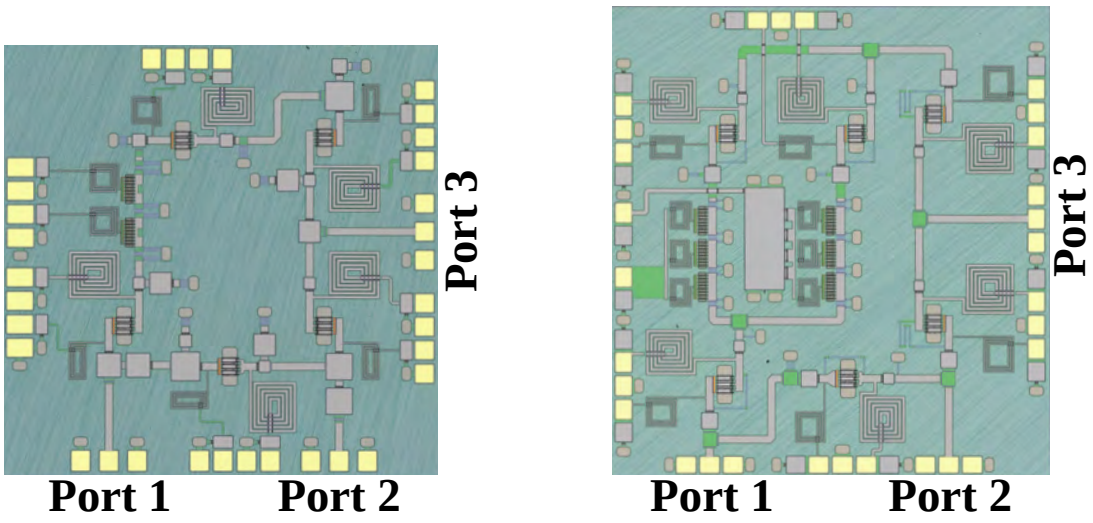


Figure 4.2: Active circulator GaN front-end MMICs with (a) one and (b) two integrated-tunable cancellers and matching port designators.

integrated counterparts, their transmit and receive path losses are often lower [104–106, 113, 123].

All of the aforementioned circulators provide a fixed transmit-to-receive isolation that is dependent on internal phase shifts, which are inherently frequency-selective and translate to isolation that varies across bandwidth. For a single design, tunable isolation enhancement was added to the circuit presented in [104] by varying the gate voltage of the transistor that controlled the phase shift, which resulted in an isolation of 40 dB over the 0.8 to 2.2 GHz tuning range [108]. In addition to that approach exhibiting insertion losses for the transmit and receive paths, the transmit power handling was limited to 8 dBm, inhibiting inclusion in modern phased arrays.

This and the following chapter both discuss two active circulators implemented as monolithic microwave integrated circuits (MMICs). They contain tunable cancellers to enhance transmit-to-receive isolation in addition to integrating a power amplifier (PA) and low-noise amplifier (LNA) for the purpose of creating a complete compact front-end that can enable IBFD arrays. Figures 4.2a and 4.2b depict photos of the two chips with one- and two-integrated canceller circuits, respectively, both of which were fabricated in the WIN Semiconductors NP12-01 0.12 μm GaN-on-SiC process. To the best of the authors' knowledge, these are the first GaN-based active circulators that exhibit

gain in the transmit and receive paths and include frequency-tunable isolation enhancement.

This work expands on the initial conference publication that introduced the active circulator design [71] by augmenting the previous simulation-only results with measurement comparisons and introducing a second design with enhanced tuning. Measurements of the active circulator inserted into a typical radar system are included in Chapter 5, along with demonstration of additional isolation using a chirp waveform and a digital cancellation filter, which highlight the functionality of the design for future IBFD phased arrays.

4.2 Architecture Overview

The block diagram of the active circulator is shown in Fig. 4.3, with port 1 for the transmitter, port 2 for the antenna, and port 3 for the receiver. The design consists of four amplifiers and a tunable canceller section. The node at port 1 acts as a power divider that splits the incoming transmit signal between the PA path (solid red arrow) and the tunable canceller path (dashed blue arrow). While both paths denote connections from ports 1 to 3, the former represents the internal SI path of the circulator and the latter embodies an approach to compensate for it. In order to better understand the design goal and relationship between these, impulse responses and corresponding transfer functions can be analyzed, beginning with

$$h_{SI}(t) = g_{SI}(t)\,\delta(t - \tau_{SI}) * h_{\phi_{SI}}(t), \tag{4.1}$$

where $g_{SI}(t)$ captures the gain from both amplifiers (the PA and LNA), such that $g_{SI} = g_{A1} \cdot g_{A2}$, for an input signal that additionally experiences a delay of τ_{SI} from ports 1 to 3 and is convolved with a composite phase shift response, $h_{\phi_{SI}}(t)$, where $\phi_{SI} = \phi_{A1} + \phi_{A2}$. The importance of these gain, delay and phase shift variables can also be visualized in the frequency domain, according to

$$H_{SI}(j\omega) = G_{SI}(j\omega)\, e^{-j\phi_{SI}}\, e^{-j\omega\tau_{SI}}, \tag{4.2}$$

where ϕ_{SI} denotes the phase shift in radians for $\omega \geq 0$.

The other connection between ports 1 and 3 contains the tunable canceller with N parallel

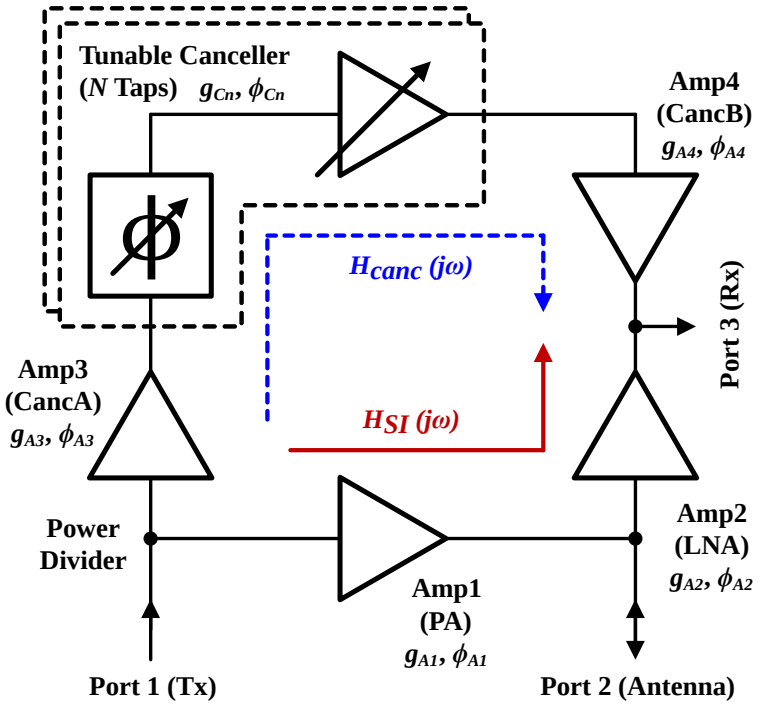


Figure 4.3: Block diagram of the active circulator with three ports, highlighting the two different paths ($H_{SI}(j\omega)$ and $H_{canc}(j\omega)$) between ports 1 and 3, four amplifiers, and a tunable canceller section with N taps to improve the transmit-receive isolation.

and independently tunable phase and gain sections, referred to as taps, and can be represented by

$$h_{canc}(t) = g_{C0}(t)\,\delta(t-\tau_{C0}) * h_{\phi_{C0}}(t) \cdot \left[\sum_{n=1}^{N} g_{Cn}(t)\,\delta(t-\tau_{Cn}) * h_{\phi_{Cn}}(t)\right], \tag{4.3}$$

where g_{C0}, τ_{C0} and $h_{\phi_{C0}}(t)$ capture the combined gain, delay and phase responses, respectively, of the two fixed amplifiers (CancA and CancB in Fig. 4.3), such that $g_{C0} = g_{A3} \cdot g_{A4}$ and $\phi_{C0} = \phi_{A3} + \phi_{A4}$. The second group of terms relate to the tunable canceller section, and illustrate how the N taps have different gain, delay and phase responses, and are combined through summation. This impulse response can be expressed in the frequency domain for sinusoidal (time-harmonic) carrier frequencies, such that

$$H_{canc}(j\omega) = G_{C0}(j\omega)\,e^{-j\phi_{C0}}\,e^{-j\omega\tau_{C0}} \cdot \left[\sum_{n=1}^{N} G_{Cn}(j\omega)\,e^{-j\phi_{Cn}}\,e^{-j\omega\tau_{Cn}}\right], \tag{4.4}$$

where the fixed and tunable components are both represented.

In order to generate the desired SI cancellation, the two paths between ports 1 and 3 should produce signals that arrive at port 3 with the same amplitudes and delays but are out-of-phase,

which results in

$$H_{canc}(j\omega) = -H_{SI}(j\omega), \tag{4.5}$$

such that, when these signals are combined, they destructively interfere and enhance the transmit-receive isolation of the active circulator. This requirement allows the derivation of two distinct design goals for the tunable canceller section. Assuming the delays between the two paths are matched, the gain and phase necessary for cancellation are

$$G_{Cn}(j\omega) = \frac{G_{A1}(j\omega) \cdot G_{A2}(j\omega)}{G_{A3}(j\omega) \cdot G_{A4}(j\omega)}, \tag{4.6}$$

and

$$\phi_{Cn}(j\omega) = \phi_{A1}(j\omega) + \phi_{A2}(j\omega) - \phi_{A3}(j\omega) - \phi_{A4}(j\omega) + \pi, \tag{4.7}$$

respectively. These equations illustrate that when the gain of the four fixed amplifiers (PA, LNA, CancA, and CancB) have similar levels, the canceller section requires near unity, or 0 dB, of gain. Similarly, when the amplifiers' phases responses are comparable, the canceller section should ideally generate a π, or 180°, phase shift to produce the intended SI suppression. For the first proof-of-principle designs presented in this chapter, all four amplifiers are equal single-stage topologies, and the canceller is designed to have roughly 0 dB total gain and introduce a nominal phase shift of 180° at the desired center frequency of 3 GHz. The tunable aspects of the canceller allow it to match the amplitude and 180° phase shift at different frequencies, which extends the operational range of the device. Details are discussed in the following sections.

4.3 Active Circulator Design

The first active circulator, shown in Fig. 4.2a, contains one tunable canceller tap ($N = 1$) with one adjustable amplifier and phase shifter section. The complete chip layout is depicted in Fig. 4.4, where the three ports match those illustrated in Fig. 4.3. The layout indicates the various metal layers, ground vias connected to the backside of the chip, RF and dc bond pads around the edges, different capacitors, and tantalum nitride (TaN) resistors. The design details of these circuit elements are discussed next.

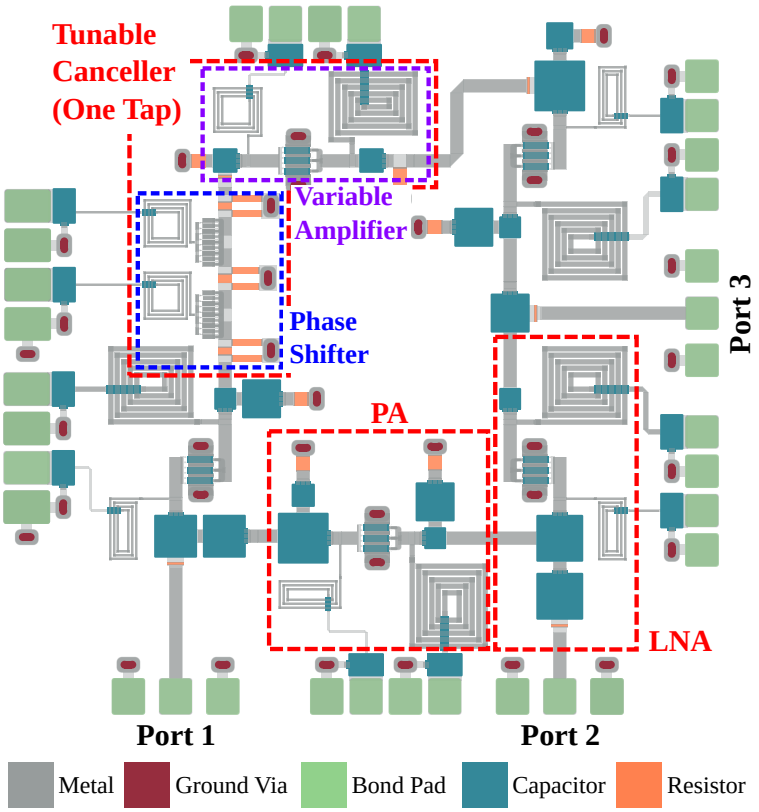


Figure 4.4: Active circulator with one-tap tunable canceller layout with labeled ports matching Fig. 4.3, highlighting the PA and LNA in the bottom right, and the amplifier and phase shifter within the canceller of the upper left.

4.3.1 Amplifier Design

The single-ended amplifier circuit schematic is shown in Fig. 4.5a, and uses a $6 \times 100\,\mu$m device. Capacitors (C_g and C_d), inductors (L_g and L_d) and microstrip transmission lines are used to match the transistor to $50\,\Omega$ as well as nominally supply the gate and drain bias voltages, V_g and V_d, with -1.6 and $+28\,$V, respectively. The input and output power dividers are represented between the input/output ports and their respective dc-blocking capacitors by impedances Z_{DIV}, that are AC-coupled through the capacitors. These impedances represent the connection of another amplifier at these nodes or a simple $50\,\Omega$ load when no division is needed, and are taken into account in the matching design. The schematic diagram not only highlights the amplifier architecture, but also illustrates the nominal component values.

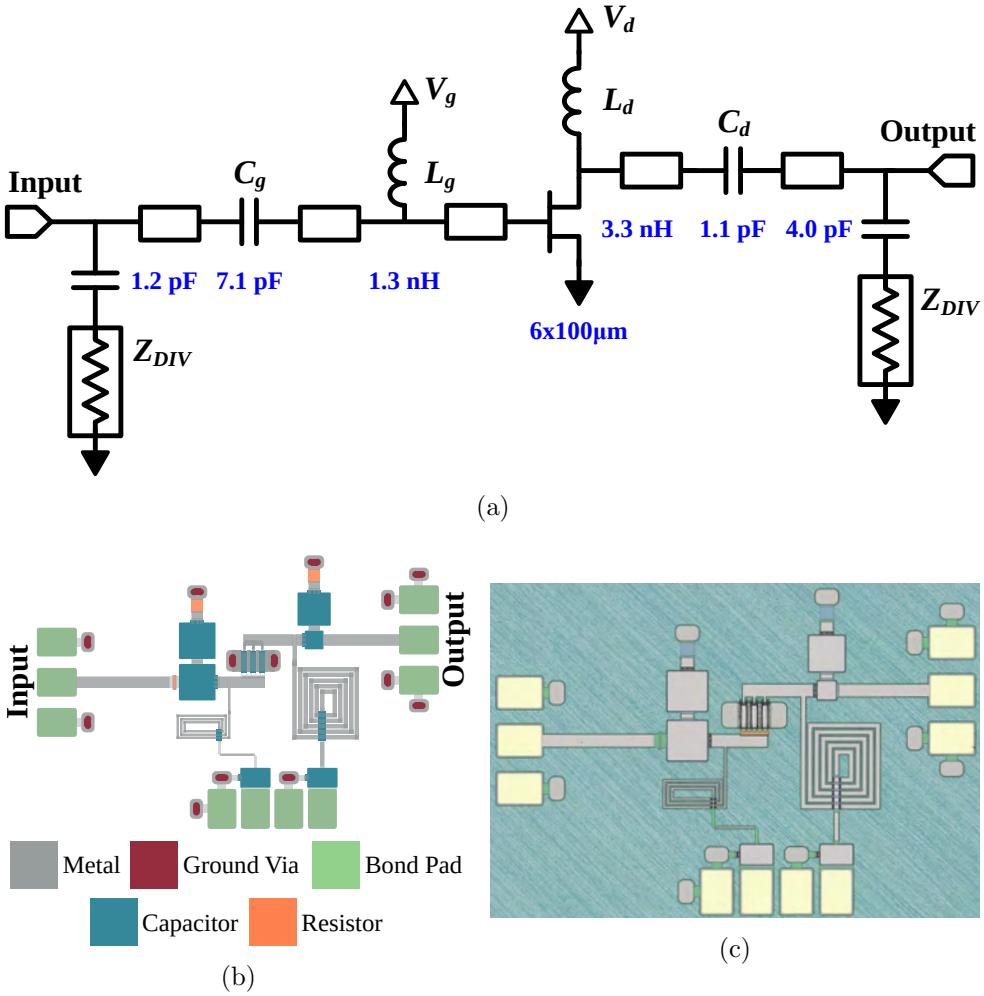


Figure 4.5: Amplifier circuit with a single-stage transistor, matching networks and power dividers at the input and output: (a) schematic, (b) layout and (c) photo with an active area of 0.83×0.65 mm.

The layout of the amplifier test circuit can be seen in Fig. 4.5b along with the associated die photo in Fig. 4.5c. These images illustrate the use of ground-signal-ground (GSG) bond pads to connect to the input and output as well as GSGS pads with decoupling capacitors that were used to supply the dc gate and drain bias voltages. The chip metal layers, grounding vias, capacitors, and TaN resistors are also illustrated.

The |S21| and ∠S21 responses of the amplifier are plotted over the frequency band of interest in Fig. 4.6a on the left and right axis, respectively. The plot compares the measured data (solid) with the simulated results (dashed) for a nominal gate bias of −1.6 V. At 3 GHz, the gain is found

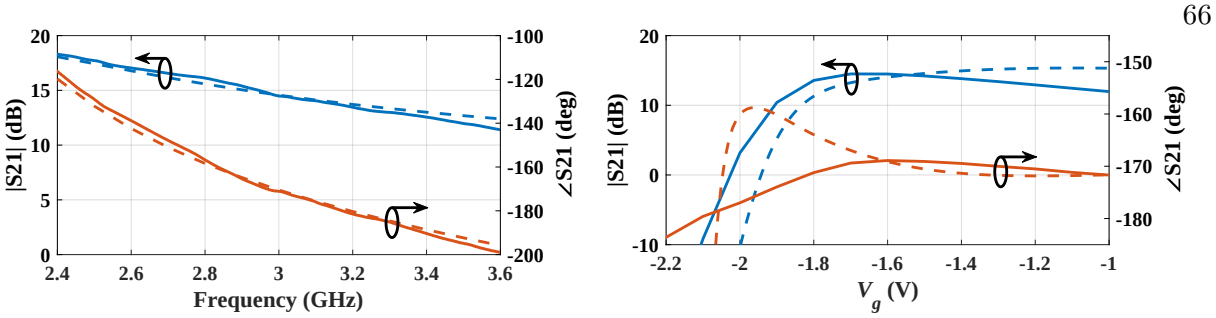


Figure 4.6: Amplifier circuit gain and phase comparison of measurements (solid) with simulated results (dashed) over (a) frequency and (b) gate voltage.

to be 14.5 dB with a phase shift of $-170°$, which is close to the $-180°$ needed for cancellation. While this image shows that the gain changes by less than 2 dB from 2.8 to 3.2 GHz, the phase is seen to change by more than 20° over that frequency range. The measurements match the expected results well.

Fig. 4.6b illustrates the amplifier performance as a function of the tunable gate voltage for a frequency of 3.0 GHz. The gain can be tuned by more than 25 dB, and is seen to deviate slightly from the simulation due to the addition of the dc probe parasitic inductance. The phase unintentionally changes by 10 to 15°, which is less than expected. This phase change combined with the frequency-dependent one motivates the need for a circuit that can dynamically compensate for these phase differences, as discussed next.

4.3.2 Phase Shifter Design

For the one-tap canceller design, the variable phase shifter is constructed using two reverse-biased diodes and three π-network attenuators, as seen in Fig. 4.7a. The phase change is accomplished by tuning the two control voltages, V_{ctrl}, of the diodes that are implemented with $8 \times 50\,\mu$m devices, and tuned using a bias voltage that ranges from -7 to -1 V. The π attenuators provide a total of 12.5 dB of attenuation using the 4, 4.5, and 4 dB sections illustrated, and effectively offset the gain of the following amplifier, such that the nominal gain of the combined phase shifter and

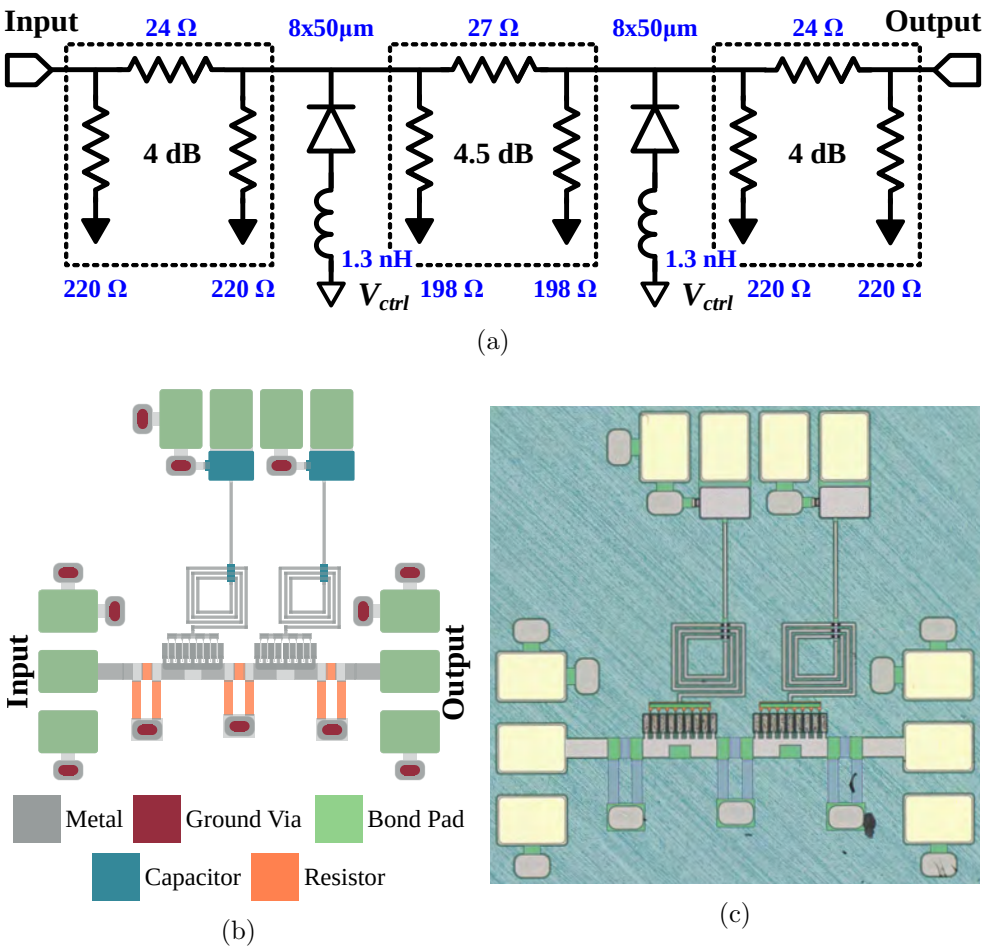


Figure 4.7: Phase shifter circuit with reverse-biased diodes and π-attenuator networks: (a) schematic, (b) layout and (c) photo with an active area of 0.63×0.52 mm.

amplifier is 0 dB, as previously mentioned. In addition to illustrating the phase shifter design, the schematic diagram also depicts the nominal component values.

Figs. 4.7b and 4.7c illustrate the phase shifter layout and matching die photo, respectively. Similar to the amplifier circuit, GSG pads are used for the input and output, and GSGS pads with decoupling capacitors are used for the bias control voltages. It should be noted that even though two distinct control lines are routed to the pads, they are tied together off-chip to form a single control voltage. Additionally, the chip metal layers, capacitors, ground vias, and TaN resistors are depicted.

The magnitude and phase responses of S21 are plotted over frequency on the left and right

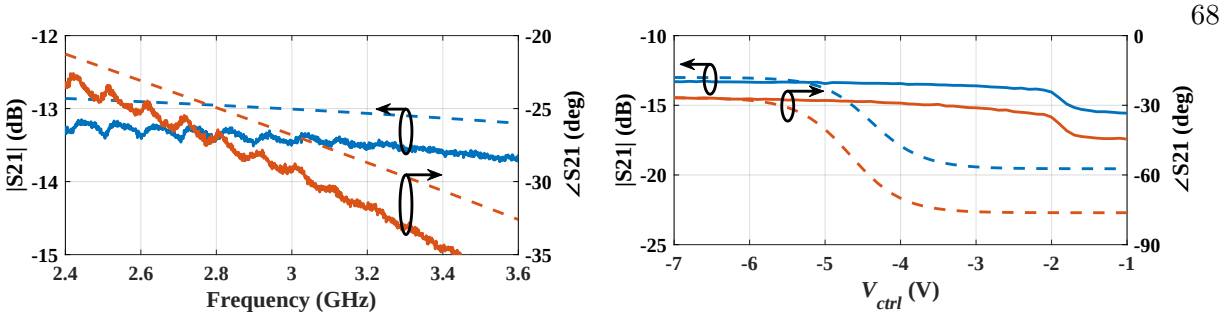


Figure 4.8: Phase shifter gain and phase comparison of measurements (solid) with simulated results (dashed) over (a) frequency and (b) control voltage.

axes of Fig. 4.8a, respectively. Again, the measured data (solid) is compared with the simulated results (dashed). With some additional loss in the circuit and physical implementation, |S21| is found to be $-13.4\,\text{dB}$ with a nominal phase shift of $-29°$ at $3\,\text{GHz}$ along with some ripple in the measurement for a control voltage of $-4\,\text{V}$.

At $3.0\,\text{GHz}$, the effect of the control voltage is depicted in Fig. 4.8b for a range of -7 to $-1\,\text{V}$. While |S21| unintentionally varies by roughly $2\,\text{dB}$, the phase can be tuned by approximately $18°$, which is significantly lower than the expected range that was simulated. The difference is again related to the dc probe parasitic inductance as well as the fact that the diode models are known to not be very accurate for this process, and most likely accounted for the frequency shift of the tuning circuit. Regardless, this phase shifter enables the canceller to tune over the frequency band of interest, which allows it to enhance its transmit-to-receive isolation, as shown in Section 4.4.

4.4 Measured Results

Both active circulators are measured on a probe station from Cascade Microtech, as shown in Fig. 4.9. An Agilent Technologies' N5222A network analyzer is utilized for the small-signal measurement of the impedance match, amplifier gain and cancellation results that are discussed below. The PA and LNA linearity metrics are characterized using an Agilent Technologies' E8257D signal generator and an N9918A FieldFox spectrum analyzer controlled by MATLAB. All results

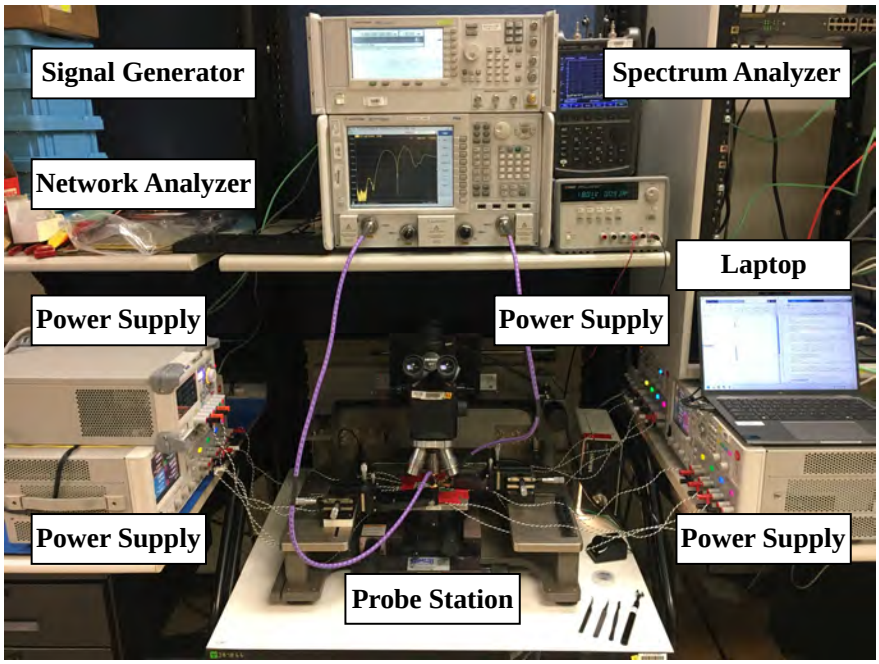


Figure 4.9: Photo of the measurement setup, highlighting the probe station, power supplies, test equipment, and laptop.

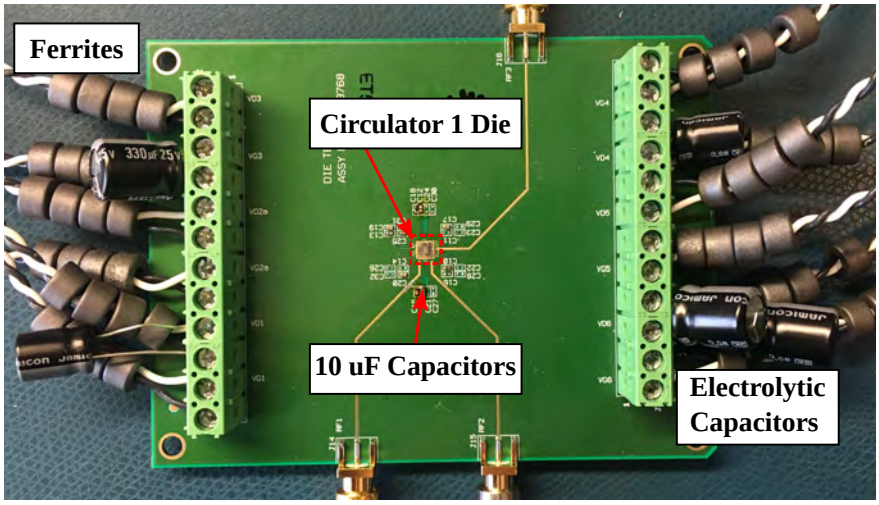
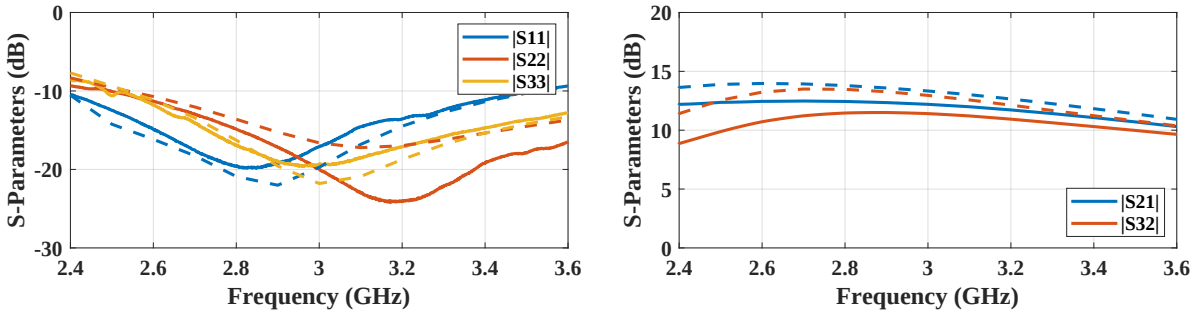


Figure 4.10: PCB utilized to test the active circulator with the one-tap canceller.

discussed here focus on evaluating the overall architecture and performance independent of a specific environment or antenna impedance, and thus, a 50 Ω load antenna termination is used to provide a performance baseline for well-matched designs.

As seen in the chip layout of Fig. 4.4, the active circulator with one canceller tap requires 12



(a) (b)

Figure 4.11: Active circulator with the one-tap canceller comparison of measurements (solid) with simulated results (dashed) for s-parameters, including (a) impedance matching and (b) transmit and receive gain.

different dc biases to supply the gate, drain and control voltages. For this reason, a printed circuit board (PCB) was created to mount the circulator die and facilitate its evaluation, where a photo of the PCB is shown in Fig. 4.10. As indicated, the board contains 10 μF surface-mount capacitors near the chip to provide decoupling of high-frequency signals on the dc bias lines, which are routed to the terminal block connectors on the left and right sides. Despite these surface-mount capacitors, the bias lines are found to be coupling to each other, and thus, 330 μF electrolytic capacitors and ferrites are added to the wires that connect the board to the various power supplies. Adding these components provides stability as well as robustness to changes in the off-board interconnect impedances that arise from the bias line wires and power supplies.

With dc voltages supplied using the PCB, the GSG RF pads of the first active circulator were probed to measure the small-signal s-parameters. Fig. 4.11a provides an indication of the port matching, and plots the |S11|, |S22|, and |S33| parameters. Collectively, they are seen to be below -10 dB between 2.5 and 3.5 GHz, and the measurements (solid) show fairly good agreement with the simulated results (dashed). Next, the transmit (|S21|) and receive (|S32|) gains were evaluated, with results plotted in Fig. 4.11b. The gains measure 12.2 and 11.4 dB for the PA and LNA, respectively, and again match the expectations well, with the exception of some additional losses and roll-off seen at the lower frequencies.

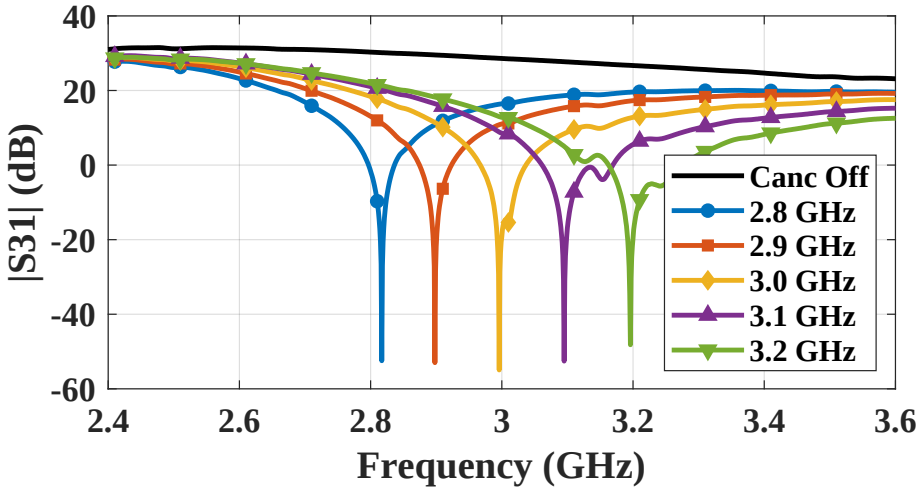


Figure 4.12: Active circulator with the one-tap canceller transmit-to-receive coupling with the canceller tuned to different frequencies, compared to being off.

Finally, the measurement of the critical transmit-to-receive isolation (|S31|) was conducted, with the results plotted in Fig. 4.12. As discussed in Section 4.3, the tunable amplifier and phase shifter of the one-tap integrated canceller were initially set to the middle of their tuning range, and yielded a maximum isolation of 54.9 dB at 3 GHz. The phase shifter was then tuned by changing V_{ctrl} over its full range along with adjusting the canceller tap's variable-gain amplifier to demonstrate the ability to continuously maintain more than 50 dB of transmit-to-receive isolation from 2.8 to 3.2 GHz, as depicted in Fig. 4.12, with tuning steps of 100 MHz plotted for illustrative purposes. The nominal |S31| with the canceller off is also plotted to provide a sense of how much cancellation is achieved by the device. It is worth noting that no comparisons are made to simulation for these results because the numerical precision of simulators cannot accurately predict the quantization errors and tolerances seen in the real world.

In addition to these s-parameter measurements, the transmit power handling and receive noise figure were also characterized. The transmit (from ports 1 to 2) output 1-dB compression point (OP1dB) is found to be 15.3 dBm, while the receive (from ports 2 to 3) noise figure is 7.8 dB, both assessed at 3 GHz with the canceller enabled. Additionally, the drain bias for each amplifier produces a current draw of approximately 50 mA that results in the active circulator having a

total current consumption of 250 mA, where the one-tap canceller path consumes 150 mA of that. It should be noted that when IBFD operation is not needed, such as for longer-range radar, the canceller can be disabled and the current reduced to 50 mA for each transmit and receive. Lastly, the overall chip size is 2.8×2.8 mm with an active area of roughly 2.0×2.2 mm.

4.5 Chapter Conclusion

This chapter presents an active circulator front-end with an integrated tunable canceller having one canceller tap that was fabricated in the WIN Semiconductors NP12-01 0.12 μm GaN process. An overview of the design architecture is discussed and the equations that govern the cancellation are formulated to verify the concept. Details on the individual amplifier and phase shifter components are highlighted, where measurement results of the standalone test circuits demonstrate good agreement with simulated expectations. The performance of the complete chip is also evaluated and provides the desired gain in the transmit and receive paths as well as successfully suppresses the transmit signal at the receiver by 50 dB, which is tunable over the 2.8−3.2 GHz range. Enhancements to this active circulator design are discussed in the following chapter. The material presented in this chapter is currently in press [72].

Chapter 5

IBFD Front-End Two-Tap Active Circulator

5.1 Introduction

In the previous chapter, an active circulator concept is introduced and focuses on a design that uses a one-tap integrated canceller, which successfully demonstrates the practicality of the architecture. This chapter presents the extension of the concept to introduce a second canceller tap, making the circuit slightly more complex, but improving the frequency coverage. The complete chip layout of the active circulator with the two-tap integrated canceller ($N = 2$) is shown in Fig. 5.1 with the power amplifier (PA), low-noise amplifier (LNA) and port placements similar to the previous version. In addition to adding the extra canceller tap, this design includes three main improvements to the underlying circuits, focusing on the power dividers (including the antenna interface), amplifiers and tunable phase shifters, as discussed next.

5.2 Active Circulator Improvements

5.2.1 Power Divider Design

The first change relates to the power dividers that were previously implemented using capacitors, which resulted in an asymmetric division of the input signal, such that the splitter exhibited an S21 of $-3\,\mathrm{dB}$ and an S31 of $-5.2\,\mathrm{dB}$ at $2.8\,\mathrm{GHz}$, as visualized with the dashed lines in Fig. 5.2. The modification was made to incorporate custom Wye-type resistive splitters that would normally provide a symmetric 6-dB split using three resistors of $16.7\,\Omega$ each ($R = 50/3\,\Omega$). While that

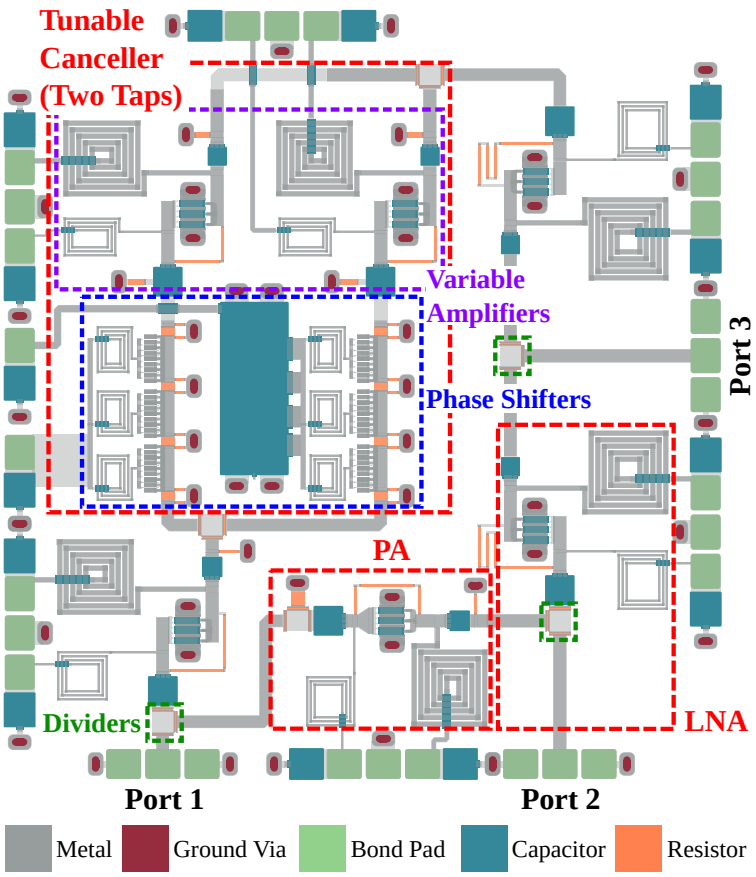


Figure 5.1: Active circulator with two-tap tunable canceller chip layout with labeled ports matching Fig. 4.3, highlighting the PA, LNA and improved dividers, amplifiers and phase shifters.

resistor value provides perfectly-matched port impedances, there is an opportunity to reduce the splitter insertion losses at the expense of degrading the match. With this in mind, resistor values of 3.2 Ω are utilized instead, which yields symmetric insertion and return losses of 4 and 12 dB, respectively, and improves the splitter performance over the previous version, as seen with the solid lines in Fig. 5.2. This comparison plot also highlights the enhanced flatness across the frequency band.

5.2.2 Amplifier Design

The second upgrade involves the amplifiers, which again center around a $6 \times 100\,\mu$m device, but additionally incorporate a feedback resistor (R_{FB}) to improve the amplifier's stability, as seen

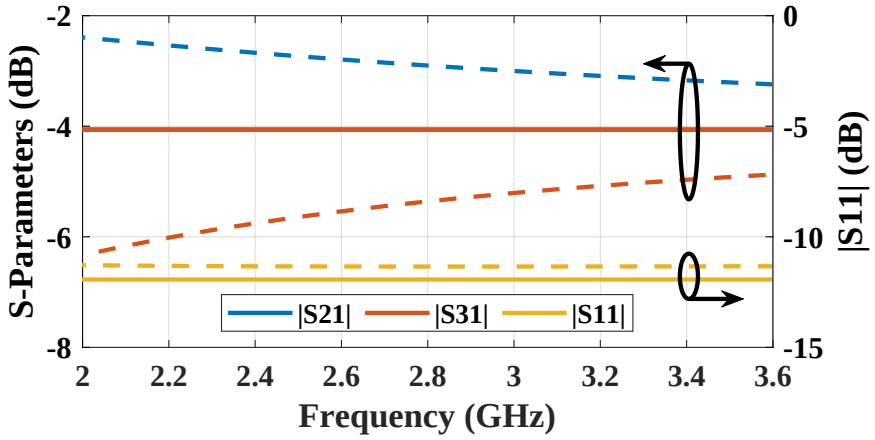


Figure 5.2: Simulated comparison between the power dividers used in the one-tap (dashed) and two-tap (solid) canceller designs, where S21 and S31 are identical for the latter.

in the lower part of Fig. 5.3a. Similar to the previous design, capacitors (C_g and C_d), inductors (L_g and L_d) and microstrip transmission lines are used to match the transistor to 50 Ω as well as nominally supply the gate and drain bias voltages, V_g and V_d, with −1.5 and +28 V, respectively. In addition to these elements, shunt input and output resistors (R_{IN} and R_{OUT}, respectively) are added to further improve the match over a wider bandwidth.

5.2.3 Phase Shifter Design

The upper part of Fig. 5.3a illustrates the third improvement made to this design iteration, and highlights a modified phase shifter design. Similar to before, this circuit is constructed using reverse-biased diodes and π-network attenuators, but now contains an additional section, such that there are three diodes and four attenuators. This extra section allows the circuit to tune over a wide range of phases, which translates to wider frequency coverage. Since the modified amplifier has a slightly higher gain than before, the baseline attenuation of the phase shifter is increased to 20 dB (using four 5 dB attenuators) to maintain a total gain near 0 dB for the canceller tap. The schematic diagram not only depicts both the improved phase shifter and amplifier, but also their nominal component values.

Due to limited fabrication area for test structures, only one complete canceller tap was

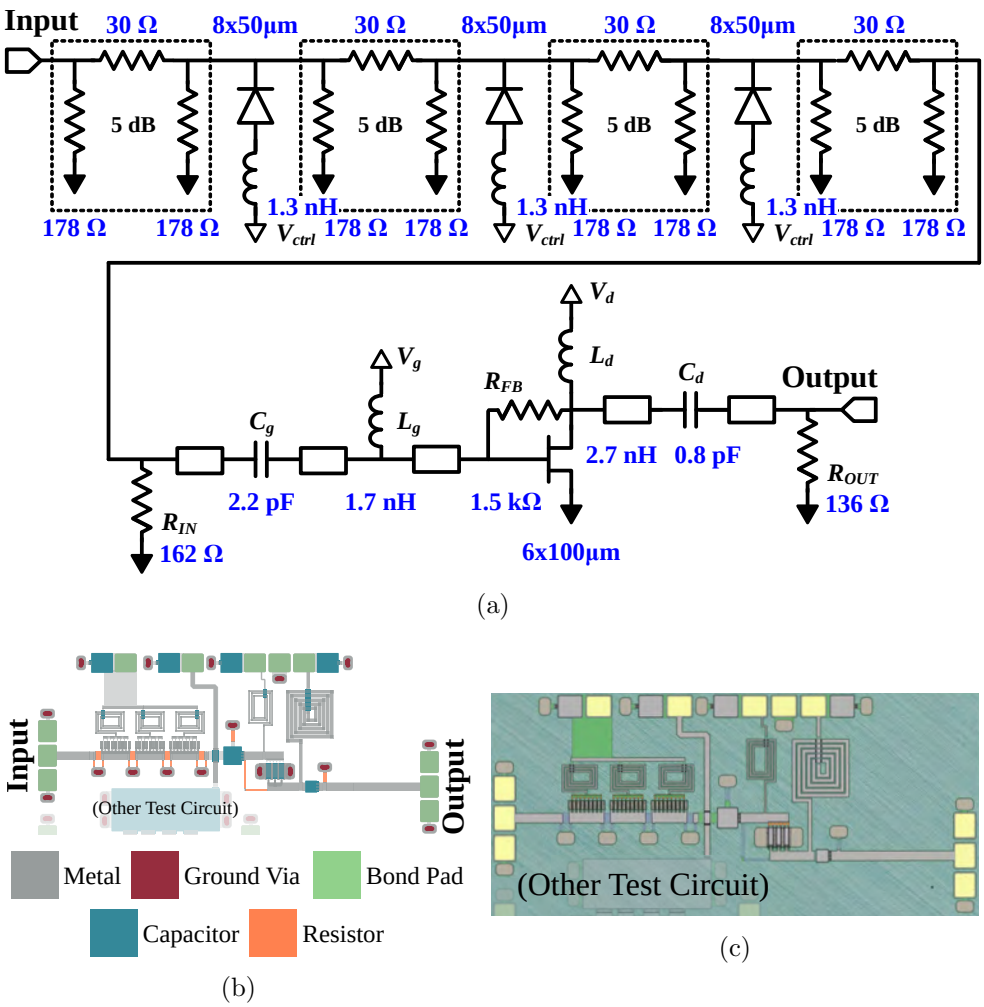


Figure 5.3: Two-tap canceller circuit (single tap shown) with improved phase shifter and amplifier design: (a) schematic, (b) layout and (c) photo with an active area of 1.5×0.6 mm.

created, as seen in the layout of Fig. 5.3b and accompanying die photo of Fig. 5.3c. The circuit connected between the input and output ports is the canceller tap, which matches the schematic illustrated in Fig. 5.3a, and depicts GSG pads for the RF connections and capacitor-decoupled pads for the single V_{ctrl}, V_g, and V_d bias voltages. Additionally, the metal layers, ground vias and TaN resistors are illustrated. The S21 magnitude and phase responses of this improved canceller tap are plotted on the left and right axes of Fig. 5.4a, respectively, with the measurements (solid) compared to simulation (dashed). The results indicate a good agreement with the expected values, and yield −3.7 dB for |S21| with a baseline phase shift of −150° at 2.8 GHz for a control voltage of −5 V.

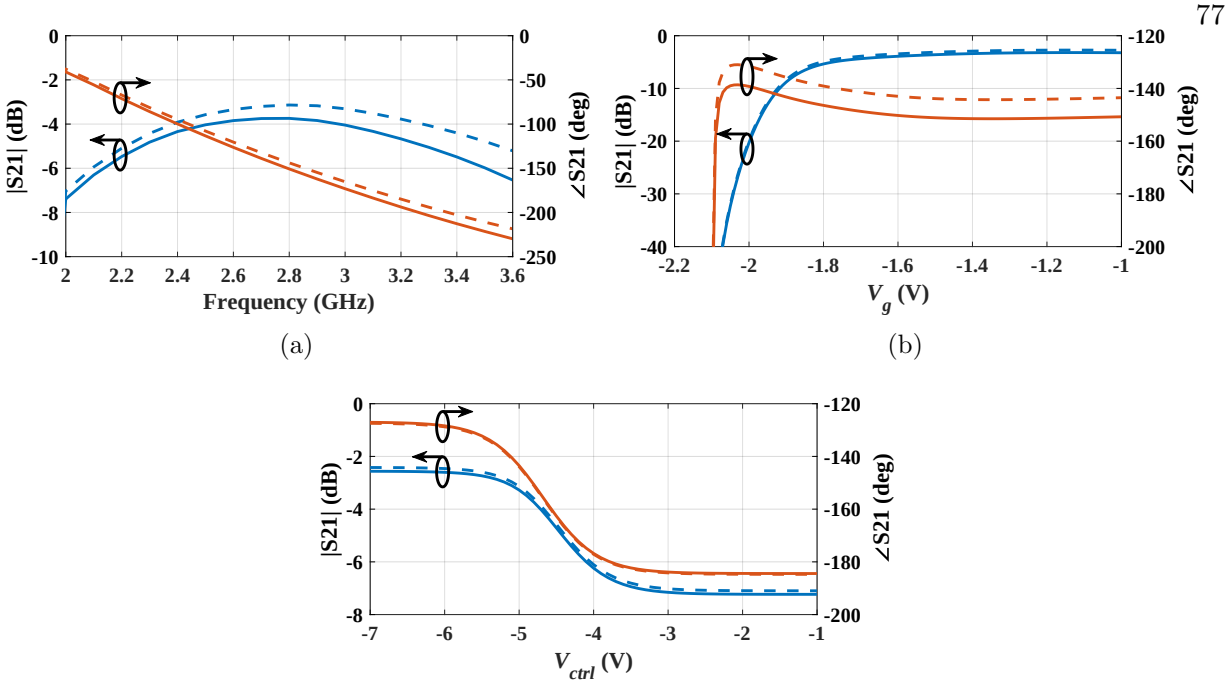


Figure 5.4: Complete tap circuit (phase shifter and amplifier) S21 gain and phase comparison of measurements (solid) with simulated results (dashed) over (a) frequency, (b) gate voltage and (c) control voltage.

Similar to the previous design, the tap's amplitude control is derived from changing the amplifier gate voltage over a tuning range of -2.2 to -1 V, where Fig. 5.4b compares the measured (solid) and simulated (dashed) performance for a fixed V_{ctrl} of -5.0 V and a frequency of 2.8 GHz. The plot indicates the ability to change the gain by more than 35 dB with less than 10° of consequential phase change. The tap's intentional phase control, on the other hand, comes from tuning the control voltage of the phase shifter circuit over a range of -7 to -1 V, where Fig. 5.4c shows the measured (solid) and simulated (dashed) results for a fixed V_g of -1.5 V and a frequency of 2.8 GHz. The figure illustrates that the phase can be varied by 57° from roughly $-127°$ to $-184°$, which represents a significant improvement over the previous design. For both of these tuning cases, the measured and simulated data show good agreement, which is aided by the use of dc wire bonds instead of probes. Overall, the benefit of the extended tuning performance on the transmit-to-receive isolation will be discussed in Section 5.3.

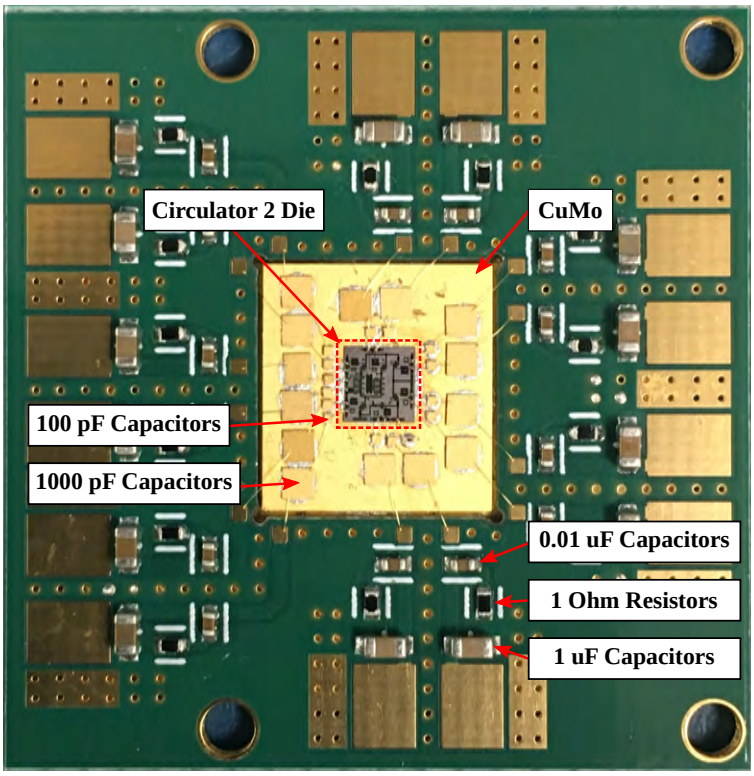
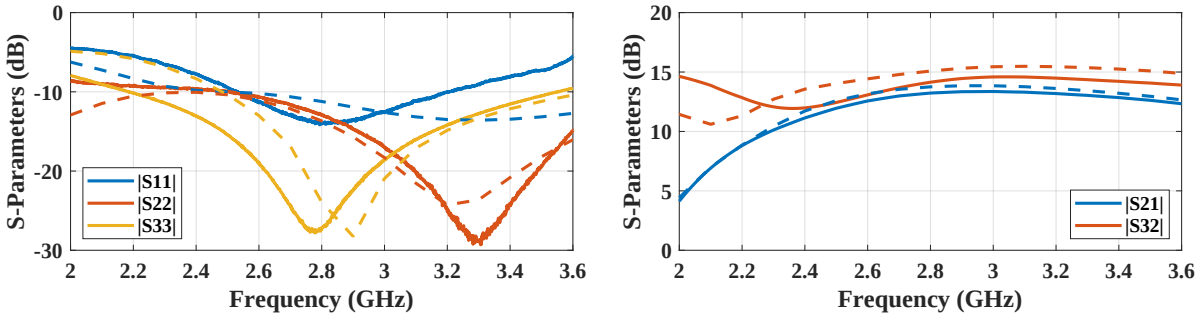


Figure 5.5: PCB utilized to test the active circulator with the two-tap canceller.

5.3 Measured Results

For the second circulator, another PCB is utilized to mount the chip and leverages lessons learned from the first iteration, specifically in the importance of minimizing the wire bond lengths and adding decoupling capacitors to improve robustness. Fig. 5.5 depicts the board used to supply the 14 different dc connections for the gate, bias and control voltages. Each of these lines are connected to the dc bond pads illustrated in Fig. 5.1 using gold bond wires. The length of these wires is minimized by attaching them to 100 and 1000 pF single-layer decoupling capacitors mounted on a copper-molybdenum (CuMo) alloy that not only offers high conductivity but also matches the coefficient of thermal expansion (CTE) of GaN to ensure proper die attachment. From the 1000 pF capacitors, bonds are made to pads on the PCB where surface-mount components provide additional decoupling in the form of 0.01 μF capacitors connected in series with 1 Ω resistors as well as successive 1 μF capacitors.



(a) (b)

Figure 5.6: Active circulator with the two-tap canceller comparison of measurements (solid) with simulated results (dashed) for s-parameters, including (a) impedance matching and (b) transmit and receive gain.

5.3.1 S-Parameters

Similar to the previous design, the GSG RF pads on the chip were probed to measure the small-signal s-parameters, beginning with the impedance matching of the three ports, as shown in Fig. 5.6a. This plot displays the |S11|, |S22| and |S33| performance over frequency, and illustrates that the device is matched with all values below -10 dB over the 2.5 to 3.2 GHz band. The comparison of these measurements (solid) with simulations (dashed) indicates that there is a slight shift downward in frequency, but this does not impact the overall operation. Next, the transmit (|S21|) and receive (|S32|) gains are evaluated to be 13.2 and 14.1 dB, respectively, at the center of the band (2.8 GHz), where the wideband results are plotted in Fig. 5.6b. Other than some deviation at the lower frequencies, the measured (solid) and simulated (dashed) results maintain the same shape, but illustrate some additional losses in the measurements. Despite the differences, these gain numbers still represent an improvement over the first active circulator design.

Finally, the transmit-to-receive isolation (|S31|) and associated tuning ability of the two-tap canceller are evaluated, with the results plotted in Fig. 5.7. With the increase in tuning variables from 2 to 4 between the design iterations, a straightforward multivariable gradient descent algorithm is employed to optimize the phase and amplitude settings of the two taps (the algorithm was chosen based on previous research [66, 79] and does not focus on the tuning speed). This results in the

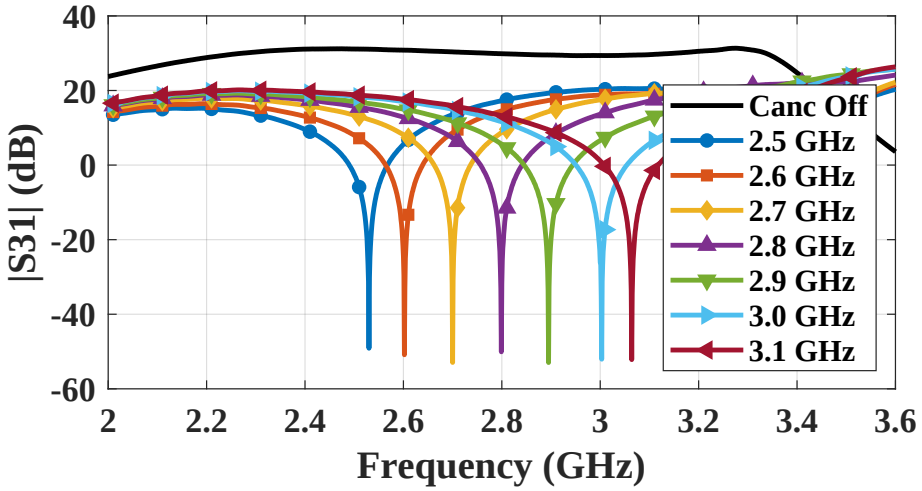
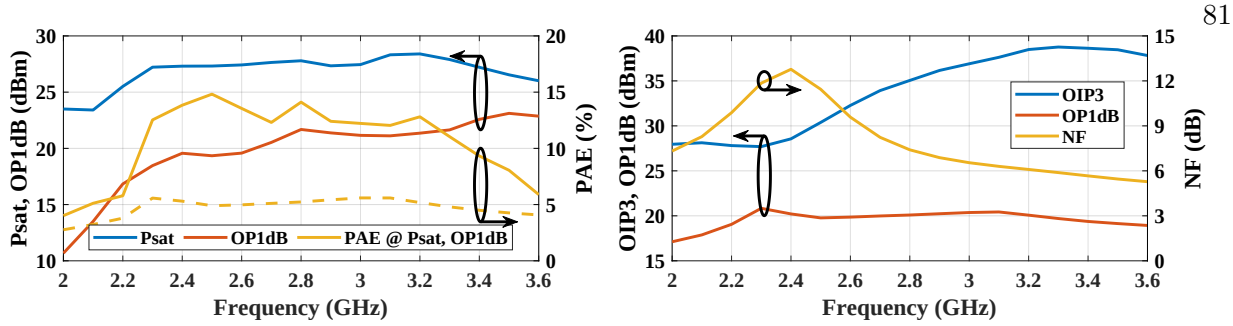


Figure 5.7: Active circulator with the two-tap canceller transmit-to-receive coupling with the canceller tuned to different frequencies, compared to being off.

isolation being enhanced to 50 dB (or the transmit-to-receive leakage being minimized to −50 dB) over the frequency tuning range of 2.5 to 3.1 GHz, which represents an enhancement over the previous design. Similar to before, these measurements are not plotted along with simulations due to the inaccurate comparisons that would result.

5.3.2 PA and LNA Performance

In addition to the small-signal s-parameter measurements, the transmit power handling of the PA (with the canceller enabled) is evaluated by measuring the saturated output power (Psat), OP1dB and power added efficiency (PAE). These metrics are plotted versus frequency in Fig. 5.8a, where the PAE is assessed both at the Psat (solid line) and OP1dB (dashed line) operating points. At 2.8 GHz, the graph illustrates a Psat of 27.8 dBm and an OP1dB of 21.7 dBm along with a PAE of 14.1% and 5.2% at the Psat and OP1dB powers, respectively. Overall, the linearity results are fairly flat over the frequency range and are representative of the typical characteristics for this device size ($6 \times 100\,\mu$m). It should be noted that the PAE for the device by itself is simulated to be approximately 40%, but the insertion loss of the input and output power dividers reduces the measured efficiency between ports 1 and 2.

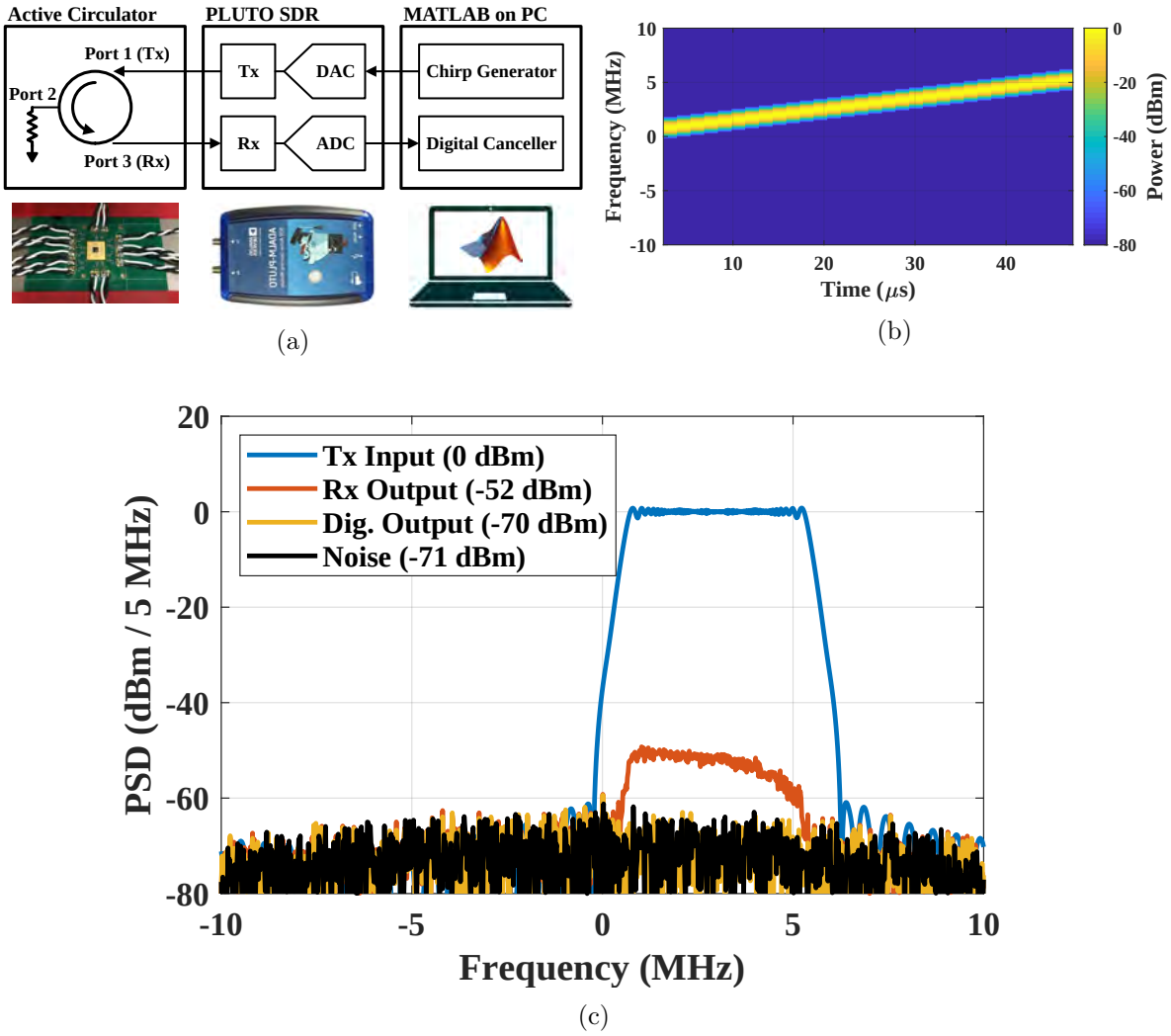


(a) (b)

Figure 5.8: Active circulator with the two-tap canceller (a) Psat, OP1dB and PAE at Psat (solid) and OP1dB (dashed) for the PA, and (b) OIP3, OP1dB and NF for the LNA.

Additionally, the linearity and noise performance of the LNA are evaluated by measuring the output third-order intercept point (OIP3), OP1dB and noise figure, with the results plotted over frequency in Fig. 5.8b. At 2.8 GHz, the OIP3 is found to be 35.1 dBm and the OP1dB is 20.1 dBm, along with the noise figure measuring 7.4 dB (again, with the canceller enabled). These metrics change slightly over the frequency range, but correspond to changes in the device gain, or |S32|, as seen in Fig. 5.6b.

While measured with additional detail and presented over frequency, both the PA and LNA performance indicate improvements compared to the previously discussed active circulator with the one-tap canceller. Additionally, the drain bias for each amplifier was recorded and yields a current draw of roughly 65 mA, which produces a total current consumption of 390 mA for the active circulator, where 260 mA comes from the two canceller taps. It should be noted that when IBFD operation is not needed, such as for longer-range radar, the canceller can be disabled and the current reduced to 65 mA for both transmit and receive. Finally, the overall chip size is 2.8×3.0 mm with an active area of approximately 2.3×2.5 mm, and the key metrics for the two active circulators are compared with others in Section 5.4.



(a) (b)

(c)

Figure 5.9: (a) Setup used to evaluate the active circulator with the two-tap canceller using a PLUTO SDR, radar waveform and digital cancellation; (b) spectrogram of linear-frequency modulated (LFM) signal; and (c) power spectral density of the 5-MHz chirp at the Tx input and Rx output of the active circulator as well as the signal after digital cancellation, compared to the Rx noise floor.

5.3.3 Modulated-Signal Characterization

In order to verify the IBFD system performance for the multifunction radar application previously described in Chapter 4, a software defined radio (SDR) controlled using MATLAB running on a laptop is connected to the active circulator with the two-tap canceller. Fig. 5.9a illustrates the block diagram of the measurement setup, where a realistic radar signal, specifically a linear

frequency-modulated (LFM) pulse waveform (i.e. radar chirp), is generated within MATLAB and sent to the DAC within a ADALM-PLUTO SDR from Analog Devices. This SDR is based on the Analog Devices AD9363 (a highly integrated RF agile transceiver) and a Xilinx Zynq Z-7010 FPGA. It provides RF coverage from 325 MHz to 3.8 GHz and supports instantaneous bandwidths up to 20 MHz. The Tx output of the SDR is connected to the Tx input (port 1) of the circulator, the antenna port (port 2) is terminated with a 50 Ω load (similar to the previous measurements) and the circulator's Rx output (port 3) is connected to the Rx input of the SDR. The ADC data is sent back to MATLAB for subsequent digital cancellation using the complex data samples. Photos of the three corresponding pieces of the setup are depicted below the system block diagram.

Fig. 5.9b shows the LFM waveform spectrogram, which provides a visualization of the chirp signal over the instantaneous bandwidth as it varies with time. The signal is offset from 0 MHz to avoid local oscillator (LO) leakage that results from the direct-conversion architecture operating in IBFD mode. The waveform sweeps over a pulse bandwidth of 5 MHz (from 0.5 to 5.5 MHz) in approximately 45 μs, which is a common bandwidth for weather surveillance [126] and wider than the 1.3 MHz used for air traffic control radars [148]. For this pulse width, the blind range can be calculated using

$$R_{min} = \frac{c_0 \cdot (\tau + t_{sw})}{2}, \tag{5.1}$$

where R_{min} is the minimum measuring range (blind range), c_0 is the speed of light, τ is the transmit pulse width, and t_{sw} is the switching time between transmit and receive. If $t_{sw} = 0$ is assumed, a blind range of 6.75 km is calculated for a 45 μs pulse width, which would be reduced to 0 m when IBFD is enabled, emphasizing its need in multifunction radar scenarios. The power spectral density (PSD) plot of Fig. 5.9c graphs the LFM waveform in the frequency domain, where the legend labels are relative to the active circulator, such that the Tx input represents the signal output by the SDR that is connected to port 1 of the circulator. It should be noted that this plot illustrates the signals at baseband, but a carrier frequency of 2.8 GHz is utilized for the measurements.

The two-tap canceller weights are tuned to suppress the SI of the chirp waveform, and provide

52 dB of isolation between ports 1 and 3 (similar to the results presented in Fig. 5.7). The remaining SI signal (the Rx output from the circulator) is digitized using the SDR and the complex data samples are sent to MATLAB for processing. The subsequent digital cancellation block consists of a complex 32-tap finite impulse response (FIR) filter with its weights computed using a minimum mean square error (MMSE) estimator, which could be done in real-time with additional compute resources [76]. The output of the digital canceller reduces the SI signal to −70 dBm, providing a total SI suppression of 70 dB, which is within 1 dB of SDR's noise floor, also plotted in Fig. 5.9c for reference. These results indicate that the active circulator can effectively operate with realistic radar waveforms and avoids introducing unwanted noise, nonlinearities and/or spurious signals that would make subsequent cancellation more challenging.

5.4 Chapter Conclusion

This chapter presents a second active circulator front-end that builds upon the architecture introduced in Chapter 4, and was also fabricated using the WIN Semiconductors NP12-01 0.12 μm GaN process. In addition to including a second integrated canceller tap, this design also incorporates improvements to the power dividers (including the antenna interface), amplifier design and tunable phase shifters. It similarly demonstrates gain in the transmit and receive paths, and provides tunable transmit-to-receive isolation of more than 50 dB over 2.5—3.1 GHz, which represent the first known instances of these capabilities for a GaN-based active circulator. This front-end is also evaluated using a LFM chirp waveform that is common in multifunction radar systems, and with the addition of a subsequent digital cancellation process produces a total SI suppression of 70 dB.

Table 5.1 presents a performance summary of active circulators implemented using III-V compound semiconductors. It lists the materials process technology; reported frequency range; transmit (|S21|) and receive (|S32|) gains; transmit-to-receive leakage (|S31|); if the leakage/isolation was tunable; OP1dB for the transmit-to-antenna path; noise figure for the antenna-to-receive path; and the chip area. As previously mentioned in Chapter 4, few active circulator designs offer transmit

Table 5.1: Summary of Measured Active Circulators using III-V Compound Semiconductors

Ref	**Technology**	**Freq. (GHz)**	**Gain (dB)**		**Tx-to-Rx Leakage, |S31| (dB)**	**Tunable**	**Tx-to-Ant OP1dB (dBm)**	**Ant-to-Rx NF (dB)**	**Size (mm^2)**
			|S21|	**|S32|**					
[41]	GaAs	0.1–10	−7	−6	−20	N	−9	–	0.9
[146]	GaAs	0.1–15	−4.5	−4.5	−15	N	–	–	0.3
[82]	GaAs	37–43	−3	−4	−15	N	–	–	20.0
[10]	InP	35–40	−5	−7	−30	N	–	–	3.3
[38]	GaAs	3.8–4.2	7.6	4	−22	N	18	5.5	5.0
[19]	GaAs	10.2–12.8	−4.5	−4.5	−35	N	–	4.5	16.0
[99]	GaAs	8–12	2.4	2.4	−13	N	–	–	6.3
[150]	GaN	27–29	−4.5	−3.6	−44	N	14	–	1.1
This Work (One-Tap)	GaN	2.8–3.2	12.2	11.4	−50	Y	15	7.8	7.8
This Work (Two-Taps)	GaN	2.5–3.1	13.2	14.1	−50	Y	22	7.4	8.4

and receive gain, regardless of their technology and frequency range. Additionally, the transmit-to-receive isolation, or leakage, is seen to vary significantly and previously-reported approaches have not incorporated a tunable mechanism to provide high isolation over the complete frequency range. Lastly, many have not published their transmit power handling or receive noise figure numbers, both of which are important aspects to consider when incorporating these devices into IBFD array systems.

As previously stated, these front-ends are intended to be integrated into multichannel phased arrays in order to leverage the array gain and compensate for the significant path loss of radar links. With that goal in mind, the next steps for these designs include focusing on a scalable power

distribution scheme that will begin with continued testing to reduce the number of different gate and drain bias lines, while maintaining electrical stability and sufficient decoupling between the various circulator stages. Additionally, the chips will be integrated behind antenna elements in such a way that allows for an air-cooled thermal solution that can be married to a fully-digital backend, which will be utilized to calibrate both the individual active circulators as well as the composite IBFD array. Finally, with the architectural concept verified, future designs of these GaN MMICs will focus on optimizing the PA and LNA for their respective performance metrics and allowing these active circulators to be inserted in multifunction array systems. The material presented in this chapter is currently in press [72].

Chapter 6

System-Level Array Integration

6.1 Introduction

For the purpose of this chapter, system-level array integration refers to populating copies of a front-end circuit (and other associated transceiver components) behind multiple antenna elements. It additionally means interfacing to data converters for the purpose of creating a complete phased array, similar to the diagram of Fig. 3.1. While the front-ends themselves are often connected to a single antenna, or evaluated with a fixed load, it is the combination of multiple channels that introduces the problematic crosstalk interference (XI) and establishes the IBFD system-level performance, as discussed in Chapter 3. Some of the main challenges associated with system integration include the need for multiple working copies of the front-end and transceiver hardware as well as a multichannel digital backend. While all of these subsystems require significant individual design and testing time, the need for significant quantities of them (oftentimes unique components) also increases the cost of creating a prototype with even a handful of channels, as evidenced in the limited set of systems presented in Fig. 2.7. Additionally, the firmware and software of the digital backend necessitate the use of skillsets that span different knowledge domains, and are often covered using multi-disciplinary engineering teams within larger research organizations.

With that said, advanced system models can be created to be both cost-effective and highly accurate for phased arrays that are co-designed with analog and digital signal processing elements. The cost-effective aspect comes from the fact that large array sizes can be synthesized without the need for redundant hardware, and the high accuracy arises from the incorporation of measured data

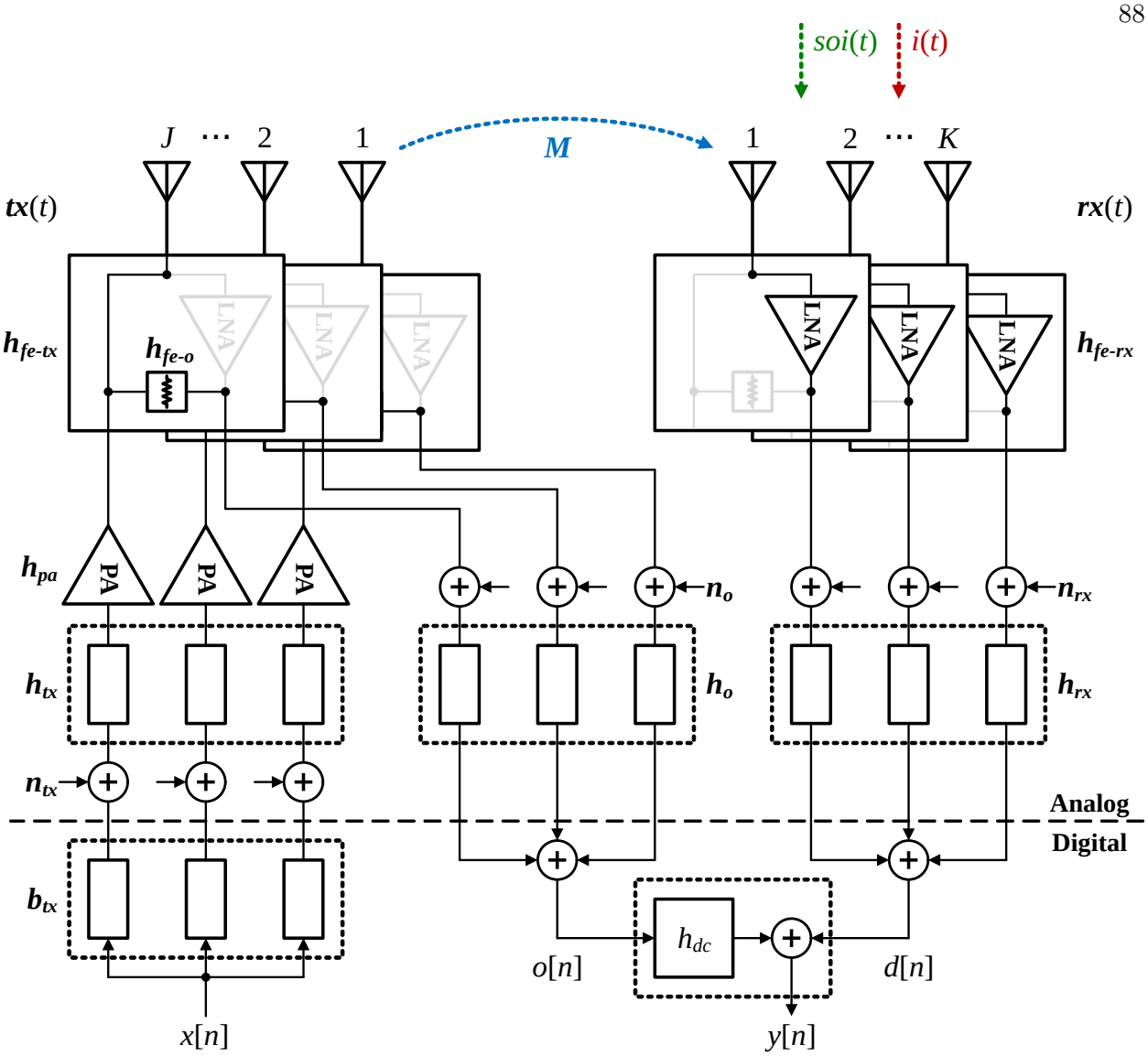


Figure 6.1: Signal model for an aperture-level IBFD array system evaluation with transmit input $x[n]$; mutual coupling matrix $\boldsymbol{M}$; signal-of-interest $soi(t)$; external interference $i(t)$; and combined receive output $y[n]$, where the transmit beamformer $\boldsymbol{b_{tx}}$ and digital filter h_{dc} reduce the crosstalk interference (XI). Note that bold variables represent vectors and/or matrices.

for the antenna array and front-end electronics, which allows the model to capture the frequency dependence of the components' linear, nonlinear and noise parameters. This chapter focuses on the integration of antennas with front-end circuits and digital signal processing to demonstrate the system-level capabilities for both aperture- and element-level IBFD phased arrays.

6.2 Aperture-Level IBFD Array

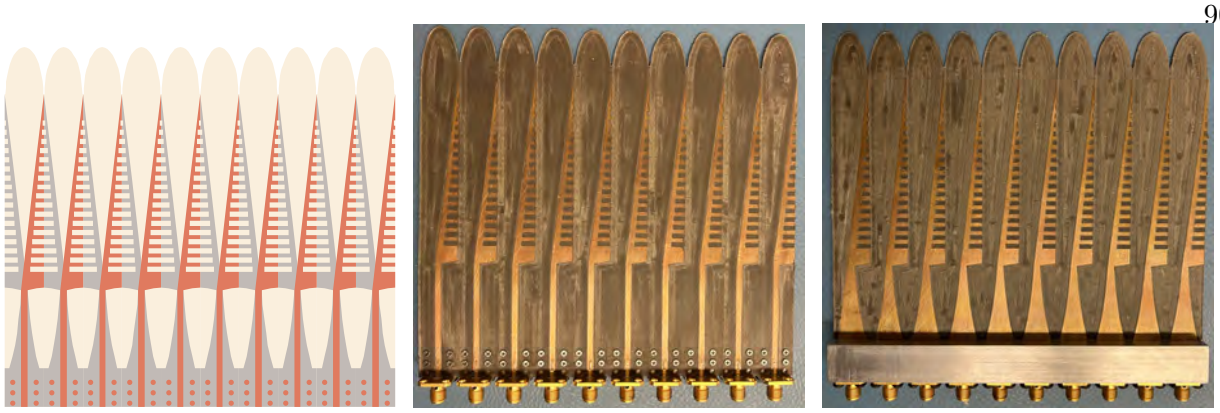
The signal model for an aperture-level IBFD array with J transmit channels and K receive channels is shown in Fig. 6.1. This diagram illustrates the RF/analog components and digital elements above and below the dashed horizontal line, respectively. The input signal is denoted as $x[n]$ in the bottom left corner with $E\left[|x[n]|^2\right] = 1$ and is multiplied by a vector of transmit beamforming coefficients ($\boldsymbol{b_{tx}}$) before being converted into the analog domain, where quantization and thermal noise ($\boldsymbol{n_{tx}}$) are added. Afterward, the signals travel through individual transmitter channels ($\boldsymbol{h_{tx}}$) before being amplified by power amplifiers (PAs) and fed to front-end circuits ($\boldsymbol{h_{fe\text{–}tx}}$) that are connected to unique antenna elements and form the final outputs as vector $\boldsymbol{tx}(t)$. These signals are additionally routed through the front-end observation paths ($\boldsymbol{h_{fe\text{–}o}}$) before noise is added ($\boldsymbol{n_o}$), and they travel through observation receivers, with responses denoted $\boldsymbol{h_o}$, before being digitized.

At the receiver input, the XI from the transmitters is present and can be characterized using the array mutual coupling matrix ($\boldsymbol{M}$), where a signal-of-interest ($soi(t)$) and external interference ($i(t)$) can also be considered. When configured for receive operation, the front-ends enable low-noise amplifiers (LNAs) with responses captured by $\boldsymbol{h_{fe\text{–}rx}}$, where noise ($\boldsymbol{n_{rx}}$) is subsequently added to each channel. As seen, the signals connect through additional receive componentry ($\boldsymbol{h_{rx}}$) before being digitized for subsequent processing.

The following sections discuss the specific antenna array utilized; the front-end architecture and circuit performance with an integrated PA; an expanded description of the array signals and associated signal processing; and finally, the results of the system-integration evaluation with complex signals.

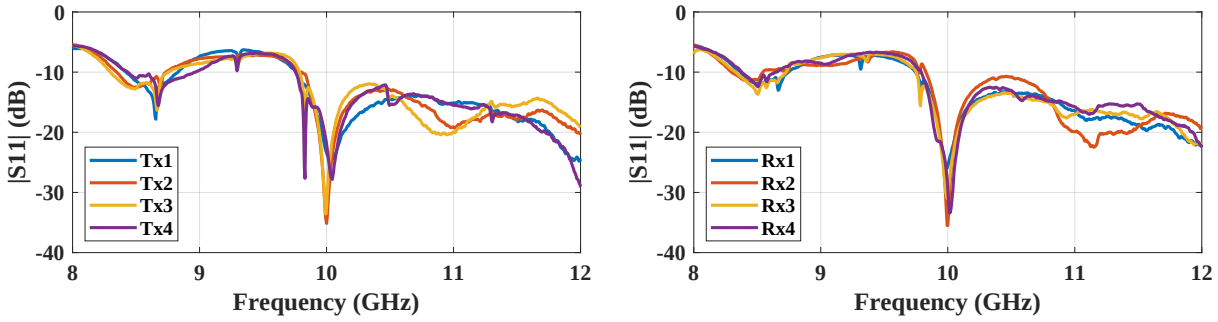
6.2.1 Antenna Array

The antenna utilized in this system is a linear array with 10 antipodal-Vivaldi elements that are designed to operate from 8 to 18 GHz [58]. Each individual element has a width of 590 mils,



(a) (b) (c)

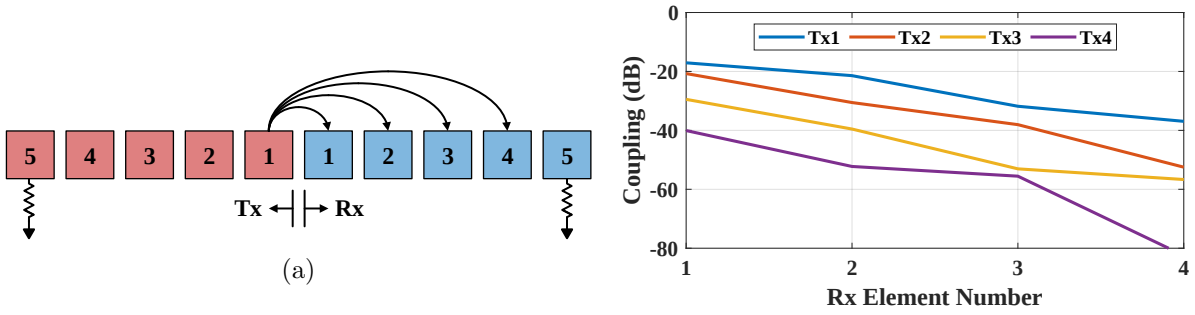
Figure 6.2: Antipodal Vivaldi array with 10 elements, highlighting the (a) model with top and bottom metal layers, and prototype photos with (b) top and (c) bottom views.



(a) (b)

Figure 6.3: Antipodal Vivaldi array |S11| measurements for the (a) four transmit channels and (b) four receive channels.

which corresponds to a 1/2-λ spacing at 10 GHz. Corrugations on the top and bottom metal layers are introduced to improve both the S11 and gain over the band. These are visualized in the model and prototype photographs shown in Fig. 6.2, which measures 5905×5438 mils and also show the end-launch SMA connectors attached on the bottom. Since the element conductors are on opposite sides of the substrate, antipodal arrays can exhibit high cross-polarization levels between the E- and H-fields. The cross-polarization is a function of the dielectric thickness, and in order to minimize this undesired effect, a Rogers RT/duroid 5880 substrate with a dielectric constant of 2.2 and a height of 31 mils was chosen.



(a) (b)

Figure 6.4: Antipodal Vivaldi array coupling, highlighting the (a) transmit and receive element diagram, and (b) coupling level from each transmit to each receive element.

In order to minimize the edge effects of this array, the elements on either end are terminated with 50 Ω loads. This reduces the total number of active elements to eight, where the four on the left were assigned to transmit and the other four set to receive. Figs. 6.3a and 6.3b illustrate the measured passive S11 magnitudes for each of the individual transmit and receive elements, respectively. While there are slight differences between the elements, the plots indicate that all are well-matched at 10 GHz. Fig. 6.4a depicts the numbered locations for both the transmit and receive elements as well as the terminated ones on the ends. Additionally, this figure illustrates the coupling paths from the first transmit element to each of the four receivers, where a total of 16 unique paths are generated between the 4×4 transmit-receive pairs (those for transmit elements 2 through 4 are omitted for clarity). The measured coupling results for all of these are plotted in Fig. 6.4b. As anticipated, the strongest coupling occurs between the elements on either side of the transmit/receive boundary (i.e. Tx1 to Rx1), which yielded a level of −17 dB. Unsurprisingly, this plot also illustrates that the coupling decreases as the distance between the transmit-receive pairs increases, such that coupling between Tx4 and Rx4 is the lowest at −82.3 dB. Based on these results, the mutual coupling matrix $\boldsymbol{M}$, referenced in Fig. 6.1, can be created and utilized for the signal processing discussed later.

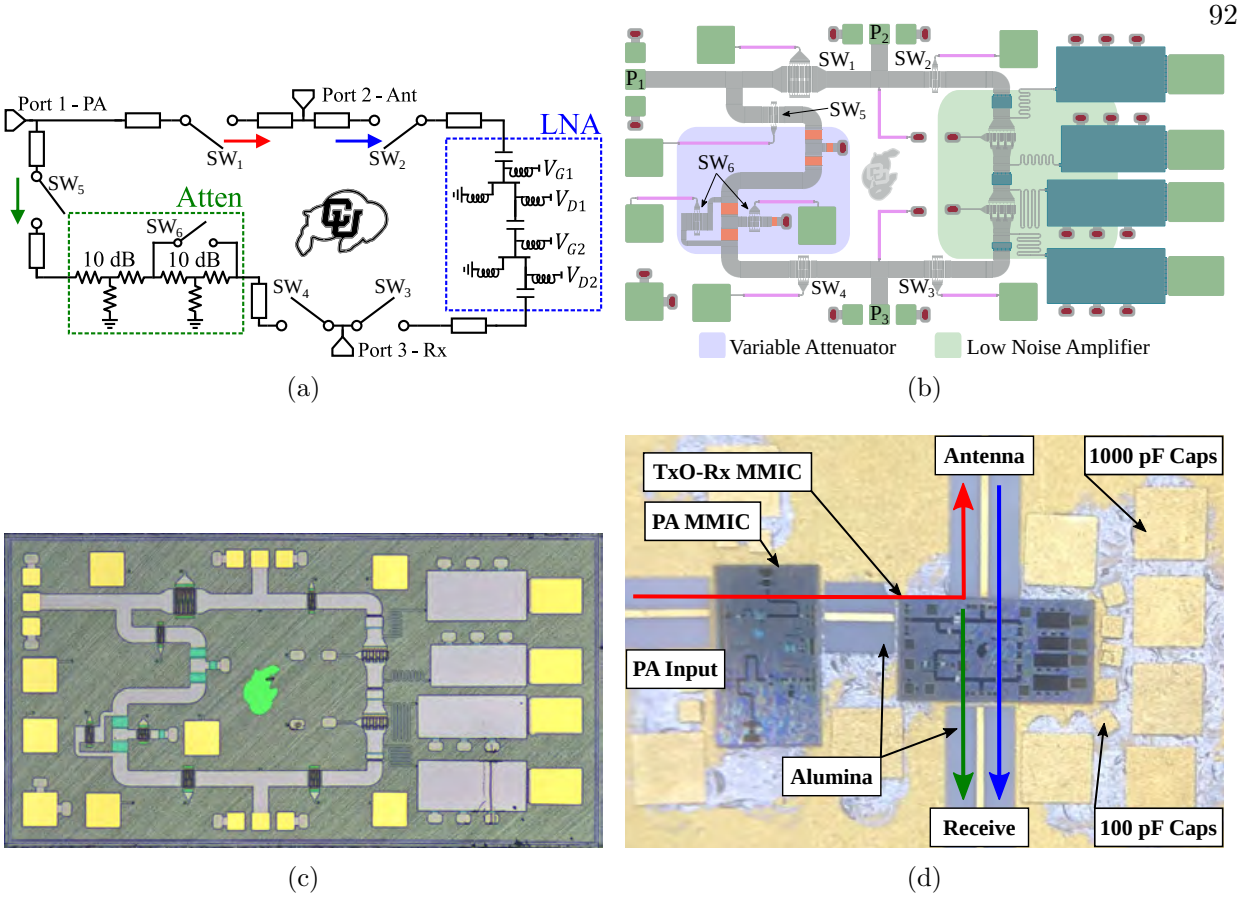


Figure 6.5: Aperture-level IBFD array front-end used for the system integration, highlighting the (a) schematic, (b) layout, (c) chip photo, and (d) integration with a single-stage power amplifier.

6.2.2 Front-End

The front-end circuit utilized for this system is different from those discussed in Chapters 4 and 5 not only because it operates at 10 GHz to match the antenna, but also because it is designed specifically for aperture-level IBFD arrays. As previously mentioned, the transmit observation receivers within these array architectures operate in a full-duplex mode, but can do so with a significantly degraded sensitivity compared to regular receivers. This is illustrated in Fig. 6.1, where different front-end configurations are selected for the transmit and receive elements based on the subarray divisions.

The schematic for the front-end circuit is depicted in Fig. 6.5a with port 1 connected to the

PA, port 2 to the antenna and port 3 to the receiver. Switches 1 through 5 provide the ability to select between transmit and receive modes as well as enable the transmit observation feedback. The transmit path through the front-end simply consists of a transmission line connected between ports 1 and 2, which minimizes the insertion loss and avoids a significant reduction of the output power, or degradation of the overall transmit efficiency. During transmission, the observation path between ports 1 and 3 is also active, where switch SW_5 is kept open such that the transmit signal is capacitively coupled through the off-state of the switch. This coupled signal is further attenuated by up to two 10 dB attenuators with resistive-tee structures that reduce the signal level before going to the observation receivers. When configured for receive operation (for elements not transmitting), port 2 routes to port 3 (with the other switches open) and the two-stage internal LNA is enabled to provide nominal sensitivity levels. The LNA is comprised of two $8\times50\,\mu$m devices with inductive source degeneration that yielded a noise figure around 2.2 dB at 10 GHz with a drain bias of 10 V and total current of 80 mA [58].

This front-end was fabricated as a GaN MMIC in the WIN Semiconductors 150 nm NP15-00 process where the chip layout is shown in Fig. 6.5b, and highlights the different ports as well as the variable attenuator and LNA sections. The size difference between the various switches is also illustrated, where switch SW_1 was designed with a $9\times150\,\mu$m device to support power handling up to 45 dBm and provide an insertion loss less than 0.25 dB. Fig. 6.5c depicts a photograph of the die that measured 3.2×1.8 mm and matches the chip layout. This MMIC is mounted on a gold-plated copper molybdenum (CuMo) carrier and wire-bonded to single-layer 100 and 1000 pF decoupling capacitors as well as 50 Ω alumina microstrip traces, as seen in Fig. 6.5d. This image also illustrates the integration with a PA, which was also fabricated in the WIN Semiconductors GaN 150 nm NP15-00 process. The PA is a single-stage design that utilizes a $6\times100\,\mu$m device, and demonstrates a small-signal gain of 15 dB, a peak power added efficiency (PAE) greater than 50%, and a P_{out} higher than 30 dBm at 10 GHz [92].

The measured small-signal s-parameter results of the combined PA and front-end circuit are plotted in Fig. 6.6. The transmit and associated observation paths produced gains of 12.7 and

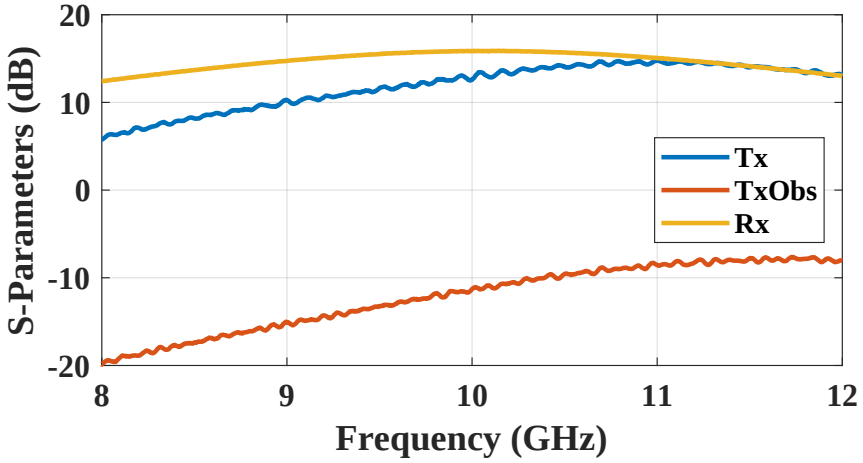


Figure 6.6: Measured s-parameters for the transmit, transmit observation and receive paths of the front-end integrated with the single-stage power amplifier.

−11.3 dB at 10 GHz, respectively. The transmit observation number corresponds to an attenuation of 24 dB with both 10 dB attenuators enabled, where additional attenuation could be added within the subsequent observation receiver to keep the signal below the ADC saturation point depending on the transmit output power, as discussed in Chapter 3. The receive-path performance is the same as the front-end by itself, and indicates that the LNA provides 15.8 dB of gain at 10 GHz. This LNA also demonstrates an output P1dB greater than 20 dBm, indicating that it could amplify the XI well above the receiver saturation level, which necessitates the use of additional signal processing in order to avoid it, as discussed in the following section [70].

6.2.3 Signal Processing

While the various components of Fig. 6.1 have already been identified, this section discusses the formulation of the transmit, observation and receive signals within the array as well as the computations necessary to determine the optimal transmit beamforming weights that reduce the XI at the receiver input. Starting with the common input signal, $x[n]$ (that becomes $x(t)$ after conversion), the transmitted signals can be formulated as

$$\boldsymbol{tx}(t) = (\boldsymbol{b_{tx}}\, x(t) + \boldsymbol{n_{tx}}(t))\, \boldsymbol{h_{tx}}\, \boldsymbol{h_{pa}}\, \boldsymbol{h_{fe\text{–}tx}}, \tag{6.1}$$

where the input is multiplied by the transmit beamforming weights as well as the other components within each channel. The digitally-combined observation signal can be derived using these outputs, such that

$$o[n] = \sum_{j=1}^{J} \left(tx_j(t)\, h_{fe\text{–}obs_j} + n_{o_j}(t) \right) h_{o_j}, \tag{6.2}$$

where the observation path within each front-end is individually utilized.

With the help of the mutual coupling matrix, the set of signals at the receiver input can be defined as

$$\boldsymbol{rx}(t) = \boldsymbol{M}\, \boldsymbol{tx}(t) + soi(t) + i(t), \tag{6.3}$$

where the SOI and external interference may or may not be present. These signals propagate through the different receive channels before being combined digitally to create a single output, according to

$$d[n] = \sum_{k=1}^{K} \left(rx_k(t)\, h_{fe\text{–}rx_k} + n_{rx_k}(t) \right)\, h_{rx_k}, \tag{6.4}$$

where a uniform weighting of the different channels is assumed. A finite-impulse response (FIR) filter is represented by h_{dc}, and is utilized to provide digital cancellation nominally using the combined transmit observation signals as inputs. Within the dashed box containing h_{dc}, the filtered version of $o[n]$ and total receive signal $d[n]$ are summed to create the final receiver output $y[n]$, which is simply defined as

$$y[n] = o[n]\, h_{dc} + d[n]. \tag{6.5}$$

When each transmitter is configured for an output of 20 dBm (assuming a uniform transmit beamformer with $\boldsymbol{b_{tx}} = 1$), the power levels for both the transmit and receive elements are illustrated in Fig. 6.7a along with a heatmap where the numbers listed are in dBm. Dictated by the coherent combining of the coupling defined by $\boldsymbol{M}$, this image clearly depicts the XI power at the input of each receiver being above the saturation level of -20 dBm, as discussed during the system analysis presented in Chapter 3.

In order to calculate the transmit beamforming weights that reduce this XI, two optimization goals need to be defined, namely maximizing the signal-to-noise-plus-interference ratio (SINR) and

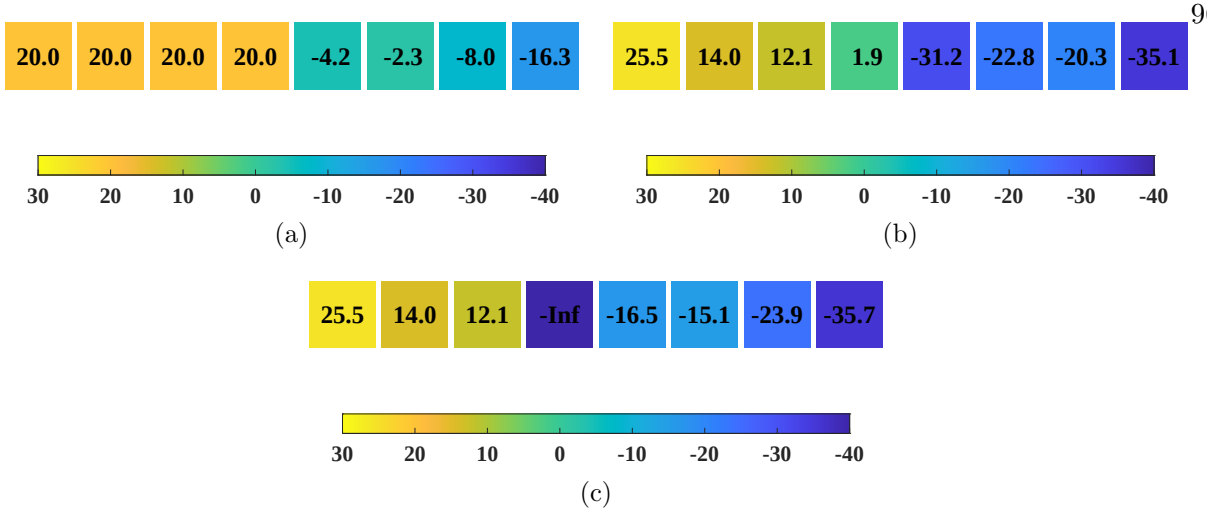


Figure 6.7: Simulated aperture-level IBFD array power levels in dBm for the antipodal Vivaldi array with the four transmit elements on the left and the four receive elements on the right for (a) uniform and (b) adaptive transmit beamforming cases, as well as (c) the adaptive case with Tx1 disabled.

minimally impacting the effective isotropic radiated power (EIRP). The former can be defined as

$$\text{SINR} = \frac{P_{\text{SOI}}}{P_{\text{XI}} + P_{N_{\text{rx}}} + P_I}, \tag{6.6}$$

where P_{SOI}, P_{XI}, $P_{N_{\text{rx}}}$, and P_I represent the average powers of the SOI, the XI, receiver noise, and external interference, respectively. The P_{XI} captures the power of the Tx signal ($x[n]$) that couples into the Rx beam, and can be expanded as

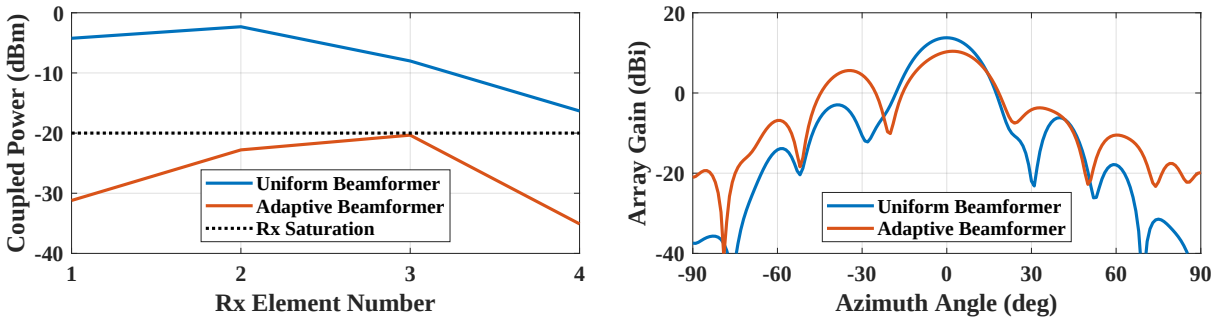
$$P_{\text{XI}} = \boldsymbol{M}\,\boldsymbol{h_{fe\text{–}tx}}\,\boldsymbol{h_{pa}}\,\boldsymbol{h_{tx}}\,\boldsymbol{b_{tx}}\,\boldsymbol{b_{tx}}^H\,\boldsymbol{h_{tx}}^H\,\boldsymbol{h_{pa}}^H\,\boldsymbol{h_{fe\text{–}tx}}^H\,\boldsymbol{M}^H, \tag{6.7}$$

where $(\cdot)^H$ represents the Hermitian operator, or complex conjugate transpose, for each vector or matrix, and all of the components that alter $x[n]$ before it reaches the receiver inputs are captured.

For the latter condition, the far-field EIRP is defined as the total transmit power plus the array gain, where the transmit beam in direction (θ_{tx}, ϕ_{tx}) can be described as

$$\text{EIRP}(\theta_{tx}, \phi_{tx}) = g(\theta_{tx}, \phi_{tx})\,\boldsymbol{b_{tx}}^H\,\boldsymbol{h_{tx}}^H\,\boldsymbol{h_{pa}}^H\,\boldsymbol{h_{fe\text{–}tx}}^H\,\boldsymbol{q_{tx}}(\theta_{tx}, \phi_{tx})\,\boldsymbol{q_{tx}}^H(\theta_{tx}, \phi_{tx})\,\boldsymbol{h_{fe\text{–}tx}}\,\boldsymbol{h_{pa}}\,\boldsymbol{h_{tx}}\,\boldsymbol{b_{tx}}, \tag{6.8}$$

where the individual element gain $g(\theta_{tx}, \phi_{tx})$ is assumed to be the same for all elements, and $\boldsymbol{q_{tx}}(\theta_{tx}, \phi_{tx})$ represents the far-field steering vector for a beam at angle (θ_{tx}, ϕ_{tx}). For a planar



(a) (b)

Figure 6.8: Simulated comparison of uniform and adaptive transmit beamforming effects on the (a) coupled power into each receive element, where the adaptive case reduces the power below the receiver saturation level and (b) the transmit array gain.

array, this is given by

$$\boldsymbol{q_{tx}}(\theta_{tx}, \phi_{tx}) = \exp\left[-j\frac{2\pi}{\lambda}\left(\boldsymbol{x_{tx}}\cos(\phi_{tx})\sin(\theta_{tx}) + \boldsymbol{y_{tx}}\sin(\phi_{tx})\sin(\theta_{tx})\right)\right], \tag{6.9}$$

where $\boldsymbol{x_{tx}}$ and $\boldsymbol{y_{tx}}$ are the x- and y-positions for each transmit element within the array, respectively [63].

With these goals in mind, the optimal transmit beamforming coefficients can be computed using

$$\boldsymbol{b_{tx}} = \left[\frac{\mathbb{M}}{||\mathbb{M}||_2} + \gamma_{tx}\, I\right]^{-1} \boldsymbol{q_{tx}}(\theta_{tx}, \phi_{tx}), \tag{6.10}$$

where the mutual coupling covariance matrix ($\mathbb{M} = \boldsymbol{M}^H \boldsymbol{M}$) is utilized and is normalized by dividing by the L2 norm. The γ_{tx} term is a diagonalization parameter that allows for the beamforming coefficients to be tuned in favor of either the SINR or EIRP goals, and is appropriately set to keep the XI power below the receiver saturation. The beamforming coefficients are constrained by the total transmit power P_{tx} according to

$$\boldsymbol{b_{tx_{norm}}} = \frac{\boldsymbol{b_{tx}}\sqrt{P_{tx}}}{||\boldsymbol{b_{tx}}||_2}, \tag{6.11}$$

which allows the amplitudes of the transmit signals to change, but only within a limited range.

With the measured data from the system model, these equations can be utilized to compute a set of transmit beamforming coefficients that minimize the XI present at the receive elements,

where Fig. 6.7b illustrates the corresponding power levels. By comparing Figs. 6.7a and 6.7b, the transmit outputs are seen to have changed for each of the four elements on the left and are reduced closer to the transmit-receive boundary in the middle. These modifications allow the XI at the input of the receivers to be kept below the saturation level of -20 dBm for each element, as visualized in Fig. 6.8a for the individual receivers.

In order to highlight the importance of all of the individual coupling paths, the transmitter with the lowest output power (Tx1) is disabled while the others maintained the same weights, as depicted in Fig. 6.7b. Fig. 6.7c illustrates that this relatively-small Tx1 power modification significantly changes the XI power at the receiver inputs, where the Rx1 and Rx2 levels are seen above the saturation threshold. If the beamforming weights were recomputed with only 3 active transmit elements, however, these XI levels could be reduced.

While the beamforming coefficients of Fig. 6.7b clearly improve the SINR, the effects on EIRP are not immediately apparent without further investigation. Since the total transmit power is the same for both the uniform and adaptive cases, changes in the array gain impact the EIRP. The array gain for both beamformers is plotted in Fig. 6.8b, and indicates 13.8 and 10.3 dBi for the uniform and adaptive cases, respectively. This noticeable 3.5-dB degradation is due in part to the small array size with limited degrees of freedom (DOF) for the beamformer, and represents one of the system-level tradeoffs that should be considered when deploying aperture-level IBFD arrays. The evaluation of the system using these beamforming coefficients and modulated signals is presented in the following section.

6.2.4 System Evaluation

An aperture-level IBFD array system is constructed using the RF Blockset circuit-envelope simulator in Simulink, where the model is comprised of components based on the measurements of the 8-element antipodal Vivaldi antenna and the front-end integrated with the single-stage PA. The model follows the diagram of Fig. 6.1, with J and K both set to 4. Additive white Gaussian noise (AWGN) was added to the transmit, observation and receive channels such that they had

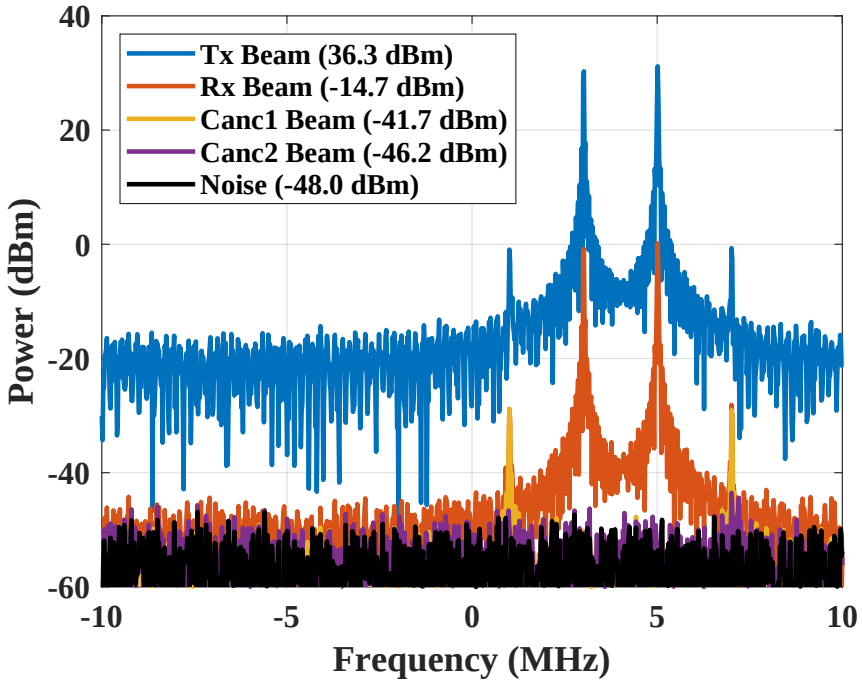


Figure 6.9: Evaluation of an 8-element aperture-level IBFD array with adaptive transmit beamforming for a two-tone transmit signal, highlighting the combined transmit beam, coupled receive beam, two cancellation methods, and the receive noise floor.

limited dynamic ranges of 45, 60 and 60 dB, respectively. Since the signal conditioning aspects of the additional hardware ($\boldsymbol{h_{tx}}$, $\boldsymbol{h_o}$, $\boldsymbol{h_{rx}}$) were not measured, they were modeled to provide unity gain and not introduce any further nonlinearities beyond those of the front-end and PA.

The initial input ($x[n]$) selected is a two-tone signal with a tone spacing of 2 MHz and a carrier frequency of 10 GHz, which allows the linear, nonlinear and noise aspects of the model to be investigated. Fig. 6.9 illustrates the baseband frequency-domain responses for the combined transmit ($\boldsymbol{tx}$), receive ($\boldsymbol{rx}$) and cancelled (y) beams, as well as indicates the receive noise floor for reference. The transmit beam is seen to have 36.3 dBm of EIRP, corresponding to the array gain of 10.3 dBi plus the total transmit power of 26.0 dBm, which is the summation of the individual transmit powers listed in Fig.6.7b. With the main tones at 3 and 5 MHz, the intermodulation products can clearly be seen at 1 and 6 MHz, demonstrating the nonlinearities of the PA and front-end being captured by the model.

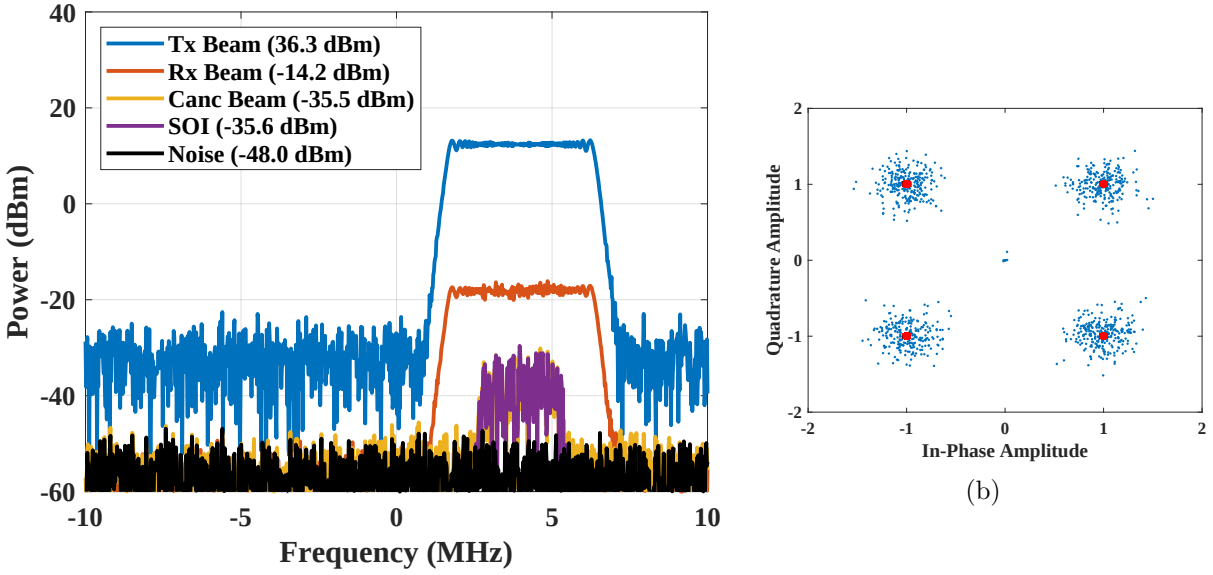
All of these signals coherently combine to create XI at the receiver input, and result in the receive beam having a total power of −14.7 dBm when the adaptive transmit beamforming is enabled. For this receive signal, two different methods of digital cancellation are investigated. In the first case (Canc1), the input to the digital filter was simply the ideal transmit input signal ($x[n]$), where Fig. 6.9 shows that the two main tones are effectively removed, but that the intermodulation tones remained, which limited the digital cancellation to 27 dB. The second method (Canc2) utilized the observed-transmit signal ($o[n]$) as the input to the canceller (depicted in Fig. 6.1), which resulted in the suppression of all of the transmit signal components, and highlights the need for the transmit observation channels. Fig. 6.9 illustrates the resulting signals with the XI digitally cancelled by 31.5 dB, which is 1.8 dB above the receive noise floor, and corresponds to a total transmit-receive isolation of 82.5 dB at the array level.

This EIRP-to-residual-noise isolation number, however, does not take into account the benefits of the directional receive array, namely the improvement the system sensitivity. For this purpose, another array-specific metric to consider is effective isotropic isolation (EII), which is defined as

$$\text{EII} = \frac{\text{EIRP}}{\text{EIS}} = \text{EIRP} \cdot \frac{G_{rx}}{P_{N_{rx}}} = \frac{P_{tx}}{P_{N_{rx}}} \cdot G_{tx} \cdot G_{rx}, \tag{6.12}$$

where $\text{EIS} = G_{rx}/P_{N_{rx}}$ and represents the effective isotropic sensitivity of the system, and G_{tx} and G_{rx} capture the transmit and receive antenna array gains, respectively [30]. For the two-tone signal considered, the EII of this system is equal to 96.3 dB (the 82.5 dB isolation plus the 13.8 dB receive array gain).

Following the two-tone signal, another input type is considered, namely a linear frequency modulated (LFM) chirp, configured as a single tone swept over a 5 MHz bandwidth, as shown at baseband in Fig. 6.10a for a carrier frequency of 10 GHz. The chirp power was adjusted so that the EIRP is the same as the two-tone scenario, and the coupled XI into the receive beam with the adaptive transmit beamformer is found to be a similar level at −14.2 dBm. This test case is unique because it also includes an SOI that was constructed as a communications signal



(a) (b)

Figure 6.10: Evaluation of an 8-element aperture-level IBFD array with adaptive transmit beamforming for a linear frequency modulated (LFM) chirp transmit signal and a receive signal-of-interest (SOI) with quadrature amplitude modulation (QAM), highlighting the (a) combined transmit beam; coupled receive beam; cancelled beam; nominal SOI; and the receive noise floor, and (b) constellation for the demodulated 4-QAM signal.

with quadrature amplitude modulation (QAM) and a modulation order of four (4-QAM), which is similar to quadrature phase-shift keying (QPSK). The digital cancellation step utilizes the transmit observation as its input and effectively removes the unwanted XI chirp, revealing the SOI, which is plotted before (purple) and after (yellow) cancellation in Fig. 6.10a. The final receiver output ($y[n]$) is demodulated and the resulting symbols are depicted in the constellation diagram of Fig. 6.10b. This image shows the four ideal symbols as red points at their in-phase and quadrature amplitude locations. The clusters of blue dots around these points represent the demodulated 4-QAM symbols with the addition of receiver noise. The average error vector magnitude (EVM) of this received SOI is $-14.4\,\text{dB}$ (compared to $-15.7\,\text{dB}$ without the chirp active), indicating that the IBFD operation of the array did not significantly degrade the signal quality of the communications link, which is critical for the multifunction applications highlighted in Chapter 1.

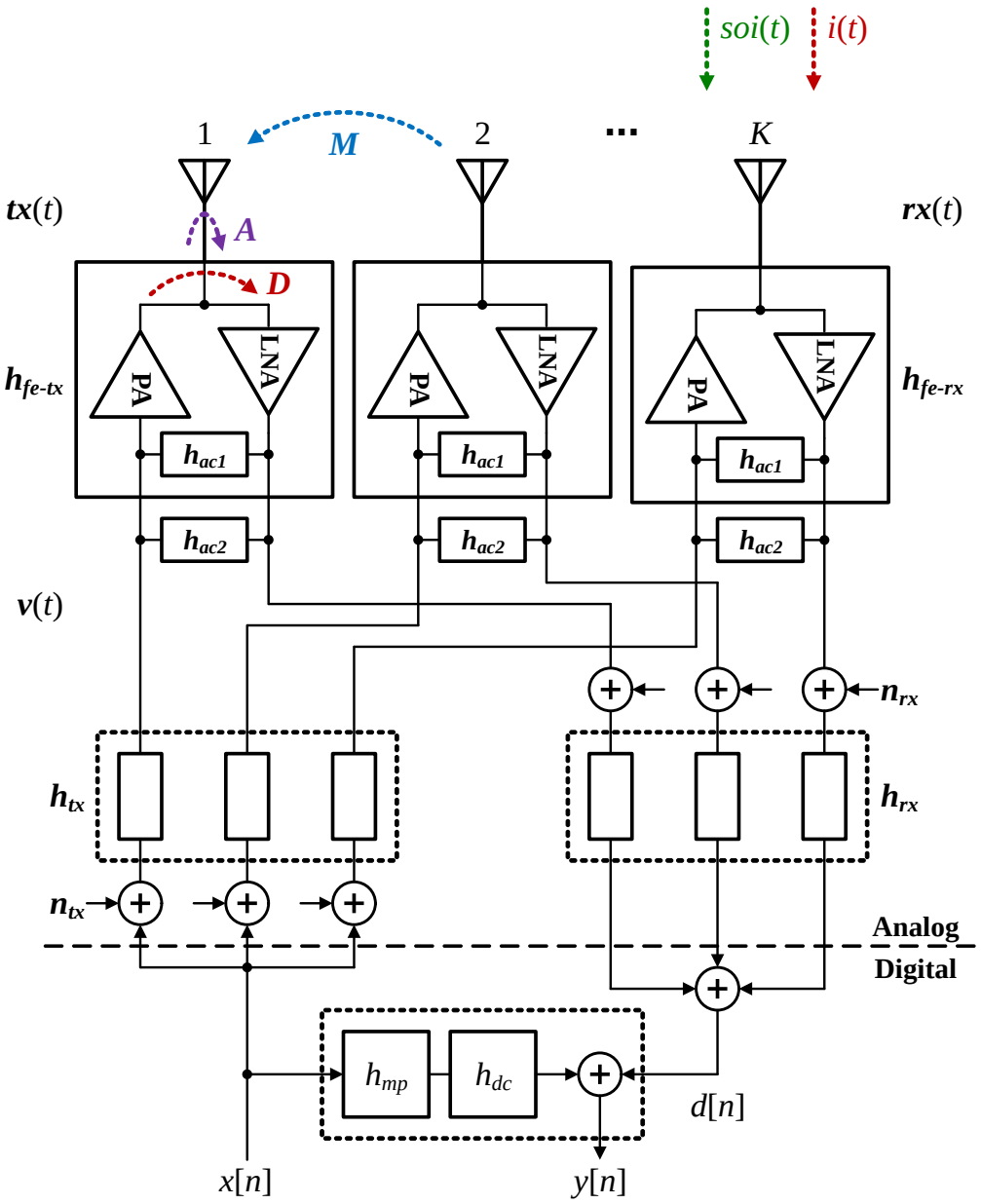


Figure 6.11: Signal model for an element-level IBFD array system evaluation with transmit input $x[n]$; mutual coupling matrix $\boldsymbol{M}$; signal-of-interest $soi(t)$; external interference $i(t)$; and combined receive output $y[n]$, where the RF/analog cancellers $\boldsymbol{h_{ac1}}$ and $\boldsymbol{h_{ac2}}$ as well as the digital canceller h_{dc} reduce the self-interference (D and A) and crosstalk interference (XI). Note that bold variables represent vectors and/or matrices.

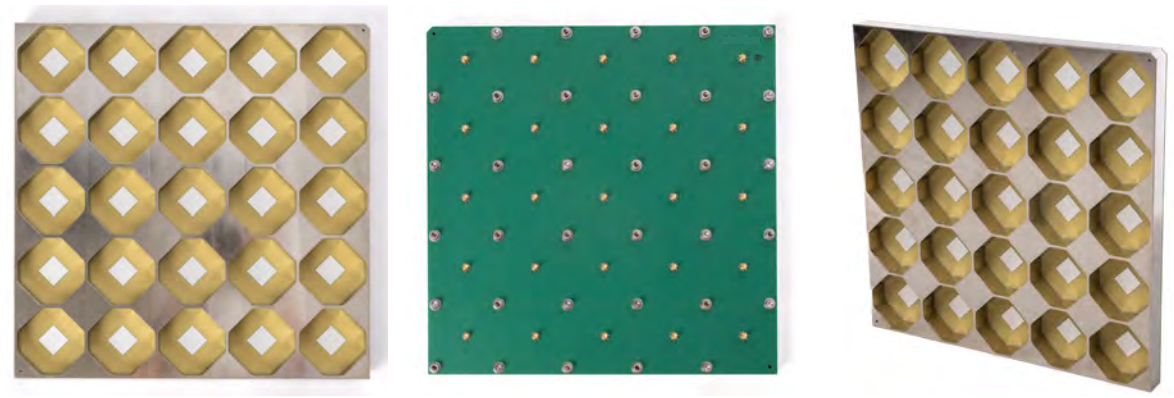
6.3 Element-Level IBFD Array

The signal model for an element-level IBFD array with K channels simultaneously transmitting and receiving is shown in Fig. 6.11. Similar to Fig. 6.1, components above the dashed

horizontal line are RF/analog in nature and those below refer to digital structures. The input signal is denoted as $x[n]$ in the bottom left corner with $E\left[|x[n]|^2\right] = 1$, where quantization and thermal noise ($\boldsymbol{n_{tx}}$) are added to the individual channels once transitioned into the analog domain. These signals travel through separate transmitters ($\boldsymbol{h_{tx}}$) before heading to the front-end circuitry, which differs significantly from what was used in the aperture-level case. Not only does this design integrate the PA, but it also must sufficiently suppress the self-interference (SI) internal to the element so that the LNA remains linear and the receiver operates at fully sensitivity. As discussed in Chapter 3, this SI is comprised of direct path and antenna reflection components, denoted only for the first element in the figure as D and A, respectively. The RF/analog canceller integrated into the front-end is represented by ($\boldsymbol{h_{ac1}}$) and attempts to mitigate the SI from D, while a second canceller ($\boldsymbol{h_{ac2}}$), located before the receiver input, tackles the SI generated by A. The XI between the elements is captured by the array mutual coupling matrix ($\boldsymbol{M}$), and can also be suppressed using these cancellers when the appropriate delays are configured.

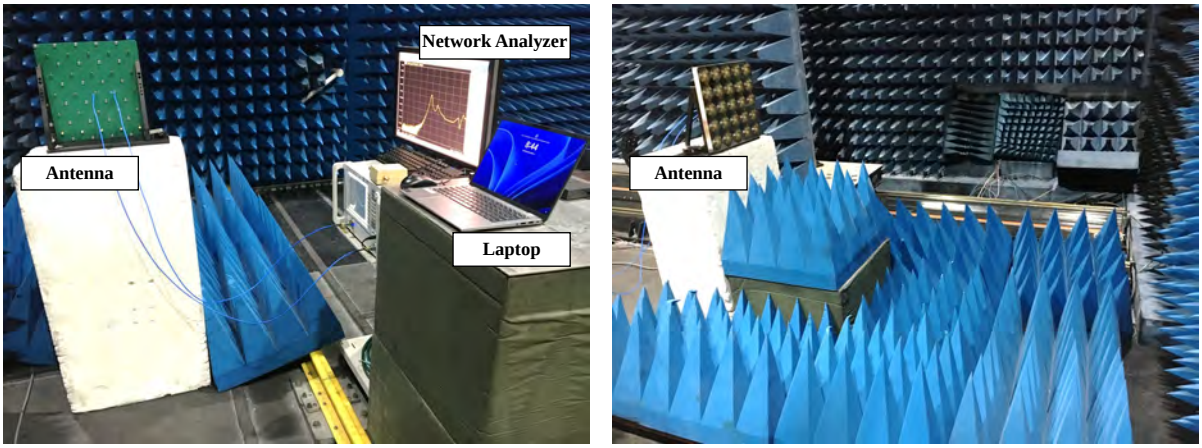
On the receive side, the antenna is seen to directly connect to an LNA, providing minimum noise figure, but requiring that the LNA handle the SI and XI power levels, which is less of a concern when employing GaN-based front-ends (as highlighted in Chapters 4 and 5). The two sets of RF/analog cancellers in each channel help ensure that the combined interference is below the receiver saturation level based on the cancellation requirements established in Chapter 3. For each receiver, noise ($\boldsymbol{n_{rx}}$) and the effects of individual hardware channels ($\boldsymbol{h_{rx}}$) are added before the signals are digitized for additional processing. Like before, a signal-of-interest ($soi(t)$) and external interference ($i(t)$) can also be factored in on the receive side.

The following sections present the reduced-coupling array utilized; the cancellation circuitry that can augment the front-ends covered in Chapters 4 and 5; the formulation of the theoretical cancellation framework using this signal model; and lastly, the outputs of the integrated array system assessed with different complex input signals.



(a) (b) (c)

Figure 6.12: Reduced-coupling array with 25 elements, highlighting the prototype photos with (a) front, (b) back and (c) isometric views.



(a) (b)

Figure 6.13: Measurement setup for the reduced-coupling array located in an anechoic chamber, highlighting the (a) equipment behind the array and (b) front radiating side.

6.3.1 Antenna Array

The antenna employed in this system is an array with 25 patch elements that are designed to operate near 3 GHz, where the simulation details are discussed in Chapter 3 and summarized in Fig. 3.11. Photos of the prototype are illustrated in Fig. 6.12 with front, back and isometric views shown. Fig. 6.12a depicts the radiating side where the rotated patches and coupling-reducing metal walls with chamfers are visible, Fig. 6.12b shows the back side with 25 SMA connectors and screws

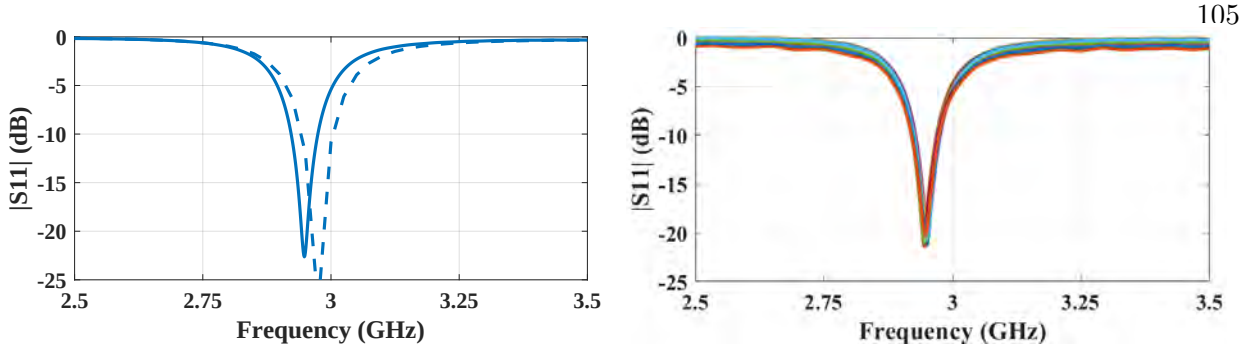


Figure 6.14: Measured |S11| for the reduced-coupling array prototype, illustrating the (a) comparison of measured (solid) and simulated (dashed) results for the center element, and (b) measurements for all the elements.

to attach the wall structure, and Fig. 6.12c gives a sense of the wall height. The measurement setup of this antenna mounted on a bracket and located in an anechoic chamber is visualized in Fig. 6.13. The antenna is located roughly 2 m from the absorber-covered wall, and an N5232A network analyzer from Agilent Technologies is utilized to record the s-parameters between each element and the center element of the array.

A comparison of the measured (solid) and simulated (dashed) |S11| for the center element (the others terminated using 50 Ω loads) is depicted in Fig. 6.14a. The plot indicates a slight downward shift in the resonance frequency due to fabrication tolerances, but is still within the acceptable range, and is seen to be well-matched. Fig. 6.14b displays the |S11| for all of the different elements with the others terminated, and demonstrates consistency across the array.

The critical coupling results are broken down based on the orientation and distance to the center element of the array, as presented in Chapter 3 and depicted in Fig. 3.4. Fig. 6.15a illustrates the coupling on the horizontal axis of the array for elements located to the left and right of the center (denoted H1) as well as two columns away in either direction (denoted H2). Similarly, Fig. 6.15b depicts the results for the vertical plane coupling. The data for the diagonal planes is further examined based on the orientation of the E- and H-planes, according to Fig. 3.11. The coupling levels from the first and second diagonal locations for the slant-left E-plane and slant-right

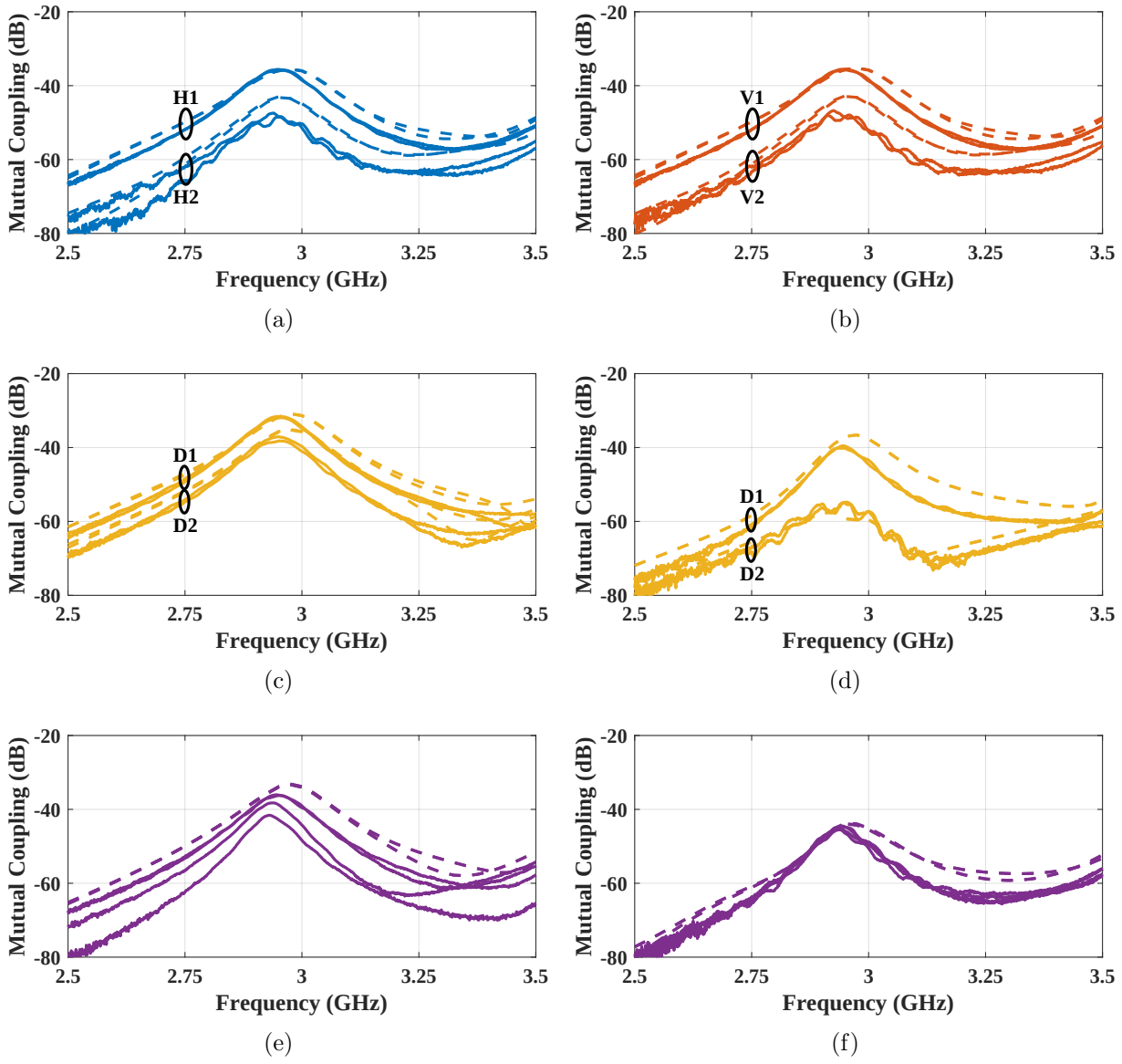


Figure 6.15: Measured mutual coupling from the center element for the 25-element reduced coupling array, comparing measured (solid) and simulated (dashed) results for different element locations, including (a) horizontal; (b) vertical; (c) diagonal E-plane; (d) diagonal H-plane; (e) off-diagonal E-plane; and (f) off-diagonal H-plane, as referenced in Fig. 3.4.

H-plane are plotted in Figs. 6.15c and 6.15d, respectively. Similarly, Figs. 6.15e and 6.15f illustrate the coupling from the off-diagonal locations, which all have the same distance to the center element. As expected, coupling from element locations further from the center exhibit lower values. All of these results show good agreement between the measured (solid) and simulated (dashed) levels, and

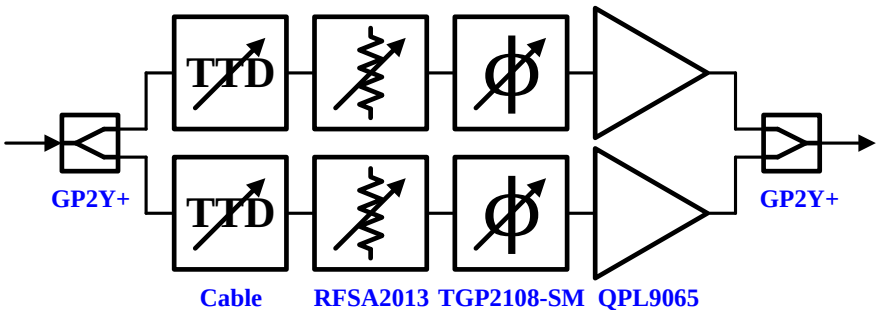


Figure 6.16: Diagram of the discrete two-tap canceller utilized for $\boldsymbol{h_{ac2}}$ in Fig. 6.11, where each tap is comprised of an adjustable true-time delay (TTD); voltage-variable attenuator; digital phase shifter; and amplifier with part numbers listed.

demonstrate a maximum coupling of −31.6 dB, which agrees with the values listed in Table 3.2, and can be used to establish the XI levels for the front-end discussed next.

6.3.2 Front-End

The front-end incorporated into this array system is based on the active circulator with a two-tap integrated canceller, as described in Chapter 5. Matching the depiction of Fig. 6.11, this GaN MMIC includes PA, LNA and canceller ($\boldsymbol{h_{ac1}}$) circuits. The cancellation internal to the front-end is augmented with an additional two-tap canceller ($\boldsymbol{h_{ac2}}$) designed using discrete components, where the block diagram is illustrated in Fig. 6.16. This image shows the canceller input being divided among the two taps using a GP2Y+ splitter from Mini-Circuits. Following that, true-time delay (TTD) units are implemented using cables, where different lengths offer the ability to make static adjustments to the individual delays. For each tap, the RFSA2013 voltage-variable attenuator from Qorvo gives a continuously tunable 30-dB attenuation range, and the TGP2108-SM digital phase shifter (also from Qorvo) provides 360° of phase coverage in roughly 5° steps. In order to compensate for the losses of these passive components, QPL9065 high-linearity amplifiers from Qorvo are included to boost the signal before it is combined at the output. The minimum step sizes and overall range limitations for these parts are added to accurately model the canceller tuning discussed in the following section.

6.3.3 Signal Processing

With the different aspects of Fig. 6.11 already higlighted, this section derives the equations that represent the transmit output, receive input and receive output signals within the array. The signals before the front-end represent an intermediary point in the transmit chains, and can be described as

$$\boldsymbol{v}(t) = (x(t) + \boldsymbol{n_{tx}}(t))\, \boldsymbol{h_{tx}}, \tag{6.13}$$

which is used to feed into the canceller stages, and will be discussed when analyzing the receivers. This intermediate signal is amplified by the PA in the front-end, such that the final transmit output can be formulated as

$$\boldsymbol{tx}(t) = \boldsymbol{v}(t)\, \boldsymbol{h_{fe\text{–}tx}}. \tag{6.14}$$

While some IBFD systems utilize this final output for cancellation, this array architecture leverages $\boldsymbol{v}(t)$ to avoid impacting the transmit efficiency and receive noise figure, as highlighted in Chapter 4.

As previously mentioned, the receivers within this array must contend with two types of SI (D and A) as well as XI ($\boldsymbol{M}$), where their combination can be represented at the input using

$$\boldsymbol{rx}(t) = (D + A + \boldsymbol{M})\, \boldsymbol{tx}(t) + soi(t) + i(t), \tag{6.15}$$

which also includes notional SOI and external interference signals. The RF/analog cancellers that mitigate the SI and XI are captured in the digital representation of the receiver output,

$$d[n] = \sum_{k=1}^{K} (rx_k(t)\, h_{fe\text{–}rx_k} + v_k(t)(h_{ac1_k} + h_{ac2_k}) + n_{rx_k}(t))\, h_{rx_k}, \tag{6.16}$$

which assumes that the K channels are summed with a uniform weighting, but other combinations could be considered (possibly in parallel) to steer the receive beam to different angles.

Since the nonlinearities of the front-end are built into the model and those effects are not present in the canceller input signal ($\boldsymbol{v}(t)$), the receiver output ($d[n]$) contains nonlinear terms that do not exist in the transmitter input ($x[n]$). In order to improve the efficacy of the final cancellation step, the input to the FIR-based digital canceller (h_{dc}) needs to be modified to include

these nonlinear aspects of the transmit signal. These terms can be generated using nonlinear device/channel modeling, for which memory polynomial (MP) models have been demonstrated to accurately characterize the nonlinearities of PAs by themselves [62, 103] as well as complete IBFD transceivers [5, 6]. The baseband equivalent MP model is represented by

$$h_{mp}[n] = \sum_{p=1}^{P} \sum_{m=0}^{M} c_{p,m}\, x[n-m]\, |x[n-m]|^{p-1}, \tag{6.17}$$

where P and M denote the polynomial order and memory depth, respectively, and $c_{p,m}$ captures the estimated coefficients for each term [145].

With this model, the remaining linear and nonlinear components of the transmit signal ($x[n]$) present in the combined receive output ($d[n]$) can be suppressed by appropriately tuning the weights of h_{dc}, yielding the final receiver output,

$$y[n] = x[n]\, h_{mp}\, h_{dc} + d[n]. \tag{6.18}$$

These equations along with the model framework are used to establish and evaluate the performance of a realistic element-level IBFD array system, which is discussed next.

6.3.4 System Evaluation

From the antenna prototype depicted in Fig. 6.12, a 5-element linear array is created using the elements along the middle row where the others are terminated with 50 Ω loads. Behind these five elements, models of the aforementioned front-end and discrete cancellers are added to assess the SI and XI power levels as well as the overall array performance. Similar to the aperture-level IBFD array, this system is initially characterized using a two-tone input that allows the nonlinear distortion terms to be clearly distinguished. Before engaging all the array elements, however, the interference levels within a single element are analyzed, as seen in Fig. 6.17a for the center element with the others not transmitting. For a carrier frequency near 3 GHz, this plot illustrates the transmit output power set to 10 dBm and the resultant AR and DP components at the output of the front-end, which represents the internal SI of each element. While the DP level is suppressed

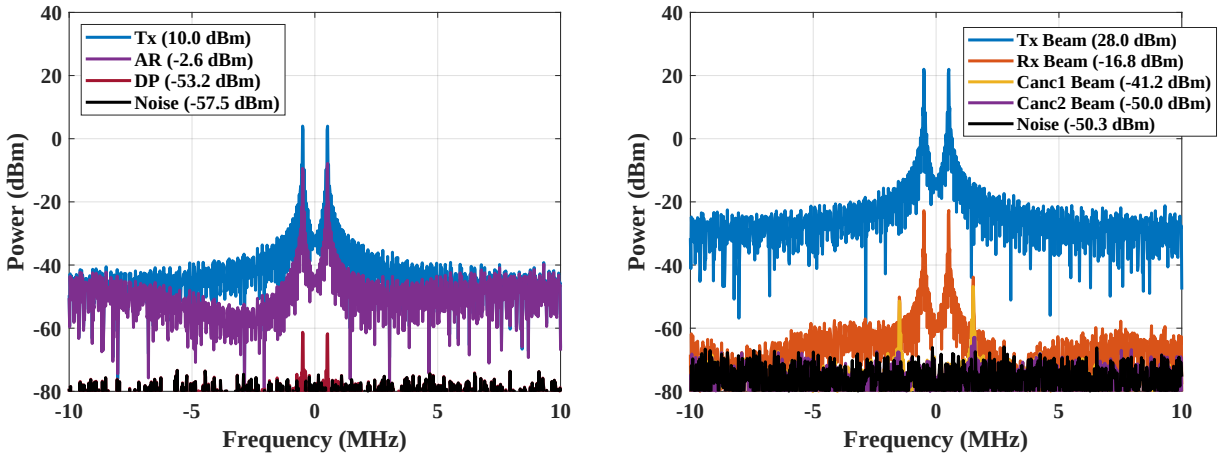
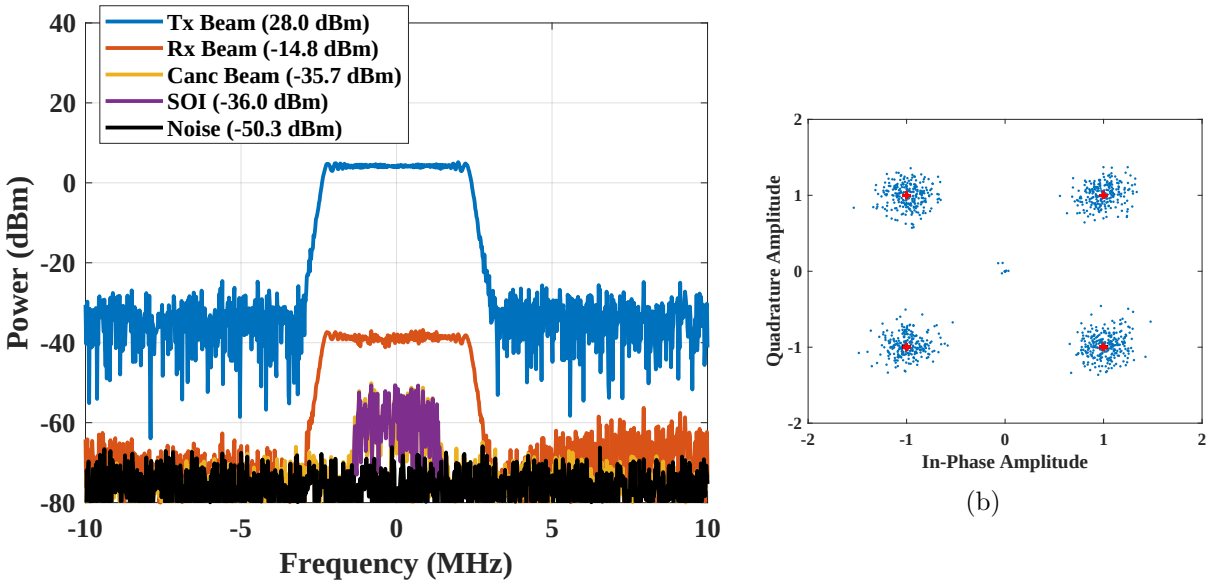


Figure 6.17: Evaluation of a 5-element element-level IBFD array, highlighting the (a) single-element transmit, antenna reflection (AR) and direct path (DP) power levels, and (b) combined transmit beam, coupled receive beam, two cancellation methods, and the receive noise floor.

by 50 dB below the front-end input ($P_v = -3.2$ dBm), the AR signal that is based on the antenna match and front-end is seen to be -2.6 dBm, which is above the receiver saturation level, determined to be -20 dBm in Chapter 3. This demonstrates the need for additional cancellation (i.e., $\boldsymbol{h_{ac2}}$) behind the front-ends of each channel.

A transmit beam can be formed using this two-tone signal when all five elements are enabled, and in Fig. 6.17b is seen to generate an EIRP of 28 dBm, which arises from the combination of the 5-element array gain of 11 dBi and the total transmit power of 17 dBm. The receive beam illustrates the uniformly-weighted summation of the five receive channels after both RF/analog cancellation steps, representing $d[n]$ in Fig. 6.11. While the composite power is seen to be -16.8 dBm, the discrete cancellers suppress the SI and XI below the receiver saturation level of -20 dBm for each channel, allowing the signals to be digitized for further processing. In this signal, intermodulation distortion products are visible on either side of the main receive tones, where the first digital cancellation (Canc1 beam) utilizes the ideal transmit signal ($x[n]$) as its input and is seen to suppress the main tones, but not the intermodulation ones. The second digital cancellation (Canc2 beam) employs the memory polynomial block (h_{mp}) to synthesize the transmit nonlinearities and



(a) (b)

Figure 6.18: Evaluation of a 5-element element-level IBFD array for a linear frequency modulated (LFM) chirp transmit signal and a receive signal-of-interest (SOI) with quadrature amplitude modulation (QAM), highlighting the (a) combined transmit beam; coupled receive beam; cancelled beam; nominal SOI; and the receive noise floor, and (b) constellation for the demodulated 4-QAM signal.

effectively minimize them in addition to the main tones. This suppresses the transmit beam to within 0.3 dB of the receiver noise floor, yielding a total system isolation of 78 dB and EII of 89 dB.

After the two-tone investigation, an LFM chirp signal with a 5 MHz bandwidth is utilized as the input, which is seen in Fig. 6.18a. The individual elements were again set to output 10 dBm, which resulted in the transmit beam having an EIRP of 28 dBm. The composite receive beam is cancelled to reveal a SOI that is configured as a communications signal with a 4-QAM digital modulation scheme. The cancellation processes are seen to minimally affect the decoding of the communications data, as evidenced in the constellation diagram of Fig. 6.18b, which produced an average EVM of -15.1 dB (compared to -15.2 dB without the chirp active). Overall, these evaluation results were similar to the aperture-level case previously discussed, and indicate that both IBFD array types are capable of suppressing SI and XI, and performing multiple simultaneous functions.

Table 6.1: Summary of System-Level Array Losses

Systems Losses (dB)		**Aperture-Level**	**Element-Level**	**Half-Duplex**
Subarray	Tx Power	3	0	0
	Tx Gain	3	0	0
	Rx Gain	3	0	0
Beamforming	Tx Beam	3.5	0	0
	Rx Beam	0	0	0
Front-End	Tx Path	1	4	1
	Rx Path	1	4	1
	Totals	14.5	8	2

6.4 Chapter Conclusion

This chapter presents the integration of both aperture- and element-level IBFD array systems that are created using measured data from antenna arrays and front-end circuits. The former utilizes an 8-element linear array based on antipodal-Vivaldi elements that operate at 10 GHz, and the latter employs a reduced-coupling 5-element linear array with patches that operate around 3 GHz. These systems are excited with two-tone and LFM signal inputs, and demonstrate the ability to effectively suppress the resulting SI and XI down to the receiver noise floor in all cases. Additionally, SOIs are recovered and successfully demodulated despite the persistent array transmissions, which demonstrates the desired IBFD and multifunction capabilities.

In order to quantify the system-level impact of incorporating IBFD capabilities into these arrays, three loss mechanisms can be considered, namely those related to the subarray division, beamforming and front-end circuity. Table 6.1 summarizes these losses for the two array architectures presented, and compares them to a traditional half-duplex system. As highlighted in Fig. 2.3, the aperture-level configuration is seen to suffer from creating transmit and receive subarrays, which decreases the gains of each as well as the total transmit power. The element-level version, on the other hand, is solely impacted by losses in the front-end, specifically the antenna interface, where values from Fig. 5.2 are used for the comparison. Overall, the table indicates that these aperture-

and element-level IBFD array configurations exhibit 12.5 and 6 dB more loss than the half-duplex reference, respectively. While this indicates that there is an opportunity to further improve these systems, the novel multifunction capability that they have been demonstrated to introduce cannot be understated. Some of the material presented in this chapter is currently in publication review [70].

Chapter 7

Conclusion

Phased array systems are being incorporated into devices that support wireless communications for both ground- and satellite-based links, commercial and defense radar, and military electronic warfare strategies, among others. Recent research has focused on the intersection of these different applications and their contention for the same spectral and hardware resources. The creation of simultaneous-multifunction wireless systems offers the opportunity to integrate traditionally "stove-piped" solutions and leverage one application to enhance the performance of another (e.g., smart base stations can use radar to track users and improve their communications links). One of the major challenges of integrating multiple functions is managing their competing need to access the same frequency channels and time slots, which can be overcome by incorporating in-band full-duplex (IBFD) operation into the designs, as discussed in this thesis.

7.1 Thesis Summary

This thesis demonstrates the ability of IBFD technology to enable the simultaneous multifunction operation of phased array systems, and presents the architectural options, critical enabling technologies and system-level integration capabilities for advanced designs.

Chapters 2 and 3 focus on the system architectures and antenna aspects that influence the requirements for IBFD arrays. In Chapter 2, state-of-the-art IBFD phased array implementations that can be used to create simultaneous-multifunction systems are highlighted. Various IBFD array architectures are presented with a focus on aperture- and element-level approaches. The

former divides the aperture into transmit and receive subarrays, and utilizes digitally-enabled self-interference (SI) cancellation processes to create isolation between them. The latter allows the same antenna in each element to simultaneously transmit and receive, and requires an RF/analog-based cancellation scheme to reduce interference before digitization and further suppression. A survey of measured IBFD array prototypes as well as their results and limitations are also discussed. In Chapter 3, a generic system architecture is presented, on which the key aspects of both aperture- and element-level IBFD arrays are considered. Both array types must address SI that arises from direct path (DP) and/or antenna reflection (AR) within some or all of the elements as well as crosstalk interference (XI) from neighboring elements within the array in order to avoid receiver saturation. This XI is a function of the mutual coupling between elements, where several different methods of reducing it are analyzed using a 7-element linear array, which aided the subsequent design of a reduced-coupling 25-element two-dimensional array. This helped form the basis for mutual coupling levels on which an IBFD system can be analyzed, and the cancellation requirements determined for the front-ends of both aperture- and element-level IBFD arrays.

Chapters 4 and 5 present two active circulators with integrated tunable cancellers having one and two canceller taps, both fabricated using the WIN Semiconductors NP12-01 0.12 μm GaN process. In Chapter 4, the first active circulator front-end with a single integrated tunable canceller tap is discussed, along with an overview and theoretical formulation of the design architecture. Details on the individual amplifier and phase shifter components are highlighted, where measurement results of the standalone test circuits demonstrate good agreement with simulated expectations. The performance of the complete chip is also evaluated and provides the desired gain in the transmit and receive paths as well as successfully suppresses the SI at the receiver by 50 dB, which is tunable over the 2.8–3.2 GHz range. In Chapter 5, a second active circulator front-end that builds upon the aforementioned architecture is examined. In addition to including a second integrated canceller tap, this design also incorporates improvements to the power dividers (including the antenna interface), amplifier design and tunable phase shifters. It similarly demonstrates gain in the transmit and receive paths, and provides tunable transmit-to-receive isolation of more than 50 dB

over 2.5–3.1 GHz, which represent the first known instances of these capabilities for a GaN-based active circulator. This front-end is also evaluated using a linear frequency-modulated (LFM) chirp waveform that is common in multifunction radar systems, and with the addition of a subsequent digital cancellation process, produces a total SI suppression of 70 dB.

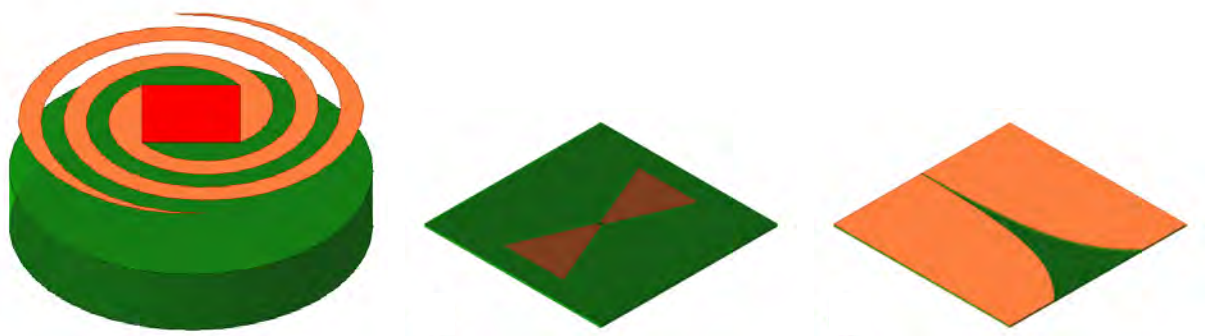
Finally, Chapter 6 presents the integration of both aperture- and element-level IBFD array systems that are created using measured data from antenna arrays and front-end circuits. The former utilizes an 8-element linear array based on antipodal-Vivaldi elements that operate at 10 GHz, and the latter employs a reduced-coupling 5-element linear array with patches that operate around 3 GHz. These systems are excited with two-tone and LFM signal inputs, and demonstrate the ability to effectively suppress the resulting SI and XI down to the receiver noise floor in all cases. Additionally, signals-of-interest are recovered and successfully demodulated despite the persistent array transmissions, which demonstrates the desired IBFD and multifunction capabilities. The system-level impact of incorporating IBFD operation into these arrays is also considered.

7.2 Future Work

Multifunction phased arrays can benefit from additional research within each of the three main topics discussed throughout this thesis, namely antennas arrays, fronts-end circuits and system-integration efforts, with suggested work detailed in the following sections.

7.2.1 Antennas

Due to the inherent narrowband nature of the patch-based unit cells considered for the antenna elements in Chapter 3, the ensuing array prototype provided reduced-coupling performance over a narrow bandwidth, as seen in the measurement results presented in Chapter 6. Two possible areas to investigate in order to extend the antenna performance are: analyzing different wideband unit cells, and taking additional advantage of the E- and H-plane coupling differences within the array. As seen in Fig. 7.1, wideband unit cells may include spiral, bow-tie and Vivaldi elements, where the latter is the one utilized in the linear array discussed in Chapter 6. While not a focus for



(a) (b) (c)

Figure 7.1: Wideband array unit cells, highlighting (a) cavity-backed spiral, (b) bow-tie and (c) Vivaldi element options.

that array design, careful attention must be given to the coupling between the elements for both aperture- and element-level IBFD array configurations. For example, tightly-coupled dipole arrays operate over wide bandwidths, but the fundamental coupling between the elements is unavoidable.

For the E- and H-plane coupling studied in Chapter 3, it was demonstrated that the H-field decays more rapidly with distance than the E-field for patch-based arrays. This effect could be analyzed for other unit cell types, and potentially leveraged to reduce their coupling, especially for linear arrays that exhibit coupling in only one plane. With this in mind, the mutual coupling reduction techniques presented in Chapter 3 were considered individually, where the combination of multiple approaches might offer unforeseen benefits. While the element-to-element coupling is a major challenge, additional requirements could be considered when designing practical systems. These include the thermal aspects of any active components (e.g., front-end MMICs) mounted to the back of the array, the desire to keep the manufacturing inexpensive (possibly utilizing printed circuit boards or additive manufacturing) and providing dual-polarization capabilities that may be necessary for some applications, like weather sensing.

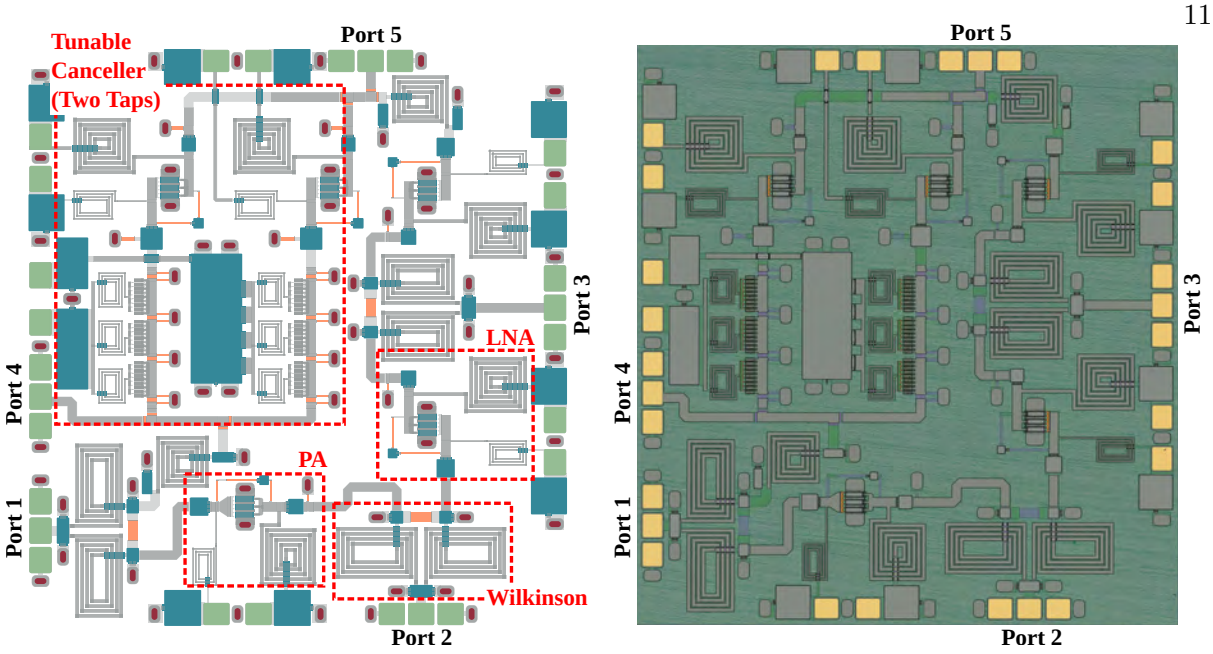
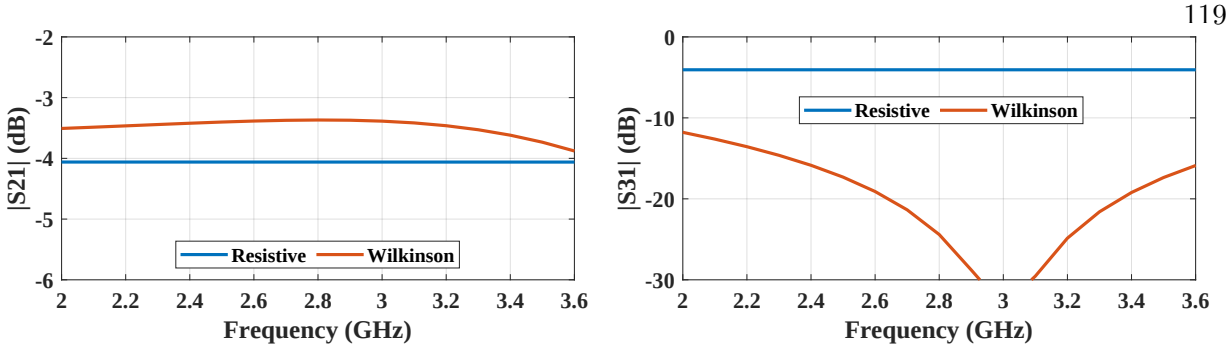


Figure 7.2: Active circulator with two-tap tunable canceller and Wilkinson-based antenna interface, illustrating the (a) chip layout with the PA, LNA and Wilkinson sections highlighted, and (b) MMIC photo with matching ports.

7.2.2 Front-Ends

For the front-end circuits presented in Chapters 4 and 5, several different improvements can be considered based on the previous findings. First, instead of using similar architectures for each amplifier, the power amplifier (PA) and low-noise amplifier (LNA) designs can be optimized to meet their divergent performance goals. The former could be tailored to enhance the transmit power output and power added efficiency (PAE), and the latter could be designed to reduce the receive noise figure and possible extend its power handling capability.

The connection of these devices on chip defines the antenna interface, which was implemented using capacitive- and resistive-based dividers for the designs presented in Chapters 4 and 5, respectively. As noted at the end of Chapter 6, the insertion losses of this aspect of the front-end limit its performance compared to traditional half-duplex systems. One possible alternative is the use of a discrete-based Wilkinson power divider, as seen in the next iteration of the front-end layout



(a) (b)

Figure 7.3: Simulated results comparing the (a) |S21| and (b) |S31| for resistive and discrete-based Wilkinson power dividers.

and MMIC photo of Fig. 7.2. While this design includes several different enhancements over those discussed in Chapters 4 and 5, the most significant is the antenna interface incorporating a Wilkinson structure. Fig. 7.3 illustrates the simulated gain (|S21|) and isolation (|S31|) of resistive and Wilkinson dividers, where the latter is seen to offer improvements in both the loss and isolation. Beyond this, further research could be conducted to focus on novel approaches that allow for the connection of the PA and LNA to the antenna, possibly leveraging orthogonal circuit modes.

In order to improve the SI suppression performance of the integrated canceller, it would be ideal if the canceller input is provided after the PA and the canceller output is injected into the receive path before the LNA. This would allow the canceller to capture the nonlinear distortion and noise of the PA, and suppress it before the LNA input, which would reduce the power handling requirements of the LNA. While this feature would improve the cancellation performance, it would create a more complex antenna interface and possibly make it more difficult to reduce its insertion loss. Additionally, within the canceller section itself, the ability of adjust the phase slope and/or add true-time delay on chip could be considered to enhance the bandwidth of the cancellation.

7.2.3 Systems

While Chapter 6 presents promising results demonstrating the capabilities of aperture- and element-level IBFD arrays, the system-level array integration effort can be expanded to not only

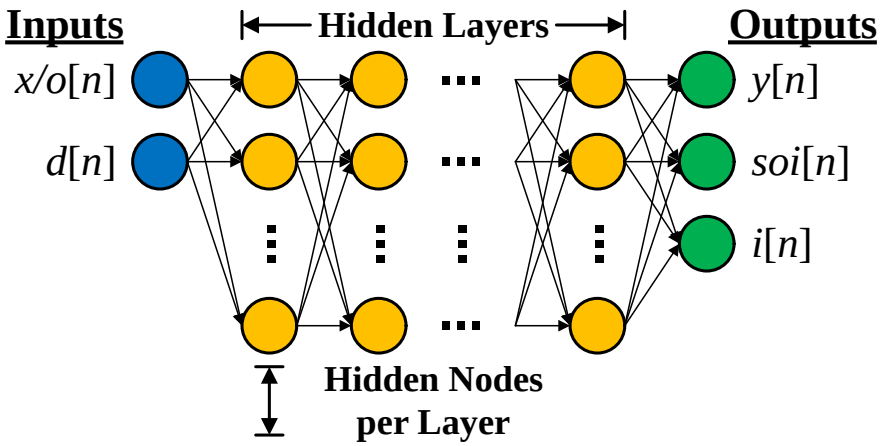


Figure 7.4: Diagram of a generic neural network that can utilize inputs $d[n]$ and $o[n]$ for aperture-level, or $x[n]$ for element-level, IBFD arrays with varying numbers of hidden layers and hidden nodes per layer to derive the outputs $y[n]$, $soi[n]$, $i[n]$.

transition into hardware, but also explore other array configurations. Connecting antenna elements to physical front-ends and data converters would capture the hardware-related time and temperature effects not represented in the model, and would lead to an increase in the maturity level of the technology. Other array considerations may include the transmission and reception of different signal types and power levels. The use of diverse transmit signals could create unique XI signals through their coherent combination, and may impose additional constrains on the beamforming and digital cancellation processes, potentially increasing the necessary computational requirements.

Additionally, different signal-of-interest (SOI) types with varying degrees of correlation to the transmit signal could be considered. When the SOI is highly correlated with the transmission, other means of separating it from the SI and XI may become necessary, including the use of time-of-arrival information. Furthermore, while external interference was represented in the model derivations discussed in Chapter 6, it was not present in the simulations. These other unwanted signals could be added to the environment to evaluate the ability of a receive beamformer to not only create near-field nulls, but also far-field ones in the aperture-level IBFD array. For the element-level IBFD case, this extra interference could be mitigated with additional digital cancellation or might require the incorporation of receive beamforming. For both array types, the digital separation of

the SOI from SI, XI and external interference could benefit from the use of artificial intelligence and machine learning (AI/ML). As depicted in Fig 7.4, this could come from a framework, such as a feedforward neural network (with various hidden layer and node depths) that trains on the characteristics of the desired signals and suppresses others, which could potentially improve the computation time of the digital signal processing.

7.3 Summary of Contributions

This thesis' contributions to research on multifunction phased arrays, including IBFD antenna arrays, GaN-based front-end MMICs and system-level integration aspects, are summarized below:

Chapter 2: A detailed description of the various IBFD array architectures, a dissection of existing aperture- and element-level approaches, and a summary of state-of-the-art prototype performance. Results are reported in [77] and [78].

Chapter 3: A framework upon which the interference components that drive the performance of IBFD arrays can be considered. The derivation of IBFD front-end requirements based on array mutual coupling, including the design of a 25-element reduced-coupling patch array. Partial results are reported in [68].

Chapter 4: The design of a novel active circulator front-end MMIC with a one-tap integrated canceller, fabricated in the WIN Semiconductors NP12-01 0.12 μm GaN process. Results are currently in press [72].

Chapter 5: The design of an improved active circulator front-end MMIC that incorporates a second canceller tap, also fabricated in the WIN Semiconductors NP12-01 0.12 μm GaN process, and additionally evaluated in a radar system context. Results are currently in press [72].

Chapter 6: The unique system-level integration of both aperture- and element-level IBFD arrays using measured antenna and front-end data, demonstrating multifunction operation. Partial results are reported in [58] and are currently in publication review [70].

Bibliography

[1] Wael M. Abdel-Wahab, H. Al-Saedi, M. Raeiszadeh, E. Alian, G. Chen, A. Ehsandar, N. Ghafarian, H. El-Sawaf, A. Palizban, M. R. Nezhad-Ahmadi, and S. Safavi-Naeini. A modular architecture for low cost phased array antenna system for Ka-band mobile satellite communication. In 36th International Communications Satellite Systems Conference (ICSSC 2018), pages 1–5, 2018.

[2] B. L. Allen, J. L.; Diamond. Mutual Coupling in Array Antennas. MIT Lincoln Laboratory Technical Report, (424):1–65, 1966.

[3] Muhammad Amjad, Fayaz Akhtar, Mubashir Husain Rehmani, Martin Reisslein, and Tariq Umer. Full-Duplex Communication in Cognitive Radio Networks: A Survey. IEEE Communications Surveys & Tutorials, 19(4):2158–2191, 2017.

[4] Ehsan Aryafar and Alireza Keshavarz-Haddad. PAFD: Phased Array Full-Duplex. In IEEE INFOCOM 2018 - IEEE Conference on Computer Communications, pages 261–269, 2018.

[5] Andrew C. M. Austin, Orion Afisiadis, and Andreas Burg. Digital predistortion of hardware impairments for full-duplex transceivers. In 2017 IEEE Global Conference on Signal and Information Processing (GlobalSIP), pages 878–882, 2017.

[6] Andrew C. M. Austin, Alexios Balatsoukas-Stimming, and Andreas Burg. Digital predistortion of power amplifier non-linearities for full-duplex transceivers. In 2016 IEEE 17th International Workshop on Signal Processing Advances in Wireless Communications (SPAWC), pages 1–5, 2016.

[7] Mustafa Ayebe, Rob Maaskant, Marianna Ivashina, Johan Malmström, Sten E. Gunnarson, Henrik Holter, Simon Westergren, and Erik Johansson. In-Band Full-Duplex Antenna Beamforming and Synchronization for Self-Interference Mitigation: Multi-Tile RFSoC Testbed Design and Deployment. In 2025 19th European Conference on Antennas and Propagation (EuCAP), pages 1–5, 2025.

[8] Mahmood Baraani Dastjerdi, Sanket Jain, Negar Reiskarimian, Arun Natarajan, and Harish Krishnaswamy. Analysis and Design of a Full-Duplex Two-Element MIMO Circulator-Receiver With High TX Power Handling Exploiting MIMO RF and Shared-Delay Baseband Self-Interference Cancellation. IEEE Journal of Solid-State Circuits, 54(12):3525–3540, 2019.

[9] Carlos Baquero Barneto, Sahan Damith Liyanaarachchi, Mikko Heino, Taneli Riihonen, and Mikko Valkama. Full Duplex Radio/Radar Technology: The Enabler for Advanced Joint Communication and Sensing. IEEE Wireless Communications, 28(1):82–88, 2021.

[10] M. Berg, T. Hackbarth, B.E. Maile, S. Kosslowski, J. Dickmann, D. Kother, B. Hopf, and H.L. Hartnagel. Active circulator MMIC in CPW technology using quarter micron InAlAs/InGaAs/InP HFETs. In Proceedings of 8th International Conference on Indium Phosphide and Related Materials, pages 68–71, 1996.

[11] Dinesh Bharadia and Sachin Katti. Full Duplex MIMO Radios. In 2014 Conf. on Netw. Syst. Des. and Implementation (USENIX), NSDI'14, pages 359–372, Berkeley, CA, USA, 2014. USENIX Association.

[12] T. S. Bird. Mutual Coupling Between Antennas. John Wiley Sons, Ltd, 2021.

[13] D. W. Bliss, P. A. Parker, and A. R. Margetts. Simultaneous Transmission and Reception for Improved Wireless Network Performance. In 2007 IEEE/SP 14th Workshop on Statistical Signal Processing, pages 478–482, 2007.

[14] G. Carchon and B. Nanwelaers. Power and noise limitations of active circulators. IEEE Transactions on Microwave Theory and Techniques, 48(2):316–319, 2000.

[15] Tingjun Chen, Mahmood Baraani Dastjerdi, Harish Krishnaswamy, and Gil Zussman. Wideband Full-Duplex Phased Array With Joint Transmit and Receive Beamforming: Optimization and Rate Gains. IEEE/ACM Transactions on Networking, 29(4):1591–1604, 2021.

[16] Tingjun Chen, Sasank Garikapati, Aravind Nagulu, Aditya Gaonkar, Manav Kohli, Igor Kadota, Harish Krishnaswamy, and Gil Zussman. A Survey and Quantitative Evaluation of Integrated Circuit-Based Antenna Interfaces and Self-Interference Cancellers for Full-Duplex. IEEE Open Journal of the Communications Society, 2:1753–1776, 2021.

[17] Zhu Chen, Hongbin Li, Guolong Cui, and Muralidhar Rangaswamy. Adaptive Transmit and Receive Beamforming for Interference Mitigation. IEEE Signal Processing Letters, 21(2):235–239, 2014.

[18] Boon Leng Cheong, Redmond Kelley, Robert D. Palmer, Yan Zhang, Mark Yeary, and Tian-You Yu. PX-1000: A Solid-State Polarimetric X-Band Weather Radar and Time–Frequency Multiplexed Waveform for Blind Range Mitigation. IEEE Transactions on Instrumentation and Measurement, 62(11):3064–3072, 2013.

[19] Siu K. Cheung, Timothy P. Halloran, William H. Weedon, and Craig P. Caldwell. MMIC-Based Quadrature Hybrid Quasi-Circulators for Simultaneous Transmit and Receive. IEEE Transactions on Microwave Theory and Techniques, 58(3):489–497, 2010.

[20] Jung Il Choi, Mayank Jain, Kannan Srinivasan, Phil Levis, and Sachin Katti. Achieving Single Channel, Full Duplex Wireless Communication. In Proc. of the Annu. Int. Conf. on Mobile Comput. and Netw., MobiCom '10, pages 1–12, New York, NY, USA, 2010. ACM.

[21] Kae Won Choi, Sa Il Hwang, Arif Abdul Aziz, Hyeon Ho Jang, Ji Su Kim, Dong Soo Kang, and Dong In Kim. Simultaneous Wireless Information and Power Transfer (SWIPT) for Internet of Things: Novel Receiver Design and Experimental Validation. IEEE Internet of Things Journal, 7(4):2996–3012, 2020.

[22] M. David Conway, David Du Russel, Alexander Morris, and Christine Parry. Multifunction phased array radar advanced technology demonstrator nearfield test results. In 2018 IEEE Radar Conference (RadarConf18), pages 1412–1415, 2018.

[23] M.J. Cryan and P.S. Hall. An integrated active circulator antenna. IEEE Microwave and Guided Wave Letters, 7(7):190–191, 1997.

[24] Ian T. Cummings, Jonathan P. Doane, Timothy J. Schulz, and Timothy C. Havens. Aperture-Level Simultaneous Transmit and Receive With Digital Phased Arrays. IEEE Transactions on Signal Processing, 68:1243–1258, 2020.

[25] Ian T. Cummings, Timothy J. Schulz, Timothy C. Havens, and Jonathan P. Doane. Neural Networks for Real-Time Adaptive Beamforming in Simultaneous Transmit and Receive Digital Phased Arrays: Student Submission. In 2019 IEEE International Symposium on Phased Array System & Technology (PAST), pages 1–8, 2019.

[26] Paige Danielson, Megan Robinson, Gregor Lasser, and Zoya Popovic. GaAs MMIC Interferometer for Broadband Interference Suppression. In 2022 17th European Microwave Integrated Circuits Conference (EuMIC), pages 17–20, 2022.

[27] Arnima Das, Maitreyi Ray Kanjilal, Moumita Mukherjee, and Arpita Santra. Review on Wide Band Gap Semiconductor. In 2022 IEEE International Conference of Electron Devices Society Kolkata Chapter (EDKCON), pages 586–591, 2022.

[28] Mahmood Baraani Dastjerdi, Negar Reiskarimian, Tingjun Chen, Gil Zussman, and Harish Krishnaswamy. Full Duplex Circulator-Receiver Phased Array Employing Self-Interference Cancellation via Beamforming. In 2018 IEEE Radio Frequency Integrated Circuits Symposium (RFIC), pages 108–111, 2018.

[29] Jonathan Doane and Richard Scott Teal. Data Distribution for Scalable on-Array Processing. In 2024 IEEE International Symposium on Antennas and Propagation and INC/USNC-URSI Radio Science Meeting (AP-S/INC-USNC-URSI), pages 2605–2606, 2024.

[30] Jonathan P. Doane. Isolation Metrics for Single-Channel and Multi-Channel Simultaneous Transmit and Receive Systems. In 2020 IEEE International Symposium on Antennas and Propagation and North American Radio Science Meeting, pages 1761–1762, 2020.

[31] Jonathan P. Doane, Kenneth E. Kolodziej, and Bradley T. Perry. Simultaneous transmit and receive with digital phased arrays. In 2016 IEEE International Symposium on Phased Array Systems and Technology (PAST), pages 1–6, 2016.

[32] Jonathan P. Doane, Kenneth E. Kolodziej, and Bradley T. Perry. Simultaneous transmit and receive performance of an 8-channel digital phased array. In 2017 IEEE International Symposium on Antennas and Propagation and USNC/URSI National Radio Science Meeting, pages 1043–1044, 2017.

[33] Jonathan P. Doane, Kenneth E. Kolodziej, and Bradley T. Perry. Analog Self-Interference Cancellation Networks for STAR Phased Arrays. In 2021 IEEE-APS Topical Conference on Antennas and Propagation in Wireless Communications (APWC), pages 189–190, 2021.

[34] Evan Everett, Achaleshwar Sahai, and Ashutosh Sabharwal. Passive Self-Interference Suppression for Full-Duplex Infrastructure Nodes. IEEE Transactions on Wireless Communications, 13(2):680–694, 2014.

[35] Evan Everett, Clayton Shepard, Lin Zhong, and Ashutosh Sabharwal. SoftNull: Many-Antenna Full-Duplex Wireless via Digital Beamforming. IEEE Transactions on Wireless Communications, 15(12):8077–8092, 2016.

[36] Rory Fagan, Frank C. Robey, and Luke Miller. Phased array radar cost reduction through the use of commercial RF systems on a chip. In 2018 IEEE Radar Conference (RadarConf18), pages 0935–0939, 2018.

[37] Hongji Fan, Yiqiu Liang, Weiheng Chen, Wanjing Huang, Zhaoyi Wang, Zhiqiang Yu, Jianyi Zhou, and Wei Hong. A Wideband, High Isolation, Shared-Aperture MIMO IBFD Front End With CMS Balun and Fewer Multitap Cancellers. IEEE Transactions on Microwave Theory and Techniques, 73(9):6918–6930, 2025.

[38] A. Gasmi, B. Huyart, E. Bergeault, and L. Jallet. Noise and power optimization of a MMIC quasi-circulator. IEEE Transactions on Microwave Theory and Techniques, 45(9):1572–1577, 1997.

[39] Nimrod Ginzberg, Dror Regev, Rani Keren, Shimi Shilo, Doron Ezri, and Emanuel Cohen. A Four-Element 5–6-GHz CMOS Quadrature Balanced Full-Duplex MIMO Transmitter With Wideband Digital Interference Cancellation. IEEE Microwave and Wireless Components Letters, 32(2):173–176, 2022.

[40] Yating Guo, Tianwei Deng, Jiongpei Xu, Xiaoxia Huang, and Xizhang Wei. A Wideband Phased Array RF Front End With Coupling-Capture Channels for Full-Duplex Wireless Backhaul. IEEE Transactions on Microwave Theory and Techniques, 73(10):8258–8274, 2025.

[41] S. Hara, T. Tokumitsu, and M. Aikawa. Novel unilateral circuits for MMIC circulators. IEEE Transactions on Microwave Theory and Techniques, 38(10):1399–1406, 1990.

[42] Matthew Harger, M. David Conway, Henry Thomas, Mark Weber, John Bendickson, Alex Morris, Ted Hoffmann, and Nathan Van Schaick. Fully Digital Phased Array Development for Next Generation Weather Radar. In 2021 IEEE Radar Conference (RadarConf21), pages 1–6, 2021.

[43] Matthew Harger, M. David Conway, Henry Thomas, Mark Weber, Alex Morris, and Ted Hoffmann. An Update on the Fully Digital Phased Array Development for Next Generation Weather Radar. In 2022 IEEE Radar Conference (RadarConf22), pages 1–6, 2022.

[44] Mehedi Hasan, Sujan Chowdhury, and Hasan U. Zaman. Active quasi circulator: Comprehensive review and performance comparison. Engineering Reports, 6(6):1–22, 2024.

[45] S. Haykin. Cognitive radio: brain-empowered wireless communications. IEEE Journal on Selected Areas in Communications, 23(2):201–220, 2005.

[46] Guolong He, Xin Gao, Liangliang Sun, and Rentian Zhang. A Review of Multibeam Phased Array Antennas as LEO Satellite Constellation Ground Station. IEEE Access, 9:147142–147154, 2021.

[47] Mikko Heino, Carlos Baquero Barneto, Taneli Riihonen, and Mikko Valkama. Design of Phased Array Architectures for Full-Duplex Joint Communications and Sensing. In 2021 15th European Conference on Antennas and Propagation (EuCAP), pages 1–5, 2021.

[48] C. Hemmi, R.T. Dover, A. Vespa, and Mun-Won Fenton. Advanced Shared Aperture Program (ASAP) array design. In Proceedings of International Symposium on Phased Array Systems and Technology, pages 278–282, 1996.

[49] J. Herd, D. Carlson, S. Duffy, M. Weber, G. Brigham, M. Rachlin, D. Cursio, C. Liss, and C. Weigand. Multifunction Phased Array Radar (MPAR) for aircraft and weather surveillance. In 2010 IEEE Radar Conference, pages 945–948, 2010.

[50] Jeffrey S. Herd and M. David Conway. The Evolution to Modern Phased Array Architectures. Proceedings of the IEEE, 104(3):519–529, 2016.

[51] Naoki Honma, Masakuni Tsunezawa, Yoshiyuki Yamamoto, and Yuta Kashino. Realizing in-band full-duplex MIMO with feasible RF-chain: Key challenges. In 2017 IEEE Conference on Antenna Measurements & Applications (CAMA), pages 284–287, 2017.

[52] Dujuan Hu, Xizhang Wei, Mingcong Xie, and Yanqun Tang. A Sparse Design for Aperture-Level Simultaneous Transmit and Receive Arrays. Electronics, 11(20), 2022.

[53] Dujuan Hu, Li Yang, Xiujun Zhang, Yan Xue, Xizhang Wei, and Tairan Lin. Comparative Analysis of Digital Self-Interference Cancellation Methods for Simultaneous Transmit and Receive Arrays. Electronics, 13(15), 2024.

[54] Sunmin Jang, Jaehun Jeong, Rundao Lu, and Michael P. Flynn. A 16-Element 4-Beam 1 GHz IF 100 MHz Bandwidth Interleaved Bit Stream Digital Beamformer in 40 nm CMOS. IEEE Journal of Solid-State Circuits, 53(5):1302–1312, 2018.

[55] R. Jedlicka, M. Poe, and K. Carver. Measured mutual coupling between microstrip antennas. IEEE Transactions on Antennas and Propagation, 29(1):147–149, 1981.

[56] Seth Johannes, Kenneth E. Kolodziej, Reyes Lucero, and Zoya Popović. Integrated GaN Front-End for Aperture-Level In-Band Full-Duplex Arrays. IEEE Transactions on Microwave Theory and Techniques, in review.

[57] Seth Johannes, Kenneth E. Kolodziej, and Zoya Popovic. GaN MMIC RF Switches for In-Band Full-Duplex Phased Array Calibration. In 2022 IEEE 22nd Annual Wireless and Microwave Technology Conference (WAMICON), pages 1–4, 2022.

[58] Seth Johannes, Kenneth E. Kolodziej, and Zoya Popović. Antipodal Vivaldi Array for Reconfigurable Aperture-Level In-Band Full-Duplex. In 2024 IEEE International Symposium on Phased Array Systems and Technology (ARRAY), pages 1–5, 2024.

[59] Hyungsik Ju and Rui Zhang. Optimal resource allocation in full-duplex wireless-powered communication network. IEEE Transactions on Communications, 62(10):3528–3540, 2014.

[60] Seyed Ali Keivaan, Pascal Burasa, and Ke Wu. Virtual Receiver Matrix and Combinatory Analog Operations for Future Multifunction Reconfigurable Sensing and Communication Wireless Systems. IEEE Transactions on Microwave Theory and Techniques, 71(1):424–433, 2023.

[61] Stéphane Kemkemian and Myriam Nouvel-Fiani. Toward common radar & EW multifunction active arrays. In 2010 IEEE International Symposium on Phased Array Systems and Technology, pages 777–784, 2010.

[62] J. Kim and K. Konstantinou. Digital predistortion of wideband signals based on power amplifier model with memory. Electronics Letters, 37(23):1–2, Nov 08 2001.

[63] Kenneth E. Kolodziej, editor. In-Band Full-Duplex Wireless Systems Handbook. Artech House, Norwood, MA, 2021.

[64] Kenneth E. Kolodziej, Glenn A. Brigham, Matthew A. Harger, Brian A. Janice, Adrienne I. Sands, Richard Scott Teal, Louis Turek, Pierre-François W. Wolfe, Jonathan P. Doane, and Bradley T. Perry. Phased Array Architecture Enabling Scalable Integrated Sensing and Communication. In 2023 IEEE Radar Conference (RadarConf23), pages 1–5, 2023.

[65] Kenneth E. Kolodziej, Glenn A. Brigham, Matthew A. Harger, Brian A. Janice, Adrienne I. Sands, Ian Weiner, Pierre-Francois W. Wolfe, Jonathan P. Doane, and Bradley T. Perry. Scalable Array Technologies for Converged-RF Applications. In 2022 IEEE Radar Conference (RadarConf22), pages 1–5, 2022.

[66] Kenneth E. Kolodziej, Aidan U. Cookson, and Bradley T. Perry. Adaptive Learning Rate Tuning Algorithm for RF Self-Interference Cancellation. IEEE Transactions on Microwave Theory and Techniques, 69(3):1740–1751, 2021.

[67] Kenneth E. Kolodziej, Jonathan P. Doane, Bradley T. Perry, and Jeffrey S. Herd. Adaptive Beamforming for Multi-Function In-Band Full-Duplex Applications. IEEE Wireless Communications, 28(1):28–35, 2021.

[68] Kenneth E. Kolodziej, Dejan Filipović, and Zoya Popović. Mutual Coupling Study of Full-Duplex Arrays. In 2025 United States National Committee of URSI National Radio Science Meeting (USNC-URSI NRSM), pages 85–86, 2025.

[69] Kenneth E. Kolodziej, Brian A. Janice, Adrienne I. Sands, and Bradley T. Perry. Scalable In-Band Full-Duplex Phased Arrays: Complexity Reduction and Distributed Processing. IEEE Journal on Selected Areas in Communications, pages 1–13, 2023.

[70] Kenneth E. Kolodziej, Seth Johannes, Reyes Lucero, and Zoya Popović. Integrated GaN Front-End within an Aperture-Level IBFD Array for ISAC Applications. In 2026 IEEE MTT-S International Microwave Symposium, pages 1–4, 2026.

[71] Kenneth E. Kolodziej, Laila Marzall, and Zoya Popović. In-Band Full-Duplex Front-End GaN MMIC for Phased Arrays. In 2024 IEEE International Symposium on Phased Array Systems and Technology (ARRAY), pages 1–5, 2024.

[72] Kenneth E. Kolodziej, Laila Marzall, and Zoya Popović. Active Circulator GaN Front-Ends with Integrated Tunable Cancellers for Multifunction Phased Arrays. IEEE Transactions on Microwave Theory and Techniques, in press.

[73] Kenneth E. Kolodziej, Joseph G. McMichael, and Bradley T. Perry. Multitap RF Canceller for In-Band Full-Duplex Wireless Communications. IEEE Transactions on Wireless Communications, 15(6):4321–4334, 2016.

[74] Kenneth E. Kolodziej, Bradley T. Perry, and Jeffrey S. Herd. Simultaneous Transmit and Receive (STAR) system architecture using multiple analog cancellation layers. In 2015 IEEE MTT-S International Microwave Symposium, pages 1–4, 2015.

[75] Kenneth E. Kolodziej, Bradley T. Perry, and Jeffrey S. Herd. In-Band Full-Duplex Technology: Techniques and Systems Survey. IEEE Transactions on Microwave Theory and Techniques, 67(7):3025–3041, 2019.

[76] Kenneth E. Kolodziej, Bradley T. Perry, and Jeffrey S. Herd. In-Band Full-Duplex Operation in High-Speed Mobile Environments: Not So Fast! IEEE Microwave Magazine, 22(12):60–72, 2021.

[77] Kenneth E. Kolodziej and Zoya Popović. In-Band Full-Duplex Array Architectures and Performance Survey. In 2024 United States National Committee of URSI National Radio Science Meeting (USNC-URSI NRSM), pages 102–103, 2024.

[78] Kenneth E. Kolodziej and Zoya Popović. Simultaneous-Multifunction Phased Arrays: Enabled by In-Band Full-Duplex Technology. IEEE Microwave Magazine, 25(4):44–63, 2024.

[79] Kenneth E. Kolodziej, Siva Yegnanarayanan, and Bradley T. Perry. Photonic-Enabled RF Canceller for Wideband In-Band Full-Duplex Wireless Systems. IEEE Transactions on Microwave Theory and Techniques, 67(5):2076–2086, 2019.

[80] Ahmed Kord, Mykhailo Tymchenko, Dimitrios L. Sounas, Harish Krishnaswamy, and Andrea Alù. CMOS Integrated Magnetless Circulators Based on Spatiotemporal Modulation Angular-Momentum Biasing. IEEE Transactions on Microwave Theory and Techniques, 67(7):2649–2662, 2019.

[81] Dani Korpi, Lauri Anttila, and Mikko Valkama. Reference receiver based digital self-interference cancellation in MIMO full-duplex transceivers. In 2014 IEEE Globecom Workshops (GC Wkshps), pages 1001–1007, 2014.

[82] D. Kother, B. Hopf, T. Sporkmann, I. Wolff, and S. Koblowski. Active CPW MMIC Circulator for the 40 GHZ Band. In 1994 24th European Microwave Conference, volume 1, pages 542–547, 1994.

[83] Amit Kumar, Abdul Quaiyum Ansari, Binod Kumar Kanaujia, Jugul Kishor, and Ladislau Matekovits. A review on different techniques of mutual coupling reduction between elements of any MIMO antenna. Part 1: DGSs and parasitic structures. Radio Science, 56(3):1–25, 2021.

[84] Amit Kumar, Abdul Quaiyum Ansari, Binod Kumar Kanaujia, Jugul Kishor, and Ladislau Matekovits. A review on different techniques of mutual coupling reduction between elements of any MIMO antenna. Part 2: Metamaterials and many more. Radio Science, 56(3):1–22, 2021.

[85] Lei Lei, Norshahida Saba, and Sirajudeen Gulam Razul. A Multichannel Self-Interference Cancellation Prototyping System. In 2019 IEEE 2nd 5G World Forum (5GWF), pages 427–432, 2019.

[86] Ao Liu, Ian P. Roberts, Taneli Riihonen, and Weixing Sheng. Analog Beamforming for In-Band Full-Duplex Phased Arrays With Quantized Phase Shifters Under a Per-Antenna Received Power Constraint. IEEE Signal Processing Letters, 31:1585–1589, 2024.

[87] Ao Liu, Weixing Sheng, and Taneli Riihonen. Per-Antenna Self-Interference Cancellation Beamforming Design for Digital Phased Array. IEEE Signal Processing Letters, 29:2442–2446, 2022.

[88] Fan Liu, Christos Masouros, Athina P. Petropulu, Hugh Griffiths, and Lajos Hanzo. Joint Radar and Communication Design: Applications, State-of-the-Art, and the Road Ahead. IEEE Transactions on Communications, 68(6):3834–3862, 2020.

[89] Yiliang Liu, Hsiao-Hwa Chen, and Liangmin Wang. Physical Layer Security for Next Generation Wireless Networks: Theories, Technologies, and Challenges. IEEE Communications Surveys & Tutorials, 19(1):347–376, 2017.

[90] Kevin S. Lorenz, Joel Goodman, Michelle Mcbeth, Matthew B. Mckeon, and David J. Parrett. A Real-Time Wideband Subband LMS Algorithm for Full-Duplex Communications. IEEE Access, 10:32566–32573, 2022.

[91] Rundao Lu, Sunmin Jang, Yun Hao, and Michael P. Flynn. A 77dB-SFDR Multi-Phase-Sampling 16-Element Digital Beamformer with 64 4GS/s 100MHz-BW Continuous-Time Band-Pass $\Delta\Sigma$ ADCs. In 2019 IEEE Radio Frequency Integrated Circuits Symposium (RFIC), pages 223–226, 2019.

[92] Reyes Lucero, Connor Nogales, and Zoya Popović. Efficiency Enhancement by Sizing Device Periphery for Supply-Modulated Power Amplifiers. In 2024 IEEE Wireless and Microwave Technology Conference (WAMICON), pages 1–4, 2024.

[93] Mattia Maggi, Syrine Hidri, Loïc Marnat, Mauro Ettorre, Gerardo Orozco, Marc Margalef-Rovira, Christophe Gaquière, and Kamel Haddadi. Millimeter-Wave Phased Arrays and Over-the-Air Characterization for 5G and Beyond: Overview on 5G mm-Wave Phased Arrays and OTA Characterization. IEEE Microwave Magazine, 23(5):67–83, 2022.

[94] James C. Martin, Robert Brodersen, and John Wawrzynek. Receiver Adaptive Beamforming and Interference of Indoor Environments in mmWave. In 2018 IEEE 29th Annual International Symposium on Personal, Indoor and Mobile Radio Communications (PIMRC), pages 1–7, 2018.

[95] Laila Marzall and Zoya Popović. An X-Band Quasi-Circulator GaAs MMIC. In 2019 IEEE International Conference on Microwaves, Antennas, Communications and Electronic Systems (COMCAS), pages 1–4, 2019.

[96] Laila Marzall and Zoya. Popović. Tunable microwave circulator, US provisional patent application 63/466,623, May 2023.

[97] Laila Marzall, Megan Robinson, Paige Danielson, Amy Robinson, Negar Ehsan, and Zoya Popović. Active and Passive Components for Broadband Transmit Phased Arrays: Broadband Transmit Front-End Components. IEEE Microwave Magazine, 23(2):56–74, 2022.

[98] Laila Marzall, Shane Verploegh, Tommaso Cappello, Michael Roberg, and Zoya Popović. Active MMIC Circulator Performance in a Phased-Array-Like Environment. In 2020 50th European Microwave Conference (EuMC), pages 1186–1189, 2021.

[99] Laila Marzall, Shane Verploegh, Tommaso Cappello, Michael Roberg, and Zoya Popović. Active MMIC Circulator Performance in a Phased-Array-Like Environment. In 2020 50th European Microwave Conference (EuMC), pages 1186–1189, 2021.

[100] Randall M. Mealey. A Method for Calculating Error Probabilities in a Radar Communication System. IEEE Transactions on Space Electronics and Telemetry, 9(2):37–42, 1963.

[101] Jaber Moghaddasi and Ke Wu. Multifunction, Multiband, and Multimode Wireless Receivers: A Path Toward the Future. IEEE Microwave Magazine, 21(12):104–125, 2020.

[102] Peter W. Moo and David J. DiFilippo. Multifunction RF Systems for Naval Platforms. Sensors, 18(7), 2018.

[103] D.R. Morgan, Z. Ma, J. Kim, M.G. Zierdt, and J. Pastalan. A Generalized Memory Polynomial Model for Digital Predistortion of RF Power Amplifiers. IEEE Transactions on Signal Processing, 54(10):3852–3860, 2006.

[104] Steve W. Y. Mung and Wing Shing Chan. Novel Active Quasi-Circulator With Phase Compensation Technique. IEEE Microwave and Wireless Components Letters, 18(12):800–802, 2008.

[105] Steve W. Y. Mung and Wing Shing Chan. Self-equalization technique for distributed quasi-circulator. Microwave and Optical Technology Letters, 51(1):182–184, 2009.

[106] Steve W. Y. Mung and Wing Shing Chan. Active Three-Way Circulator Using Transistor Feedback Network. IEEE Microwave and Wireless Components Letters, 27(5):476–478, 2017.

[107] Steve W.Y. Mung and Wing Shing Chan. The Challenge of Active Circulators: Design and Optimization in Future Wireless Communication. IEEE Microwave Magazine, 20(7):55–66, 2019.

[108] S.W.Y. Mung and W.S. Chan. Wideband active quasi-circulator with tunable isolation enhancement. The Journal of Engineering, 2014:83–85(2), March 2014.

[109] Aravind Nagulu, Negar Reiskarimian, Tingjun Chen, Sasank Garikapati, Igor Kadota, Tolga Dinc, Sastry Lakshmi Garimella, Manav Kohli, Alon Simon Levin, Gil Zussman, and Harish Krishnaswamy. Doubling Down on Wireless Capacity: A Review of Integrated Circuits, Systems, and Networks for Full Duplex. Proceedings of the IEEE, 112(5):405–432, 2024.

[110] A. Navarrini, A. Melis, G. Comoretto, T. Pisanu, R. Nesti, P. Marongiu, P. Ortu, P. Maxia, A. Ladu, H. Ghobadi, R. Concu, G. Angius, A. Cabras, L. Schirru, P. Di Ninni, M. Belluso, and S. Billotta. Architecture of C-band Phased Array Feed with RFSoC digital beamformer. In 2022 3rd URSI Atlantic and Asia Pacific Radio Science Meeting (AT-AP-RASC), pages 1–3, 2022.

[111] A. Ohlsson, V. Gonzalez-Posadas, and D. Segovia-Vargas. Active Integrated Circulating Antenna based on Non-Reciprocal Active Phase Shifters. In The Second European Conference on Antennas and Propagation, EuCAP 2007, pages 1–5, 2007.

[112] A. Ouacha, A. Fredlund, J. Andersson, H. Hindsefelt, V. Rinaldi, and C. Scattoni. SE-IT joint M-AESA program: Overview and status. In Proceedings of the Fourth European Conference on Antennas and Propagation, pages 1–5, 2010.

[113] Mirko Palomba, Andrea Bentini, Diego Palombini, Walter Ciccognani, and Ernesto Limiti. A novel hybrid active quasi-circulator for L-band applications. In 2012 19th International Conference on Microwaves, Radar Wireless Communications, volume 1, pages 41–44, 2012.

[114] Nial J. Peters, Colin P. Horne, Amin D. Amiri, Piers Beasley, and Matthew A. Ritchie. Modular Multi-Channel RFSoC System Expansion and Array Design. In 2023 IEEE Radar Conference (RadarConf23), pages 1–4, 2023.

[115] Tharindu D. Ponnimbaduge Perera, Dushantha Nalin K. Jayakody, Shree Krishna Sharma, Symeon Chatzinotas, and Jun Li. Simultaneous Wireless Information and Power Transfer (SWIPT): Recent Advances and Future Challenges. IEEE Communications Surveys & Tutorials, 20(1):264–302, 2018.

[116] D. Pozar. Input impedance and mutual coupling of rectangular microstrip antennas. IEEE Transactions on Antennas and Propagation, 30(6):1191–1196, 1982.

[117] Negar Reiskarimian, Aravind Nagulu, Tolga Dinc, and Harish Krishnaswamy. Nonreciprocal Electronic Devices: A Hypothesis Turned Into Reality. IEEE Microwave Magazine, 20(4):94–111, 2019.

[118] Taneli Riihonen, Dani Korpi, Olli Rantula, Heikki Rantanen, Tapio Saarelainen, and Mikko Valkama. Inband Full-Duplex Radio Transceivers: A Paradigm Shift in Tactical Communications and Electronic Warfare? IEEE Communications Magazine, 55(10):30–36, 2017.

[119] Taneli Riihonen, Dani Korpi, Matias Turunen, and Mikko Valkama. Full-duplex radio technology for simultaneously detecting and preventing improvised explosive device activation. In 2018 International Conference on Military Communications and Information Systems (ICMCIS), pages 1–4, 2018.

[120] Ian P. Roberts, Jeffrey G. Andrews, Hardik B. Jain, and Sriram Vishwanath. Millimeter-Wave Full Duplex Radios: New Challenges and Techniques. IEEE Wireless Communications, 28(1):36–43, 2021.

[121] Megan C Robinson, Zoya Popović, and Gregor Lasser. Linear broadband interference suppression circuit based on GaN monolithic microwave integrated circuits. IET circuits, devices & systems /, 17(4), 2023.

[122] Anthony Romano, Timothy Sonnenberg, Laila Marzall, and Zoya Popovic. V- Through W-Band GaN Active Circulator. In 2023 18th European Microwave Integrated Circuits Conference (EuMIC), pages 1–4, 2023.

[123] C.E. Saavedra and Y. Zheng. Active quasi-circulator realisation with gain elements and slow-wave couplers. IET Microwaves, Antennas Propagation, 1:1020–1023, 2007.

[124] A. Sabharwal, P. Schniter, D. Guo, D. W. Bliss, S. Rangarajan, and R. Wichman. In-Band Full-Duplex Wireless: Challenges and Opportunities. IEEE Journal on Selected Areas in Communications, 32(9):1637–1652, 2014.

[125] Aman Samaiyar, Dong-Chan Son, Mohamed A. Elmansouri, and Dejan S. Filipovic. Simultaneous Transmit and Receive with Shared-Aperture Arrays. In 2020 International Applied Computational Electromagnetics Society Symposium (ACES), pages 1–2, 2020.

[126] David Schvartzman, Robert D. Palmer, Matthew Herndon, and Mark B. Yeary. Enhanced Weather Surveillance Capabilities With Multiple Simultaneous Transmit Beams. IEEE Transactions on Radar Systems, 3:272–289, 2025.

[127] Tanzeela Shakeel, Shanzay Gul, Shahista Habib, and Ateeqa Naseer. A Systematic Literature Review on Cognitive Radio Networks. In 2021 International Conference on Innovative Computing (ICIC), pages 1–11, 2021.

[128] S.K. Sharma and J.C.S. Chieh. Multifunctional Antennas and Arrays for Wireless Communication Systems. John Wiley Sons, Ltd, 2021.

[129] Chengzhe Shi, Wensheng Pan, Ying Shen, and Shihai Shao. Robust Transmit Beamforming for Self-Interference Cancellation in STAR Phased Array Systems. IEEE Signal Processing Letters, 29:2622–2626, 2022.

[130] Chengzhe Shi, Wensheng Pan, Ying Shen, and Shihai Shao. Transmit Beamforming Self-Interference Cancellation Design and Experiment for STAR Phased Array. In 2024 IEEE Globecom Workshops (GC Wkshps), pages 1–6, 2024.

[131] Shih-Chieh Shin, Jhih-Yu Huang, Kun-You Lin, and Huei Wang. A 1.5–9.6 GHz Monolithic Active Quasi-Circulator in 0.18 μm CMOS Technology. IEEE Microwave and Wireless Components Letters, 18(12):797–799, 2008.

[132] Pratiksha Shukla, Yuanzhang Xiao, Magdy F. Iskander, and Zhengqing Yun. Advanced Base Station Concept for Wireless Connectivity in Rural Areas. In 2020 IEEE International Symposium on Antennas and Propagation and North American Radio Science Meeting, pages 641–642, 2020.

[133] Dimitrios Siafarikas and John L. Volakis. Toward Direct RF Sampling: Implications for Digital Communications. IEEE Microwave Magazine, 21(9):43–52, 2020.

[134] Hema Singh, H. L. Sneha, and R. M. Jha. Mutual Coupling in Phased Arrays: A Review. International Journal of Antennas and Propagation, 2013(1):348123, 2013.

[135] M.I. Skolnik. Radar Handbook, Third Edition. McGraw-Hill Education, 2008.

[136] Besma Smida, Risto Wichman, Kenneth E. Kolodziej, Himal A. Suraweera, Taneli Riihonen, and Ashutosh Sabharwal. In-Band Full-Duplex: The Physical Layer. Proceedings of the IEEE, pages 1–30, 2024.

[137] Trevor Snow, Caleb Fulton, and William J. Chappell. Transmit–Receive Duplexing Using Digital Beamforming System to Cancel Self-Interference. IEEE Transactions on Microwave Theory and Techniques, 59(12):3494–3503, 2011.

[138] D.-C. Son, A. Samaiyar, M. Elmansouri, D. Filipovic, and P. Valale Prasannakumar. Phased Array Antenna for Bi-Static Simultaneous Transmit and Receive (STAR) system. In 2020 IEEE International Symposium on Antennas and Propagation and North American Radio Science Meeting, pages 173–174, 2020.

[139] Timothy Sonnenberg, Anthony Romano, Shane Verploegh, Mauricio Pinto, and Zoya Popović. V- and W-Band Millimeter-Wave GaN MMICs. IEEE Journal of Microwaves, 3(1):453–465, 2023.

[140] Judson E. Stailey and Kurt D. Hondl. Multifunction Phased Array Radar for Aircraft and Weather Surveillance. Proceedings of the IEEE, 104(3):649–659, 2016.

[141] Kyle A. Steiner and Mark B. Yeary. A 1.6-GHz Sub-Nyquist-Sampled Wideband Beamformer on an RFSoC. IEEE Transactions on Radar Systems, 1:308–317, 2023.

[142] Salvador H. Talisa, Kenneth W. O'Haver, Thomas M. Comberiate, Matthew D. Sharp, and Oscar F. Somerlock. Benefits of Digital Phased Array Radars. Proceedings of the IEEE, 104(3):530–543, 2016.

[143] S. Tanaka, N. Shimomura, and K. Ohtake. Active circulators—The realization of circulators using transistors. Proceedings of the IEEE, 53(3):260–267, 1965.

[144] G.C. Tavik, C.L. Hilterbrick, J.B. Evins, J.J. Alter, J.G. Crnkovich, J.W. de Graaf, W. Habicht, G.P. Hrin, S.A. Lessin, D.C. Wu, and S.M. Hagewood. The advanced multifunction RF concept. IEEE Transactions on Microwave Theory and Techniques, 53(3):1009–1020, 2005.

[145] Ali Soltani Tehrani, Haiying Cao, Sepideh Afsardoost, Thomas Eriksson, Magnus Isaksson, and Christian Fager. A comparative analysis of the complexity/accuracy tradeoff in power amplifier behavioral models. IEEE Transactions on Microwave Theory and Techniques, 58(6):1510–1520, 2010.

[146] T. Tokumitsu, S. Hara, T. Takenaka, and M. Aikawa. Divider and combiner line-unified FET's as basic circuit function modules. II. IEEE Transactions on Microwave Theory and Techniques, 38(9):1218–1226, 1990.

[147] Xavier Vilajosana, Guillem Boquet, Joan Melià-Seguí, Pere Tuset-Peiró, Borja Martinez, and Ferran Adelantado. Challenges and Opportunities for Simultaneous Multifunctional Wireless Networks in the UHF Band. IEEE Communications Magazine, 61(5):48–54, 2023.

[148] Huaiyi Wang, Joel Johnson, Chris Baker, Lixin Ye, and Chenglin Zhang. On spectrum sharing between communications and air traffic control radar systems. In 2015 IEEE Radar Conference (RadarCon), pages 1545–1550, 2015.

[149] Xiaoxin Wang, Zhipeng Jiang, Wenguo Yang, and Suixiang Gao. The optimization of self-interference in wideband full-duplex phased array with joint transmit and receive beamforming. Journal of Combinatorial Optimization, 44, 2022.

[150] Xiyao Wang, Qi Cai, Haoshen Zhu, Wenjie Feng, Quan Xue, and Wenquan Che. A 28 GHz GaN HEMT quasi-circulator with high isolation and high power-handling capability. Microwave and Optical Technology Letters, 64(1):72–76, 2022.

[151] Zhongxiang Wei, Fan Liu, Christos Masouros, Nanchi Su, and Athina P. Petropulu. Toward Multi-Functional 6G Wireless Networks: Integrating Sensing, Communication, and Security. IEEE Communications Magazine, 60(4):65–71, 2022.

[152] James Wilson, Janet Liu, Benjamin Epstein, and Anna Tauke-Pedretti. Scalable On-Array Processing (SOAP). In 2024 IEEE International Symposium on Phased Array Systems and Technology (ARRAY), pages 1–3, 2024.

[153] Yue Ming Wu, Cheng-Yung Ke, Chien Cheng Wang, Ying Hsuan Tang, Yu-Wei Chen, Chien-Te Li, Li-Han Chang, Ching-Yun Chu, Borching Su, Ta-Shun Chu, and Yu-Jiu Wang. An X-band Scalable 4×4 Digital Phased Array Module using RF SoC and Antenna-in-Package. In 2019 IEEE Radar Conference (RadarConf), pages 1–6, 2019.

[154] Mingcong Xie, Xizhang Wei, Yanqun Tang, and Dujuan Hu. A Robust Design for Aperture-Level Simultaneous Transmit and Receive with Digital Phased Array. Sensors, 22(1), 2022.

[155] Nan Yang, Lifeng Wang, Giovanni Geraci, Maged Elkashlan, Jinhong Yuan, and Marco Di Renzo. Safeguarding 5G wireless communication networks using physical layer security. IEEE Communications Magazine, 53(4):20–27, 2015.

[156] J. Andrew Zhang, Fan Liu, Christos Masouros, Robert W. Heath, Zhiyong Feng, Le Zheng, and Athina Petropulu. An Overview of Signal Processing Techniques for Joint Communication and Radar Sensing. IEEE Journal of Selected Topics in Signal Processing, 15(6):1295–1315, 2021.

[157] Jie Zhang and Jiudong Zheng. Prototype Verification of Self-Interference Suppression for Constant-Amplitude Full-Duplex Phased Array with Finite Phase Shift. Electronics, 11(3), 2022.

[158] Qinzhen Zhang, Jie Zhang, Jiudong Zheng, and Hongchao Wu. Self-Interference Cancellation of Partitioning Simultaneous Transmit and Receive Phased Array. In 2020 IEEE 9th Joint International Information Technology and Artificial Intelligence Conference (ITAIC), volume 9, pages 1406–1409, 2020.

[159] Gan Zheng, Ioannis Krikidis, Jiangyuan Li, Athina P. Petropulu, and Björn Ottersten. Improving Physical Layer Secrecy Using Full-Duplex Jamming Receivers. IEEE Transactions on Signal Processing, 61(20):4962–4974, 2013.

[160] You Zheng and Carlos E. Saavedra. Active Quasi-Circulator MMIC Using OTAs. IEEE Microwave and Wireless Components Letters, 19(4):218–220, 2009.

Appendix A

Appendix

A.1 Introduction

This appendix presents the detailed simulation results for the mutual coupling reduction techniques discussed in Section 3.3 as well as the reduced mutual coupling array design highlighted in Section 3.4. Section A.2 contains the model diagrams and plots for the different iterations of the metallic posts, metallic walls, electromagnetic bandgap structures (EBGs), and defected ground structures (DGSs) inserted between the elements of the 7-element linear array. Section A.3 presents the array models, S11 magnitudes, mutual coupling results, and array gain for the different design configurations of the 25-element array that was focused on reducing the mutual coupling between elements in two dimensions (2D).

A.2 Coupling-Reduction Techniques Results

Beginning with the metallic posts, Fig. A.1a illustrates the strength of the E-field magnitudes on the 7-element array model with the side and top-down views shown, as well as the field/plane directions. Fig. A.1b plots the E-plane mutual coupling results for designs with posts that vary their radii between 10 and 50 mils as well as their heights between 250 and 750 mils, as indicated by the first and second numbers in the legend, respectively. These results are compared to the baseline in the plot, while the changes from the baseline are displayed in Fig. A.1c, where the largest/tallest posts are found to provide the most coupling decrease. Similar to the E-plane model, Fig. A.1d displays the strength of the H-field magnitude for the 7-element H-plane array model with side and

top views shown (note the change in the field/plane directions). Comparing Figs. A.1a and A.1d, the H-field strength is seen to decay more rapidly than the E-field. Figs. A.1e and A.1f plot the mutual coupling and coupling changes, respectively, and indicate that the largest reductions on the H-plane also occur for the largest/tallest posts.

Fig. A.2 depicts the models and results for the array with metallic walls inserted between the elements, where the walls vary in height from 250 to 1250 mils. The taller walls are seen to reduce the coupling in both the E- and H-planes. Fig. A.3 shows the models and coupling values for the EBG structures that are created using metallic posts with square top hats to produce high-impedance structures. The posts have fixed radii of 50 mils, but their heights vary between 250 and 750 mils and the top hat sizes change between 200 and 350 mils, which are limited by the element spacing. The larger top hats on the taller posts are seen to provide the most coupling reduction. Finally, Fig. A.4 displays the array models and simulation results for the arrays with DGSs between elements, which consist of slots cut into the bottom-side ground plane between the elements. The size of the slots is swept between 1500 by 200 mils and 2500 by 400 mils, where the size is not found to impact the coupling, except for the largest case. Overall, the results of each of these are summarized in Table 3.1 in Chapter 3.

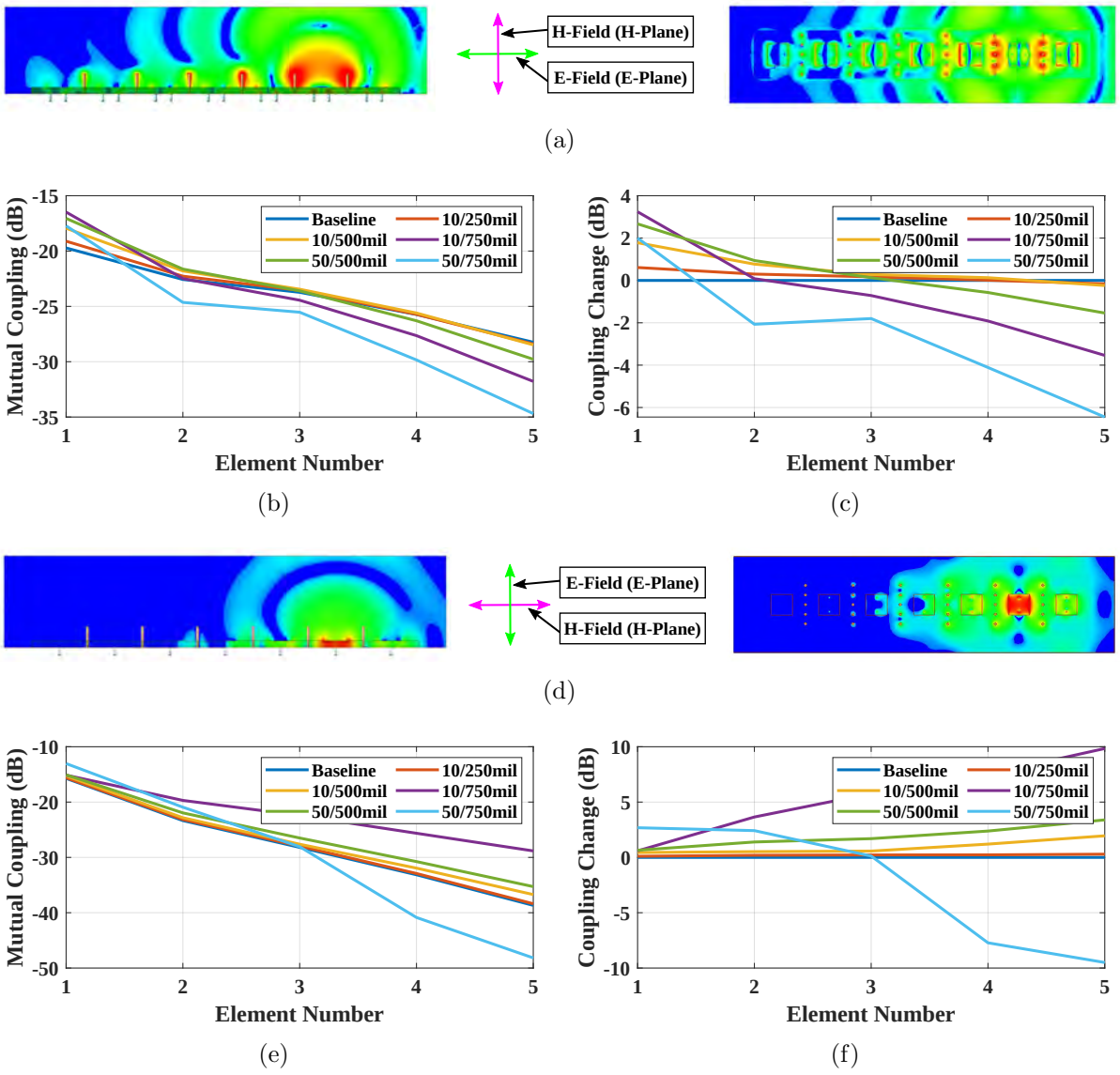


Figure A.1: Simulation results of mutual coupling changes for a 7-element array with metallic posts between elements, highlighting the (a) E-field magnitudes for the E-plane model; (b) mutual coupling and (c) coupling changes from the baseline for different post sizes on the E-plane array; (d) H-field magnitudes for the H-plane model; (e) mutual coupling and (f) coupling changes from the baseline for different post sizes on the H-plane array.

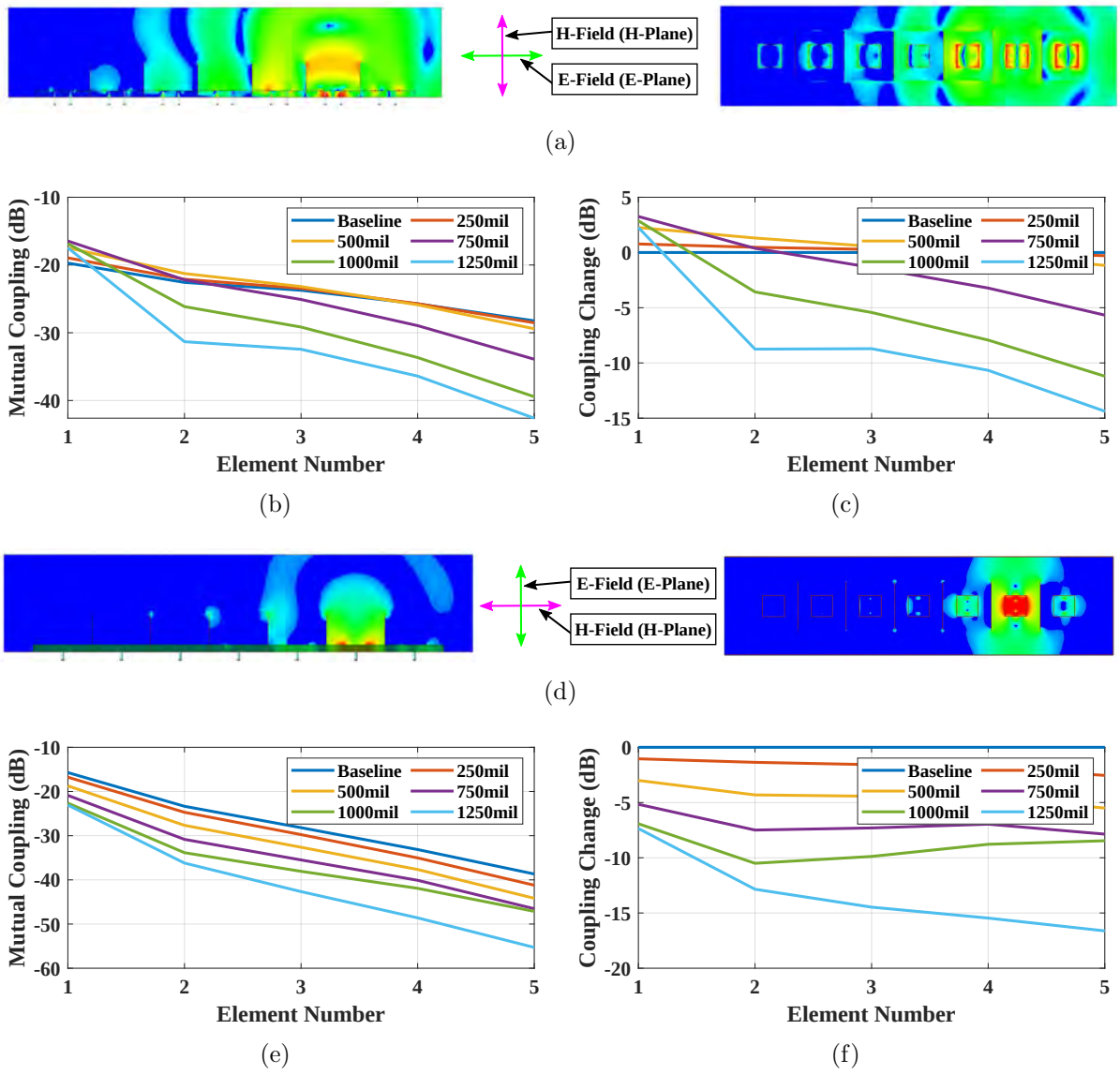


Figure A.2: Simulation results of mutual coupling changes for a 7-element array with metallic walls between elements, highlighting the (a) E-field magnitudes for the E-plane model; (b) mutual coupling and (c) coupling changes from the baseline for different wall sizes on the E-plane array; (d) H-field magnitudes for the H-plane model; (e) mutual coupling and (f) coupling changes from the baseline for different wall sizes on the H-plane array.

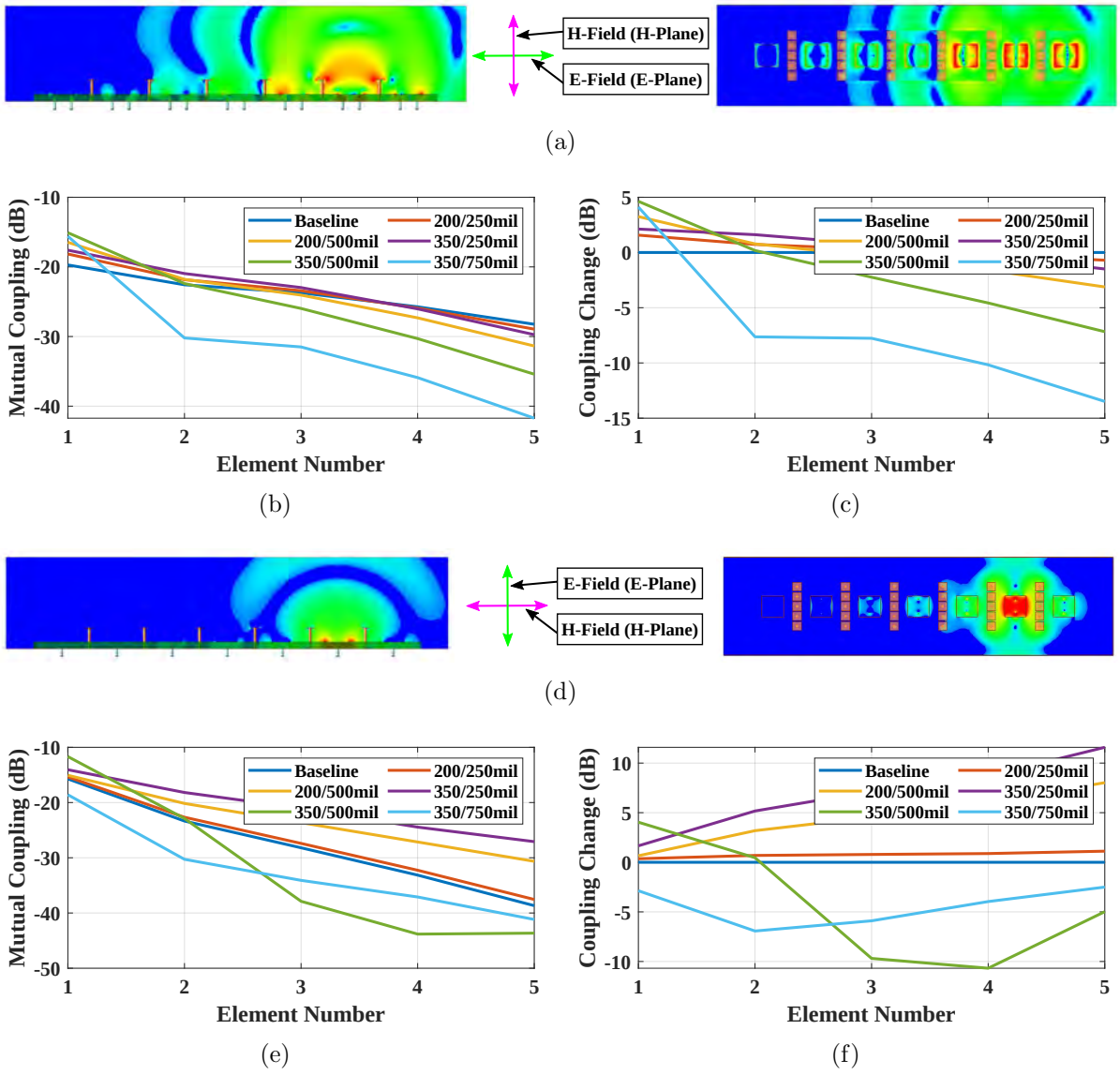


Figure A.3: Simulation results of mutual coupling changes for a 7-element array with EBG between elements, highlighting the (a) E-field magnitudes for the E-plane model; (b) mutual coupling and (c) coupling changes from the baseline for different EBG sizes on the E-plane array; (d) H-field magnitudes for the H-plane model; (e) mutual coupling and (f) coupling changes from the baseline for different EBG sizes on the H-plane array.

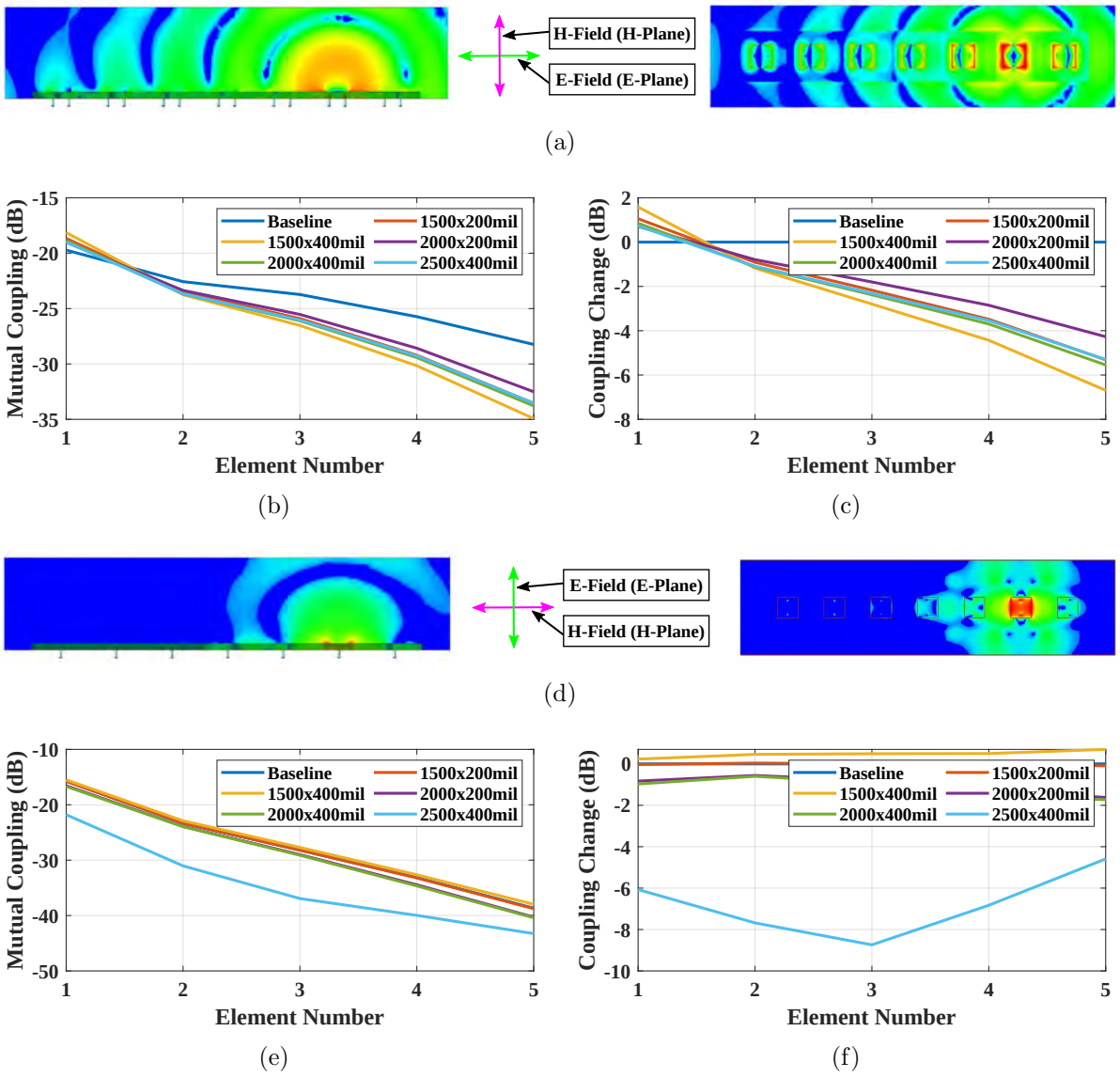


Figure A.4: Simulation results of mutual coupling changes for a 7-element array with DGS between elements, highlighting the (a) E-field magnitudes for the E-plane model; (b) mutual coupling and (c) coupling changes from the baseline for different DGS sizes on the E-plane array; (d) H-field magnitudes for the H-plane model; (e) mutual coupling and (f) coupling changes from the baseline for different DGS sizes on the H-plane array.

A.3 Reduced-Coupling Array Design Results

Based on the findings of the previous section, a 25-element 2D array with reduced mutual coupling was created and compared to a baseline, as discussed in Section 3.4. Several different design configurations were investigated between the baseline and the final reduced-coupling array, where this appendix contains summaries of their details. Fig. A.5a illustrates the model of a 3-GHz array design with 45-degree rotated patches and 1/2-λ-element spacing. Fig. A.5b depicts the S11 magnitude for the passive and three active (1D horizontal, 1D vertical and 2D) cases considered, and indicates a well-matched design just below 3 GHz for all. The mutual coupling to the center element for the locations referenced in Fig. 3.4 is plotted in Fig. A.5c, and shows an overall maximum value of -24.0 dB for the H1 element position. Finally, Fig. A.5d illustrates the array gain for azimuth and elevation angles with a uniform beamformer.

Fig. A.6 represents the results of a design with straight patches and a 3/4-λ-element spacing where the overall maximum mutual coupling is -24.1 dB from the V1 element location. Fig. A.7 displays an array with 45-degree rotated patches and a 3/4-λ-element spacing where the maximum overall coupling is -28.3 dB from the D1 element position. Fig. A.8 depicts a design with 45-degree rotated patches and a 3/4-λ-element spacing with 1-inch square walls where the overall maximum mutual coupling is -28.6 dB from the D1 element location. Fig. A.9 illustrates an array with 45-degree rotated patches, 3/4-λ-element spacing with 0-inch chamfered walls where the maximum overall coupling is -28.6 dB from the D1 element position. These as well as the baseline and final reduced-coupling array results are summarized in Table 3.2 within Chapter 3.

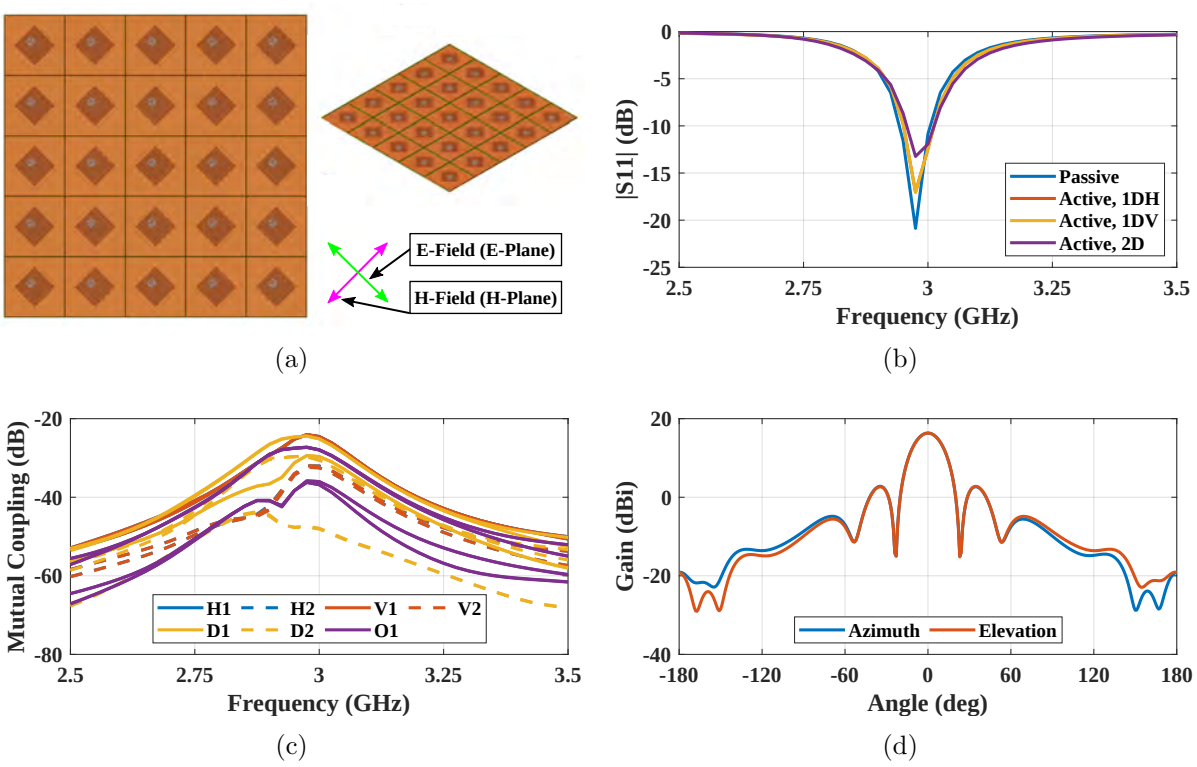


Figure A.5: Reduced-coupling 25-element patch array configuration 1: (a) top and isometric model views with field directions indicated; (b) simulated S11 magnitude for passive and active (1D horizontal, 1D vertical and 2D) configurations; (c) simulated mutual coupling to the center element for the locations referenced in Fig. 3.4; and (d) simulated azimuth and elevation gain patterns.

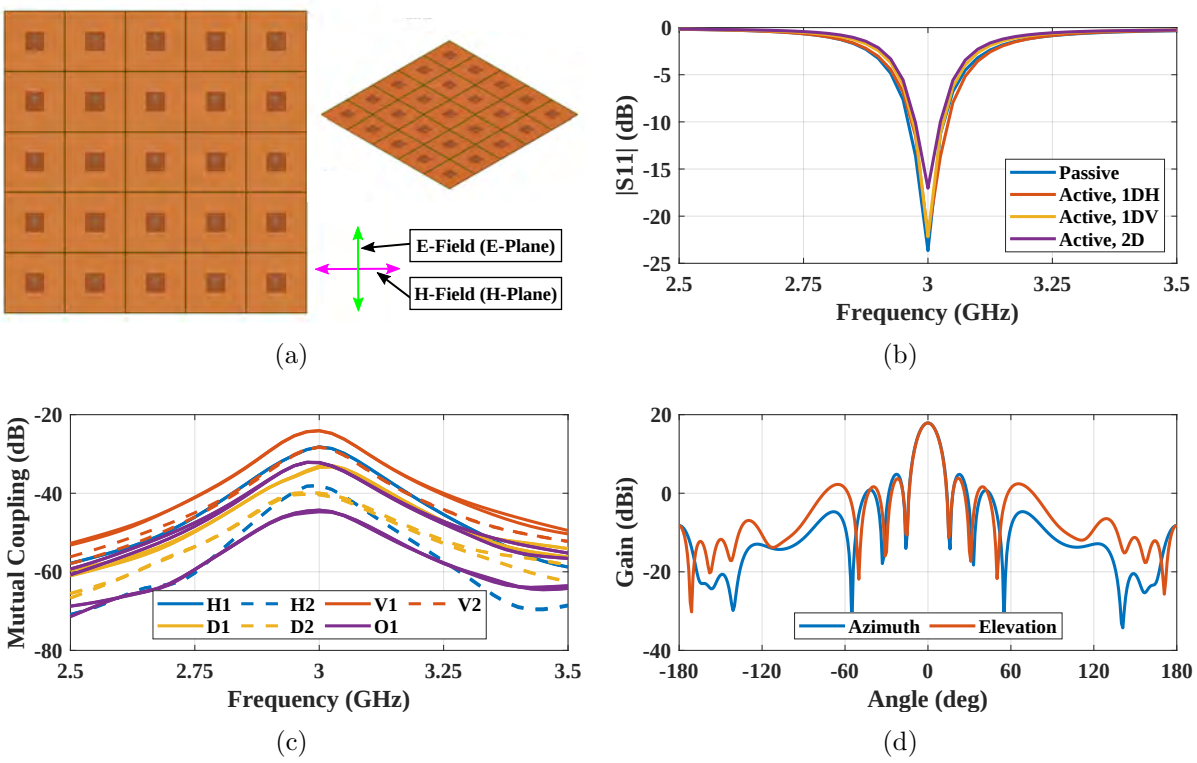


Figure A.6: Reduced-coupling 25-element patch array configuration 2: (a) top and isometric model views with field directions indicated; (b) simulated S11 magnitude for passive and active (1D horizontal, 1D vertical and 2D) configurations; (c) simulated mutual coupling to the center element for the locations referenced in Fig. 3.4; and (d) simulated azimuth and elevation gain patterns.

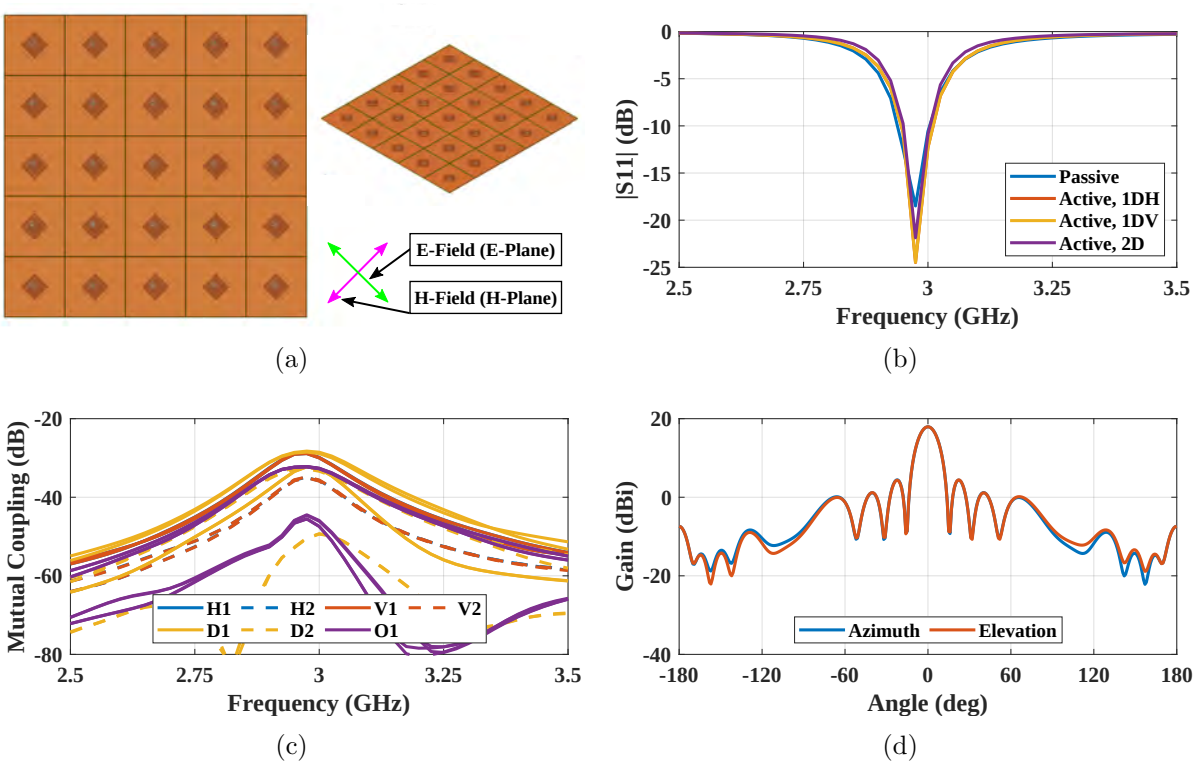


Figure A.7: Reduced-coupling 25-element patch array configuration 3: (a) top and isometric model views with field directions indicated; (b) simulated S11 magnitude for passive and active (1D horizontal, 1D vertical and 2D) configurations; (c) simulated mutual coupling to the center element for the locations referenced in Fig. 3.4; and (d) simulated azimuth and elevation gain patterns.

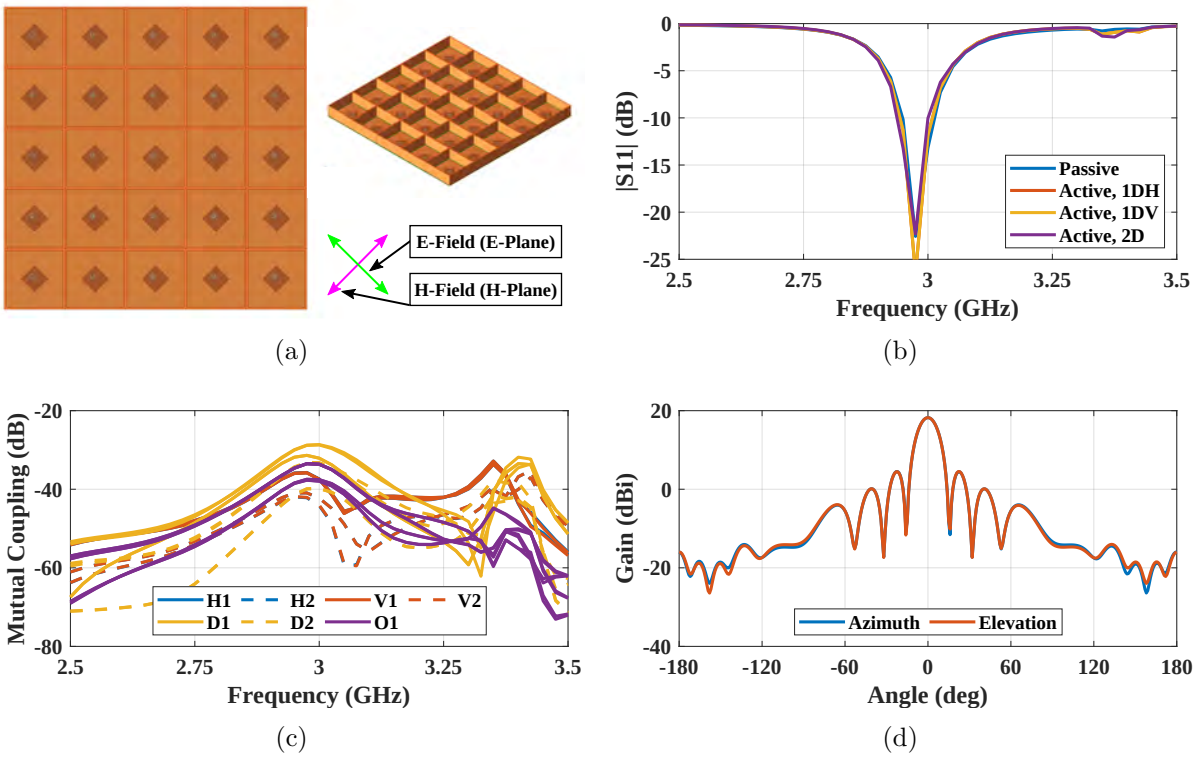


Figure A.8: Reduced-coupling 25-element patch array configuration 4: (a) top and isometric model views with field directions indicated; (b) simulated S11 magnitude for passive and active (1D horizontal, 1D vertical and 2D) configurations; (c) simulated mutual coupling to the center element for the locations referenced in Fig. 3.4; and (d) simulated azimuth and elevation gain patterns.

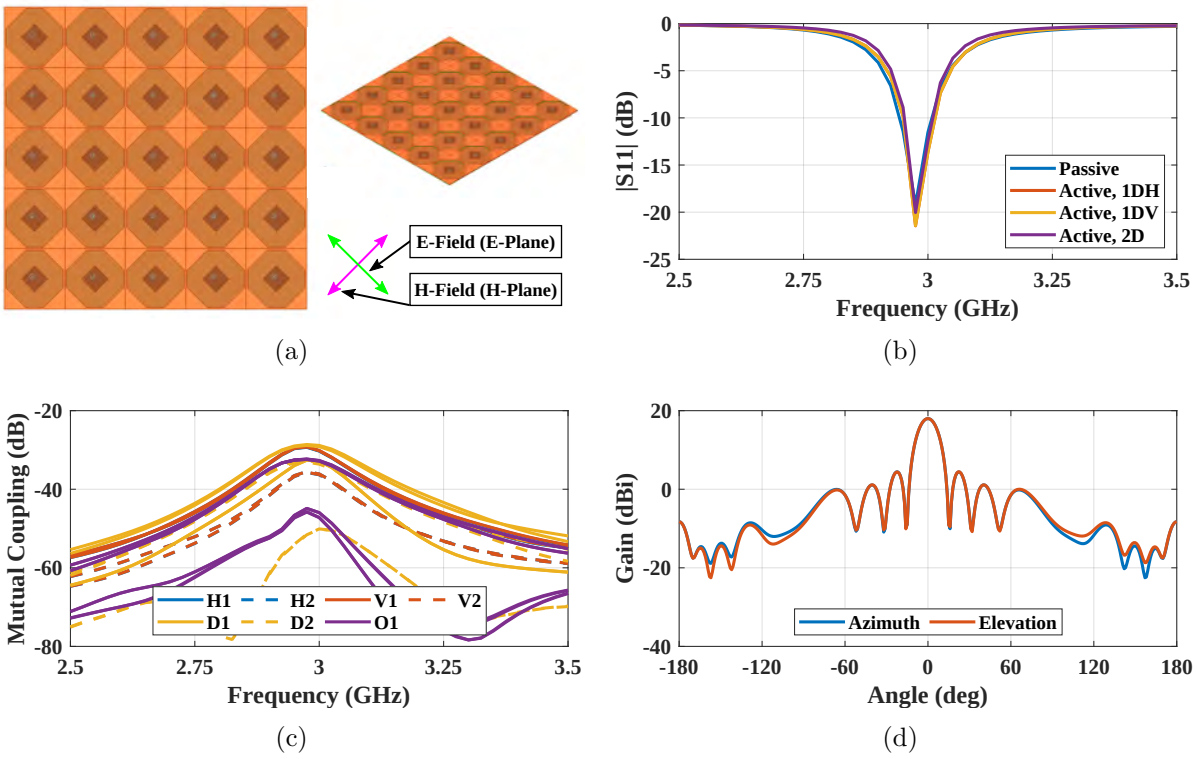


Figure A.9: Reduced-coupling 25-element patch array configuration 5: (a) top and isometric model views with field directions indicated; (b) simulated S11 magnitude for passive and active (1D horizontal, 1D vertical and 2D) configurations; (c) simulated mutual coupling to center element for the locations referenced in Fig. 3.4; and (d) simulated azimuth and elevation gain patterns.

ProQuest Number: 32445966

INFORMATION TO ALL USERS
The quality and completeness of this reproduction is dependent on the quality
and completeness of the copy made available to ProQuest.



Distributed by
ProQuest LLC a part of Clarivate (2026).
Copyright of the Dissertation is held by the Author unless otherwise noted.

This work is protected against unauthorized copying under Title 17,
United States Code and other applicable copyright laws.

This work may be used in accordance with the terms of the Creative Commons license
or other rights statement, as indicated in the copyright statement or in the metadata
associated with this work. Unless otherwise specified in the copyright statement
or the metadata, all rights are reserved by the copyright holder.

ProQuest LLC
789 East Eisenhower Parkway
Ann Arbor, MI 48108 USA